Master's thesis

NTNU
Norwegian University of Science and Technology
Faculty of Medicine and Health Sciences
Department of Clinical and Molecular Medicine

Mouzuna Munir

The Role of DNA Repair Enzyme NEIL3 in Hippocampal Development and Function

Master's thesis in Molecular Medicine
Supervisor: Jing Ye
Co-supervisor: Magnar Bjørås
January 2024

NTNU
Norwegian University of
Science and Technology

Mouzuna Munir

The Role of DNA Repair Enzyme NEIL3 in Hippocampal Development and Function

Master's thesis in Molecular Medicine
Supervisor: Jing Ye
Co-supervisor: Magnar Bjørås
January 2024

Norwegian University of Science and Technology
Faculty of Medicine and Health Sciences
Department of Clinical and Molecular Medicine

NTNU
Norwegian University of
Science and Technology

Abstract

Recent findings underscore emerging insights into the multifaceted roles of NEIL3 within the brain, particularly in hippocampus region. Studies with rodents have delineated a discernible expression profile of NEIL3 within the subgranular zone of the dentate gyrus and the subventricular zone of the lateral ventricles throughout developmental stages, indicative of its involvement in neuronal organization and hippocampal development. In addition, NEIL3-depleted mice display impaired spatial learning and memory in the Morris Water Maze (MWM), suggesting a unique role of NEIL3 in the regulation of hippocampal functions.

The first aim of this investigation is to discern the impact of NEIL3 on the gene expression within the hippocampal subregions. Transcriptomic study conducted on mice at three months of age revealed noteworthy differentially expressed genes, such as Drd2, Grm gene subunits, and Rgs gene subunits, known pivotal components within G-protein signalling pathways. Subsequent investigations were undertaken to discern alterations in the hippocampal transcriptome in the absence of NEIL3 followed by qPCR analyses, providing normalized gene expression data for comparison between Neil3-/- and Wild-type counterparts.

The second aim of this study is to investigate the influence of NEIL3 in the organization of GABAergic inhibitory neurons. This objective was achieved by Immunohistochemistry studies utilizing various cellular markers, including GAD67, PV, and Somatostatin. The samples were visualized using confocal imaging, subsequently processed through 3D software Imaris, and subjected to a comparative analysis to discern distinctions between the two groups.

The third aim of this study is to investigate the the role of NEIL3 in the postnatal maturation of hippocampal subregions. This objective was achieved by utilization of various markers, including ki67 for proliferating cells, Sox2 for neural progenitor cells, along with DCX for immature neurons, NeuroD1, and NeuN for mature neurons, to assess the maturation and organization of distinct neuronal populations during postnatal days 2 (p2) and 8 (p8) in both wild-type and Neil3-/- mice.

The outcomes of my study indicate the following findings: (1) the normalized gene expression identified in both the hippocampal CA1 and DG regions via qPCR revealed distinct expression patterns of these genes in WT and Neil3-/- (2) The absence of NEIL3 significantly influences the organization of GABAergic inhibitory neurons within the hippocampus, elucidating a marked reduction in the inhibitory network observed in knockout mice, highlighting the functional role of NEIL3 in the hippocampus. (3) A decrease in proliferating neurons and neural progenitor cells, reduced DCX expression, increase in mature neurons like NeuN and NeuroD1 were noted in the hippocampus of P8 mice compared to P2 mice were observed. Furthermore, the alterations in the numbers of these neurons in Neil3-/-, emphasize the role of NEIL3 in the postnatal maturation of hippocampus.

In summary, my results indicate that the DNA repair enzyme NEIL3 plays an important role in the hippocampal development and function.

Sammendrag

Nylige funn understreker nye innsikter i de mange rollene NEIL3 har i hjernen, spesielt i hippocampus-regionen. Studier med gnagere har avdekket et tydelig uttrykksmønster for NEIL3 i den subgranulære sonen av dentate gyrus og den subventrikulære sonen av laterale ventrikler gjennom utviklingsstadiene. Dette indikerer at NEIL3 er involvert i nevronal organisasjon og utvikling av hippocampus. I tillegg viser forsøk med NEIL3-depletet mus at de har nedsatt romlig læring og hukommelse i Morris Water Maze (MWM), noe som antyder at NEIL3 har en unik rolle i reguleringen av hippocampusfunksjoner.

Det første målet med denne studien er å undersøke NEIL3s innvirkning på genuttrykket innenfor de ulike delområdene av hippocampus. En transkriptomisk studie utført på mus ved tre måneders alder avdekket signifikante forskjeller i genuttrykk, blant annet for gener som Drd2, underenheter av Grm-genet og Rgs-genet, som er kjente komponenter i G-protein signalveier. Videre undersøkte vi endringer i hippocampus' transkriptom i fravær av NEIL3, etterfulgt av qPCR-analyser som ga normaliserte genuttrykksdata for sammenligning mellom mus med og uten NEIL3.

Det andre målet med studien er å undersøke NEIL3s innflytelse på organisasjonen av GABAerge hemmende nevroner. Dette målet ble oppnådd gjennom immunohistokjemiske studier ved bruk av ulike cellulære markører, inkludert GAD67, PV og Somatostatin. Prøvene ble visualisert ved hjelp av konfokal avbildning, behandlet med 3D-programvaren Imaris, og deretter analysert for å finne forskjeller mellom de to gruppene.

Det tredje målet med studien er å undersøke NEIL3s rolle i den postnatale modningen av hippocampus. Dette ble gjort ved hjelp av ulike markører, som ki67 for prolifererende celler, SOX2 for nevrale stamceller, DCX for umodne nevroner, samt NeuroD1 og NeuN for modne nevroner. Vi vurderte modningen og organiseringen av ulike nevronale populasjoner hos mus ved postnatale dager 2 (p2) og 8 (p8), både hos ville mus og mus uten NEIL3.

Resultatene fra studien indikerer følgende funn: (1) Det normaliserte genuttrykket, identifisert både i hippocampus CA1 og DG-regioner via qPCR, avslørte distinkte uttrykksmønstre av disse genene hos mus med og uten NEIL3. (2) Fraværet av NEIL3 påvirker betydelig organiseringen av GABAerge hemmende nevroner i hippocampus, og viser en markert reduksjon i det hemmende nettverket hos knockout mus, noe som understreker NEIL3s funksjon i hippocampus. (3) Vi observerte en nedgang i prolifererende nevroner og nevrale stamceller, redusert DCX-uttrykk, og økning i modne nevroner som NeuN og NeuroD1 i hippocampus hos mus ved p8 sammenlignet med p2. Endringene i antallet av disse nevronene hos mus uten NEIL3 understreker NEIL3s rolle i den postnatale modningen av hippocampus.

Oppsummert indikerer resultatene fra studien at DNA-reparasjonsenzymet NEIL3 spiller en viktig rolle i utviklingen og funksjonen til hippocampus.

Acknowledgements

First and foremost, I extend my heartfelt appreciation to my main supervisor, Jing Ye, for their unwavering support. I am grateful for their constant availability for questions and insightful discussions. I would also like to convey my thanks to my co-supervisor, Magnar Bjørås, for making this project possible and warmly welcoming me into the research group. My gratitude extends to all the members of the research group, with special mention to Marion Silvana Fernandez for invaluable assistance in animal training and teaching various research techniques, including staining and brain sectioning, while fostering a positive atmosphere. Thanks are due to Maria Camara for teaching me numerous methods and aiding in Imaris countings and confocal scanning. Additionally, I express my appreciation to my family and friends for their steadfast support and encouragement. Finally, I offer my thanks to Allah Almighty, without whose guidance completing this project would not have been possible.

Table of contents

List of figures and tables

.

Abbreviations

BER	Base excision repair
CA	Cornu Ammonis
DCX	Doublecortin
DEG	Differentially expressed genes
DG	Dentate gyrus
Drd2	Dopamine D2-like receptors
DISH	Double in situ hybridization
DNMT	DNA methyl transferase
EC	Entorhinal cortex
GABA	Gamma aminobutyric acid
GAD67	Glutamic acid decarboxylase
Grm	Metabotropic glutamate receptor 1
GCL	Granular cell layer
GCL	Granular cell layer
HF	Hippocampal formation
IHC	Immunohistochemistry
LEC	Lateral entorhinal cortex
MCL	Molecular cell layer
MEC	Medial entorhinal cortex
NEIL1	Nei endonuclease VIII-like protein 1
NeuN	Neuronal nuclear antigen
NeuroD1	Neurogenic differentiation 1
NOL	Novel object location
NSC	Neural stem cell
NSPC	Neural stem progenitor cell
PAR	parasubiculum
PCL	Pyramidal cell layer
PER	Perirhinal cortex
PHR	Parahippocamal region

POR	Postrhinal cortex
PrS	Presubuculum
PV	Parvalbumin
PFA	Paraformaldehyde
RGL	Radial Glial-like
RGS	Regulators of G-protein signaling protein
ROS	Reactive oxygen species
SGZ	Subgranular zone
SL	Stratum lucidum
SLM	Stratum lacunosum-moleculare
SO	Stratum oriens
Sox2	Sex determining region Y-box 2
SR	Stratum radiatum
ssDNA	Single stranded DNA
SVZ	Subventricular zone
TDG	Thymine DNA glycosylase
TET	Ten-eleven translocation methylcytosine dioxygenases
VZ	Ventricular zone

1: Introduction

1.1 A Comprehensive Overview of DNA damage in the brain

The prevalent proportion of spontaneous DNA alterations undergoes immediate repair by the body's DNA repair mechanisms. However, in cases where a gene responsible for DNA repair is dysfunctional or absent, it can lead to an elevated level of genomic instability and mutagenesis. [1]. These aberrations in the integrity of DNA have been robustly linked to diverse pathological states, encompassing cancer and neurodegenerative disorders. [2].

1.1.1 The Role of Oxidative Stress in DNA Damage

Oxidative damage to DNA is a common occurrence in the brain, mostly caused by endogenous reactive oxygen species (ROS) generated during cellular respiration [1, 3]. ROS have been recognized as essential second messengers in diverse cellular processes. However, at elevated concentrations, ROS can exert detrimental effects by causing oxidative damage to nucleic acids, particularly in genomic DNA [4]. These ROS can inflict a variety of damage to DNA, including oxidized bases, abasic sites, and strand breaks [5, 6]. As the brain has a high demand for energy due to continuous electrochemical signalling between neurons, ROS production in brain tissue is particularly elevated [7]. This underscores an increased requirement for DNA repair mechanisms to uphold genomic stability, with the base excision repair (BER) system being the fundamental means of repairing oxidative damage in the brain [7].

Neurons possess a heightened metabolic rate but exhibit low levels of antioxidant enzymes, rendering them vulnerable to oxidative stress caused by ROS [8]. Interestingly, ROS can also function as cellular messengers during long-term potentiation in the hippocampus, suggesting their involvement in cell signalling and homeostasis [9]. Neurodegenerative diseases commonly exhibit increased levels of DNA damage, including oxidative stress-induced DNA damage, that cause the cell death in conditions like stroke [10]. Dysfunction in base excision repair, has been implicated in neurodegeneration and ischemic brain disorders [11, 12]. Post-mitotic neurons exhibit a quiescent state due to their irreversible differentiation and absence of the DNA damage detection and repair machinery related to replication. Consequently, these neurons heavily depend on the base excision repair (BER) mechanism within the brain for maintenance and preservation of genomic integrity [3, 7]. Overall, these findings emphasize the significance of BER mechanism in brain's defence against oxidative DNA damage and the maintenance of genomic integrity in neurons.

1.1.2 Base Excision Repair (BER) in the brain

The base excision repair (BER) pathway plays a pivotal role in repairing of most of the intrinsic DNA lesions, including those prompted by alkylation, oxidation, depurination, deamination, and single strand breaks [13].

Intriguingly, knockouts of NEIL, a distinctive family of BER proteins, do not exhibit severe phenotypic consequences [14]. However, the continuous exposure of neurons to reactive

oxygen species (ROS) results in persistent damage, which can affect various nucleic acids and trigger cell death. The brain's neurons are primarily in a post-mitotic stage, with limited regions generating new neurons during adulthood, one such region is the subgranular zone (SGZ) of the dentate gyrus (DG) in the hippocampus where neurogenesis occurs [15]. Hence, an efficient repair mechanism specific to neurons is vital for maintaining optimal brain function, safeguarding the integrity of genetic material within neurons, and preventing oxidative damage [8].

Two mechanisms of BER can occur in cells which are recognised by the repair gap size and the enzymes involved. The initiation of the short-patch base excision repair (BER) process involves the recognition of the damaged base by a specialized DNA glycosylase enzyme. This enzyme cleaves the N-glycosidic bond of the damaged base, leading to the formation of an abasic site [16]. Presently, there are 11 recognized human DNA glycosylases, with NEIL3 being one of them [17]. After identifying and cleaving the damaged base, DNA glycosylase triggers a single-strand break, facilitated by AP endonuclease (APE1), which incises the abasic site on the 5'-side. Subsequently, a DNA polymerase fills the resulting gap by synthesizing the correct base, and a DNA ligase seals the ends of the DNA strand. This sequential process successfully reinstates the integrity of the previously damaged DNA strand [16, 18]. Long-patch BER involves the removal of 2-10 nucleotides and requires additional replication proteins for gap repair, including DNA polymerase δ/ε, PCNA, RFC, FEN1, and LIG1, are recruited to complete the repair process. Short-patch BER is independent of replication, while long-patch BER is mainly active in proliferating cells. [16, 19].

Beyond their pivotal function in nuclear DNA repair, enzymes involved in base excision repair (BER) also wield a substantial influence in preserving the integrity of the mitochondrial genome [20]. The expression and activity regulation of BER proteins exhibit tissue-specific and cell cycle-specific patterns. This implies that the expression levels of these proteins and their activity vary across different tissues [21].

Aberrations in the repair machinery are linked to an increased mutation burden, which may ultimately contribute to neuronal dysfunction and degeneration [22]. Dysfunction in some of the BER proteins seems to be involved in three of the most common neurodegenerative conditions: Alzheimer’s disease (AD), Parkinson’s disease (PD) and stroke [7].

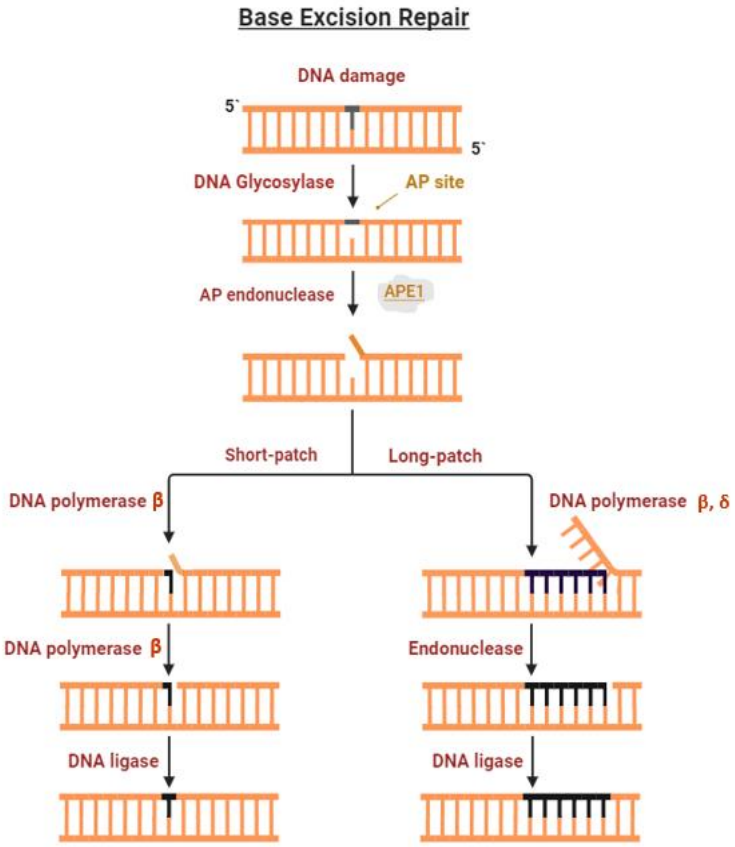

Figure 1: *The processes of Base Excision Repair (BER) are elucidated, differentiating between short-patch and long-patch BER. In short-patch BER, a damaged base is identified by a DNA glycosylase, leading to the cleavage of the N-glycosidic bond and the creation of an abasic site. Subsequently, AP endonuclease initiates the generation of a single-strand break, and the resulting gap is filled by DNA polymerase β, with DNA ligase then connecting the ends. Long-patch base excision repair (BER) follows a similar sequence but entails the removal of 2-10 nucleotides, employing replication proteins for both gap-filling and ligation. The diagram is constructed using BioRender.*

1.1.3 BER in DNA demethylation

The base excision repair (BER) pathway not only engages in DNA repair but also assumes a pivotal role in facilitating active DNA demethylation processes. [23]. DNA methylation and demethylation are epigenetic processes that regulate gene expression without altering the underlying DNA sequence [24]. In embryonic development, genome-wide demethylation is selective and occurs at specific loci, while gene-specific demethylation is triggered in cells responding to specific signals. Moreover, active DNA demethylation plays a critical role in facilitating the expression of genes related to neurogenesis and has been observed in post-mitotic neurons [25].

Recent research indicates that DNA demethylation can occur through two distinct mechanisms: passive demethylation and active demethylation, with the former being replication-dependent and the latter being enzymatic and BER-facilitated. Active DNA

demethylation is particularly important for gene expression regulation during specific developmental processes and in response to environmental cues. Although TDG-coupled BER is a well-known pathway for active DNA demethylation, other pathways have been proposed, suggesting that the accomplishment of this process can be facilitated through various mechanisms [25].

1.2 Nei Like DNA glycosylase 3 (NEIL3)

The human NEIL3 gene is situated on Chromosome 4q34.3, covering an approximate span of 53.25 kilobases and comprising 10 exons of diverse sizes. It encodes the NEIL3 protein, which is composed of 605 amino acids and has a anticipated molecular weight of 68 kDa [26]. In mice, the NEIL3 gene is encoded by the minus strand and is sited on Chromosome 8 B1.3. It is positioned adjacent to Aga and Vegfc genes. The gene encodes a protein consisting of 606 amino acids [26].

NEIL3 exhibits distinct expression pattern that is dependent on the cell cycle and primarily observed in neurogenic niches during early postnatal stages [27]. Alongside NEIL1 and NEIL2, NEIL3 possesses the ability to repair DNA in quadruplex structures, which is especially relevant for telomere DNA repair due to the frequent occurrence of quadruplex DNA formation at these sites [28]. NEIL3 also demonstrates high affinity for spiroiminodihydantoin (Sp) and guanidinohydantoin (Gh), and its base excision activity surpasses its AP-lyase activity, indicating its role as a monofunctional DNA-glycosylase that likely relies on APE1 as an endonuclease [29, 30].

NEIL3 is unique among the NEIL glycosylases due to its structural composition. Unlike NEIL1 and NEIL2, NEIL3 has a valine residue at the N-terminus, whereas other two have a catalytic proline at this position. Moreover, NEIL3 exhibits an extensive C-terminal extension, incorporating an additional C-domain with distinctive structural attributes. This extension comprises a potential nuclear localization signal (NLS), a zinc finger motif resembling RAN-binding protein, and two consecutive GRF zinc finger motifs [31, 32]. Despite these structural differences, NEIL3 also displays glycosylase activity and participates in base excision repair pathway [29, 32, 33]. Additionally, recent studies suggest that NEIL3 plays a functional role in epigenetic gene regulation. [34, 35].

1.2.1 Regional and Developmental Expression of NEIL3 in the Mouse Brain

Within the mouse brain, the expression of NEIL3 is localized in regions that comprise progenitor cells [29]. Research conducted in mice indicates that NEIL3 expression coincides with the process of organogenesis, occurring within the developmental timeframe of embryonic days 7 to 11.5 [36].

Neurogenesis in mice commences at embryonic day 12 (E12) and concludes by E17 [36]. During brain development, neurogenesis involves two proliferative populations known as the ventricular zone (VZ) and the subventricular zone (SVZ) [36]. The SVZ retains its capacity for promoting neurogenesis throughout adulthood [24]. Furthermore, a germinal zone known as the subgranular zone (SGZ) becomes apparent in the dentate gyrus (DG) after birth. [36]. NEIL3 expression has been observed in the VZ and SVZ during brain development in mice, but its levels decline as embryonic brain development progresses, leaving limited cells near the lateral ventricles and the DG at postnatal day 0 (P0) [36].

In the course of postnatal development, particularly commencing from postnatal day 3 (P3), the expression of NEIL3 has been detected in the subventricular zone (SVZ), the rostral migratory stream (RMS), the dentate gyrus of the hippocampus, and the Purkinje cells of the cerebellum [8]. However, as postnatal development advances, NEIL3 expression significantly diminishes, with fewer cells detected in the SVZ and layer V of the neocortex in one-month-old mice. In the brains of one-year-old mice, NEIL3 has been solely observed in layer V of the neocortex [8].

However, although NEIL3 expression decreases with age, it continues to be expressed in the hippocampal region [35], indicating that NEIL3 may exert a significant role in hippocampal functions, including spatial memory and learning.

1.2.2 Roles of NEIL3 in the Brain: A Comprehensive Analysis

NEIL3 has emerged as a pivotal contributor to the DNA repair mechanism. In addition to its central role in DNA repair, particularly in the Base Excision Repair (BER) process, NEIL3 is implicated in active DNA demethylation. In this context, NEIL3 serves as one of the glycosylases initiating the BER mechanism. It is suggested that NEIL3 may activate silenced genes through an alternative BER pathway involving active DNA demethylation [35, 37].

Recent studies have demonstrated that NEIL glycosylases, including NEIL1 and NEIL3, may have a potential binding affinity for oxidized cytosine derivatives and may accompany thymine DNA glycosylase (TDG) in reactivating epigenetically silenced genes [38]. However, their precise function in TET-dependent active DNA demethylation is yet to be determined. Nevertheless, research indicates that NEIL3 can compensate for the absence of TDG and instigate Base Excision Repair (BER) subsequent to TET oxidation. Hence, NEIL glycosylases could serve as an alternate route for active DNA demethylation, thereby playing a role in their participation in epigenetic gene regulation [38].

The functional scope of the NEIL3 protein extends beyond DNA oxidative repair. This glycosylase has been demonstrated to assume additional roles, including the maintenance of stem cell differentiation potential. Its essential role in the expression of multipotency factors, as well as in regulating neuronal and glial genes, underscores its broader involvement in cellular functions [39].

Research studies have demonstrated that NEIL3 plays a pivotal role in preserving genomic stability within neural cells by recognizing and eliminating oxidized DNA base lesions [40]. This repair activity is particularly important in neurons, as these cells are post-mitotic and cannot dilute the DNA damage through cell division. NEIL3 deficiency cause increased accumulation of oxidative DNA damage in neuronal genomes [40].

Fascinatingly, NEIL3 has also been associated with cognitive function and synaptic plasticity. Studies involving Neil3 knock-out mice have revealed decreased spatial performance in behavioral assessments, such as the Morris Water Maze (MWM) [41]. NEIL3 has been demonstrated to play a role in adult neurogenesis [41], suggesting its significance in maintaining functions reliant on the hippocampus for learning and memory [42]. These behavioral impairments were accompanied by altered synaptic protein expression and synaptic dysfunction in the hippocampus, a brain region essential for learning and memory processes.

Mice with a knock-out of Neil3 exhibit deficits in learning and memory, reduced anxiety-like behavior, changes in the expression of glutamatergic and gamma-aminobutyric acid receptors, heightened receptor density, and diminished post-synaptic density in the hippocampus [33].

1.3 Anatomy of the Hippocampal Region: A Key Player in Learning and Memory

The hippocampal region, located in the medial temporal lobe, holds a crucial function in spatial learning and the establishment of episodic memories. [43-45]. In terms of anatomy, the hippocampal area can be divided into two cortical sub-regions: the hippocampal formation (HF) and the parahippocampal region (PHR). The HF consists of the dentate gyrus (DG), the main hippocampus, and the subiculum (SUB). The main hippocampus, in turn, is subdivided into CA1, CA2, and CA3 regions. In common communication, the term "hippocampus" is typically employed to encompass both the DG and the hippocampus proper. Meanwhile, the parahippocampal region is located next to the HF on the border with the subiculum. It consists of five sub regions: the presubiculum (PRE), the parasubiculum (PAR), the entorhinal cortex (EC), and the postrhinal cortex (POR) [46]. The hippocampal formation (HF) and the parahippocampal region (PHR) collectively constitute a functional system or neuronal network referred to as the parahippocampal-hippocampal circuitry [46]. This circuitry serves as a network that establishes connectivity pathways among all the hippocampal fields, facilitating the flow of information [46]. Neocortical input reaches the hippocampal formation by passing through the superficial layers of the entorhinal cortex (EC). The perforant path is established by axons projecting unidirectionally from the superficial layers of the entorhinal cortex to the dentate gyrus (DG) [47]. Granule cells, serving as the primary neurons in the dentate gyrus (DG), project elongated axons referred to as mossy fibers. These axons establish connectivity with the pyramidal cells situated within the CA3 region of the hippocampus [47].

Furthermore, within the hippocampal formation, there are three distinct fields: CA3, CA2, and CA1, each with unique characteristics [20]. The dendrites of CA1 neurons either branch in the stratum lacunosum-moleculare after passing through the stratum radiatum or solely branch in the stratum radiatum [20]. CA1 pyramidal neurons possess two to eight dendrites covered with numerous dendritic spines and project a single axon through the stratum oriens in the alveus [20]. CA3 pyramidal neurons, larger in size than CA1 neurons, possess a diverse morphology of dendritic spines, with their apical dendritic tree branching near to the soma [20]. These neurons have a single axon that primarily projects to CA1 but also exhibits extensive collateralization within the CA3 region [20]. The CA1 field, in turn, projects excitatory output both to the SUB and the EC, completing the hippocampal processing loop [47]. The subiculum (SUB) serves as a significant source of subcortical projections, while the entorhinal cortex (EC) acts as the primary source of projections directed towards the neocortex [47]. Additionally, the granule cell layer between the CA3 and CA1 fields is known as the crest, and the CA2 field is distinguishable from other hippocampal fields using neurochemical markers, while the CA4 region represents the polymorphic layer of DG [48].

The hippocampal formation encompasses not only the CA fields but also the DG, SUB, PRE, PAR, and EC, forming an intricate circuitry involved in memory formation and spatial

navigation [49, 50]. The granule cells in the DG play a crucial role, with their dendrites reaching into the molecular layer and receiving inputs from various sources. The mossy cells, situated in the hilus, receive excitatory input from both granule cell mossy fibers and a subset of CA3 pyramidal neurons, while concurrently exhibiting inhibitory characteristics [20].

1.4 The Hippocampal functions:

The HF and the PHR play vital roles in memory formation, spatial navigation, and temporal dynamics [51]. Together, these areas form the hippocampal-parahippocampal network, where sensory inputs from the neocortex undergo comprehensive processing [44, 52-54]. Differing from various neocortical regions, the hippocampal area is distinguished by predominantly one-way connections. Within the parahippocampal region (PHR), it receives diverse sensory signals from the neocortex and forms two parallel pathways. One of these pathways includes the perirhinal cortex (PER), which transmits non-spatial information to the lateral entorhinal cortex (LEC) [20, 55], while the POR conveys spatial information to the medial entorhinal cortex (MEC) [56, 57]. The entorhinal cortex (EC) serves as the main source of cortical input to the hippocampal formation [46, 58]. Within the parahippocampal-hippocampal circuitry, Layer III of the lateral entorhinal cortex (LEC) directly communicates non-spatial information to the subiculum (SUB), while the medial entorhinal cortex (MEC) in the same layer conveys spatial information to CA1. Additionally, the specific function of Layer II in both LEC and MEC is to transmit information to the dentate gyrus (DG) [46, 59]. The DG receives multisensory inputs from the EC (Layer II) through the perforant pathway (PP) [53]. Sensory inputs from the DG are projected to CA3 via mossy fibers (MF), synapsing onto pyramidal cell dendrites [53]. The sensory inputs are relayed by pyramidal cells to CA1 through Schaffer collateral synapses. CA1 can subsequently project the processed memory output to the subiculum (Sub), and both CA1 and the Sub engage in communication with other brain structures. The deep layers of the entorhinal cortex (EC), specifically Layers V and VI, receive the processed memory output from CA1 [46, 54]. Interneurons within the circuit play a crucial role in regulating and controlling interactions among excitatory principal cells [60].

Memory formation and navigation involve the HF and the EC. The EC holds a universal memory representation, while HF processes detailed information through pattern separation and completion [46]. Increased activity in the EC is observed during memory recall, indicating its role in retrieving specific memory details, as well as providing a universal map for navigation within the HF [46].

The hippocampus plays a crucial role in encoding and storing episodic memory through its auto-associative network, primarily located in CA3, characterized by recurrent connections and stable states [61]. Place cells, which contribute to spatial memory, are found in CA1 [62], CA3 [63], SUB [64], PRE [65], and PAR [66]. The size of place fields in the hippocampus reflects spatial scale, allowing for different spatial resolutions in the brain [67]. Grid cells, located in the EC [68], also contribute to spatial memory and receive visuospatial information from the postrhinal cortex [69]. The EC serves as a secondary storage for spatial information and disruption of the connection between the medial EC and CA1 affects long-term spatial memory [70]. Head direction cells are primarily located in PRE [71], but directionally tuned cells can also be found in the EC [57]. The morphologically and molecularly distinct cell types within the medial entorhinal cortex (MEC) contribute to the mapping of grid cells, head-direction cells, and border cells [72].

In summary, the HF and the EC are integral components of the hippocampal-parahippocampal network, supporting memory formation and spatial navigation. While the EC provides a universal memory representation, the HF.

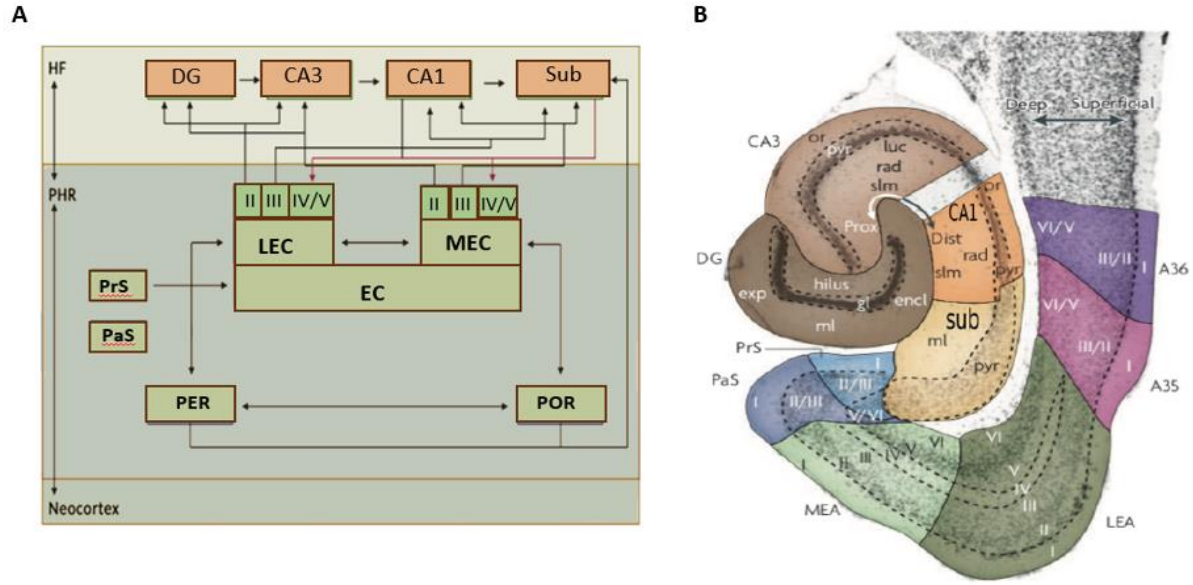

Figure 2: A) *Depicting the structure of the hippocampal-parahippocampal network, the diagram reveals parallel projection pathways originating from the perirhinal cortex (PER) to the lateral entorhinal cortex (LEC) and from the postrhinal cortex (POR) to the medial entorhinal cortex (MEC). Input from the entorhinal cortex (EC) is then transmitted to the hippocampal region, where layer II projects to the dentate gyrus (DG) and CA3, while layer III projects to CA1 and the subiculum (Sub). In the polysynaptic pathway, EC projects to DG, which subsequently projects to CA3, resulting in output from both CA1 and Sub to the deep layers of the MEC and LEC in the parahippocampal region. This depiction is a modified version. [46].* ***B)*** *The illustration displays the hippocampal-parahippocampal region in rats. Within the hippocampal formation, the depicted regions encompass the dentate gyrus (in dark brown), CA3 (in medium brown), CA2 (not shown), CA1 (in orange), and the subiculum (in yellow). In the parahippocampal region, the components include the Lateral Entorhinal Area (LEA) in dark green and the Medial Entorhinal Area (MEA) in light green. The perirhinal cortex is represented by Brodmann areas A35 (in pink) and A36 (in purple) [46].*

1.5 Hippocampus proper:

In common terminology, the term "hippocampus proper" typically encompasses the four CA fields (CA1, CA2, CA3, and CA4), while the broader term "hippocampal formation" includes not only the hippocampus proper but also the dentate gyrus and the subiculum [20]. The dentate gyrus consists of densely packed granule cells, forming a pointed wedge or semicircle. Proceeding inward, there are Cornu Ammonis (CA) areas, specifically CA4, CA3, CA2, and CA1, each housing densely packed pyramidal cells that bear resemblance to the organization found in the neocortex [48]. Adjacent to CA1 is the subiculum, which acts as a transitional zone connecting the hippocampus proper with the dentate gyrus. Beyond the subiculum are presubiculum and parasubiculum, followed by the transition to the entorhinal area in the cortex [47].

The hippocampus proper exhibits three distinct regions, namely CA1, CA2, and CA3, organized in a layered structure. The deepest layer, known as the stratum oriens or infrapyramidal region, primarily consists of dendrites from pyramidal cells and various interneurons [46]. Located above the stratum oriens is the pyramidal cell layer (PCL), predominantly composed of pyramidal neurons and interneurons. The outermost layer is the molecular layer, which is further divided into sublayers referred to as the stratum radiatum (SR) and the stratum lacunosum-moleculare (SLM). The suprapyramidal region (SR) within the molecular layer is the location of the Schaffer collaterals, which connect CA3 and CA1 [20]. Furthermore, CA3 features a narrow acellular region known as the stratum lucidum (SL), positioned directly above the pyramidal cell layer (PCL). This layer houses mossy fibers (MFs), which play a crucial role in connecting the dentate gyrus (DG) with the CA3 region [46, 73].

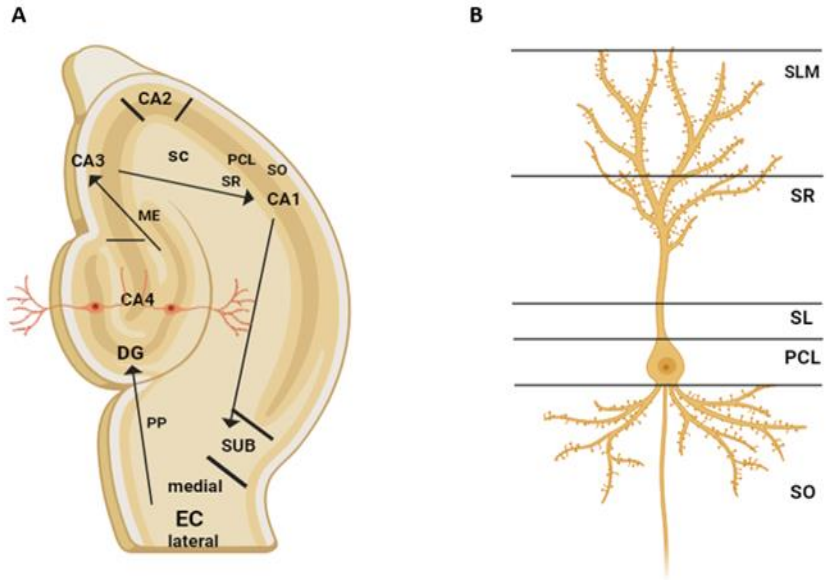

Figure 3: A) *Hippocampal and neural anatomy. A: Representation of hippocampal fiber systems, including the Cornu Ammonis areas (CA1, CA2, CA3, and CA4) in the hippocampus proper, and the hippocampal formation components (dentate gyrus or DG, subiculum or SUB, and entorhinal cortex or EC). The connection between the entorhinal cortex and the dentate gyrus occurs through the perforant path (PP). The dentate gyrus connects to CA3 through mossy fibers (MF), and CA3 connects to CA1 via Schaffer collaterals (SC). Additionally, CA1 independently connects to the subiculum and entorhinal cortex, with all these connections exhibiting unidirectional pathways. The figure was generated using Biorender.* ***B)*** *Schematic representation of a CA1 neuron and its dendrites, positioned in different layers of the CA1. With the pyramidal layer as the central point, the stratum radiatum lies immediately above, and the stratum oriens lies directly below, including pcl (pyramidal cell layer), sl-m (stratum lacunosum-moleculare), so (stratum oriens), and sr (stratum radiatum). The figure was generated using Biorender.*

1.5.1 Dentate gyrus

The dentate gyrus (DG) is a component of the hippocampal formation, receiving cortical input from the entorhinal cortex and projecting to CA3 pyramidal cells. Adult neurogenesis takes place in the DG, particularly in the subgranular zone (SGZ), where hippocampal neural stem cells undergo differentiation into granule cell progenitors expressing the marker Prox1. Prox1 is specific to glutamatergic granule cells, and these cells ultimately populate the SGZ of the DG [74].

The dentate gyrus (DG) exhibits anatomical and neurophysiological characteristics that support its hypothesized neural functions. With a neuron count approximately twice that of the entorhinal cortex [75]. The dentate gyrus (DG) has the capacity to generate a sparse and uncorrelated depiction of cortical information it receives. The minimal firing rate of granule cells in the DG, supported by tonic inhibition, contributes to enhancing the temporal sparsity within this representation.[75].

The dentate gyrus (DG) demonstrates a complex organization comprising three distinct layers: the molecular cell layer (MCL), granular cell layer (GCL), and polymorphic layer (hilus) [47]. The molecular cell layer (MCL), positioned closer to the hippocampal fissure, is relatively sparse and is predominantly composed of dendrites of granule cells, interneurons, polymorphic cells, as well as some interneurons and axons originating from the entorhinal cortex and other sources [47]. Deeper within DG, the GCL is densely packed with granule cells, forming a characteristic V-shape with a suprapyramidal (SPB) and infrapyramidal blade (IPB) configuration [76]. Granule cells, the predominant cell type in the dentate gyrus (DG), project their dendrites from the granule cell layer to the hippocampal fissure within the molecular cell layer (MCL) [47]. Furthermore, mossy fibers that originate from dentate gyrus (DG) granule cells form multiple synapses on CA3 pyramidal cells. This arrangement facilitates the dependable activation of pyramidal neurons with minimal action potentials from DG granule cells. This connectivity enables the robust transmission of a sparse neural code across different brain regions [77].

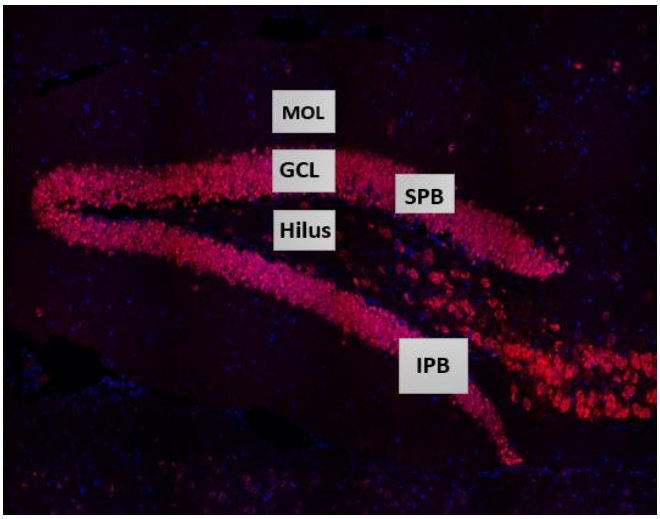

Figure 4: *Illustration of the dentate gyrus, comprising three layers: the molecular layer (MOL), granule cell layer (GCL), and the hilus (H), also known as the polymorphic layer. The hilus is further divided into two blades: the suprapyramidal blade (SPB), situated between CA3 and CA1, and the infrapyramidal blade (IPB), positioned beneath CA3.*

1.5.2 The Dentate Gyrus: Key Player in Learning and Memory Formation within the Hippocampus

The formation of long-term memory is a complex machanism involving the encoding of sensory input into a durable memory trace, storage, consolidation, and recall [78]. The dentate gyrus (DG) functions as a significant input region to the hippocampus and is implicated in hippocampal-dependent memory processes, encompassing episodic and spatial memory [79]. Experimental studies have demonstrated that DG lesions result in impaired performance in memory tasks reliant on hippocampal function [78, 80, 81].

Within the dentate gyrus (DG) of the hippocampus, the sub-granular zone (SGZ) serves as a specialized environment for neural stem cells (NSCs) in the adult mammalian brain. Positioned between the granule cell layer and the hilus, the SGZ provides a microenvironment conducive to the proliferation of NSCs and the progression of specification and differentiation of dentate granule neurons. Adult-generated dentate granule neurons undergo distinct developmental stages, beginning with type 1 radial glia-like cells (RGLs), representing the NSC population. Type 1 RGLs give rise to proliferating intermediate progenitor cells (IPCs), also known as type 2 cells, exhibiting transient amplifying characteristics. Subsequently, type 2 cells generate neuroblasts (type 3), which undergo differentiation into mature dentate granule neurons. Furthermore, the sub-granular zone (SGZ) accommodates various other cell types that facilitate neurogenesis, and it features a dense vascular network closely associated with neural stem cells (NSCs) [79].

In a clinical context, spatial memory, in particular, declines during age-related neurodegenerative diseases and normal aging [82]. The hippocampal-parahippocampal network, with the DG as a core component, undergoes functional changes in different cognitive deficits. These changes include reduced input to the DG through the perforant pathway (PP), decreased levels of adult neurogenesis[83, 84], impaired pattern separation abilities [85], and disrupted synaptic plasticity [86]. Gaining a precise understanding of the dentate gyrus (DG) and the underlying mechanisms related to spatial memory and learning is of considerable importance from both clinical and neurobiological standpoints.

1.5.3 Cornu Ammonis 1 (CA1)

The Ammon's horn, a component of the hippocampus, exhibits segregation into distinct subdivisions named CA1, CA2, and CA3, arranged along the transverse axis. Furthermore, it undergoes horizontal partitioning into a series of well-structured layers, including the stratum oriens, stratum pyramidale (also known as SP or the pyramidal cell layer), stratum radiatum (SR), and stratum lacunosum-moleculare [87]. The pyramidal layer, now called the pyramidal cell stratum, is main type of cells found densely packed in the CA1 region. These cells form the majority of neurons and exhibit a striking similarity in the structure of their dendritic trees, showing a consistent pattern among them [20].

CA1 pyramidal neurons can be categorized into two primary groups based on their dendritic morphology. The first group includes neurons with a primary apical dendrite that extends through the stratum radiatum before bifurcating in the stratum lacunosum-moleculare. The second group comprises neurons with apical dendrites that bifurcate within the stratum radiatum [88]. CA1 pyramidal neurons have two to eight dendrites that stem from the base of the soma. These dendrites are covered with around 30,000 dendritic spines [47]. According to Andersen et al, CA1 neurons do not connect between

themselves except in the developing hippocampus. The neurons connect to the pyramidal neurons in the subiculum which is the most significant intrahippocampal connection of the CA1 [47]. The EC and CA3 pyramidal neurons are the main providers of excitatory input to the CA1 [47].

In the hippocampus, there are unique layers with different cell compositions. The stratum oriens, below the pyramidal layer, has lower cell density and contains basal dendrites and interneurons. Above the pyramidal layer in CA1 is the stratum radiatum, which accommodates specific interconnections such as CA3 to CA3 associational connections and CA3 to CA1 Schaffer collateral connections [20]. The hippocampus contains diverse interneuron types distributed across all layers. These include pyramidal basket cells extending dendrites into the stratum oriens and stratum radiatum, chandelier cells with dendrites spanning all hippocampal strata, and bistratified cells near the pyramidal cell layer. Interneuron-selective neurons are also distributed throughout the layers, with cell bodies found in different regions [20].

Glutamate functions as the principal excitatory neurotransmitter in the hippocampus, and small glutamatergic synapses represent the most prevalent type of synapse in this brain region. These synapses predominantly target dendritic spines located in the Schaffer collateral pathway, which transmit signals to CA1 pyramidal neurons. [89]. Within the CA1 pyramidal layer, there is a notable presence of GABA, the principal inhibitory neurotransmitter. The dendritic spines of CA1 pyramidal neurons, specifically in the stratum radiatum, are estimated to be around 30,000 in number, and the majority of these spines receive excitatory synaptic input [90].

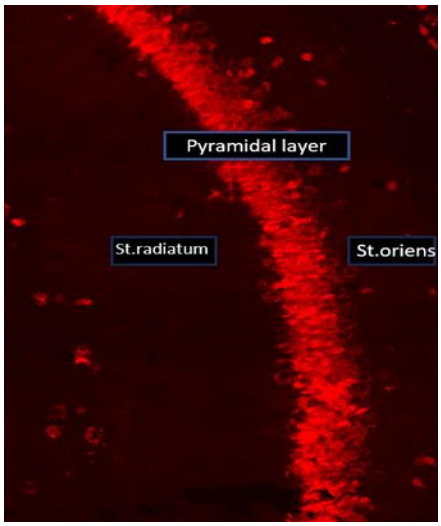

Figure 5: *Illustration of the CA1 region in the hippocampus, depicting various labeled regions, including the pyramidal layer, stratum radiatum, and stratum oriens.*

1.6 Characterizing Hippocampal Development and Neurogenesis in Mouse

In the developing mouse brain during embryonic and early postnatal stages, neural stem cells (NSCs) exhibit the capability to generate neurons and glial cells, including astrocytes and oligodendrocytes. The transition of NSCs from a proliferative and multipotent state into fully differentiated neurons and glial cells is termed neurogenesis and gliogenesis, respectively [91].

1.6.1 Dentate gyrus:

The dentate gyrus (DG) in the hippocampus undergoes a fascinating developmental process, starting during embryonic development and continuing throughout the postnatal phase. Granule cells in the dentate gyrus undergo a sequential developmental process, commencing from the primary dentate neuroepithelium situated around the dentate notch. This process occurs during the mouse's embryonic stages at E13.5 and E14. [87]. At the developmental stage of E15.5 in mice, a subset of cells generated within the primary dentate ventricular zone initiates migration towards the subpial region via the suprafimbrial region. This migratory phenomenon is referred to as "dentate migration, Interestingly, during this migration, these cells maintain their ability to proliferate while simultaneously playing a role in the formation of the secondary dentate matrix along their migratory route [87].

The maturation of neurons in the molecular cell layer (MCL) and the hilus of the dentate gyrus (DG) reaches completion around embryonic day 15 (E15). In contrast, the formation of the granule cell layer (GCL) in the DG begins at postnatal day 0 (P0) and does not reach full completion until postnatal week 3. The granular cells within the GCL are derived from precursor cells originating from all three matrices [92]. The characteristic shape of the GCL, with two blades, is influenced by the surrounding Cajal-Retzius cells and the pial surface. [91]. The glial scaffold and Cajal-Retzius cells play a vital role in the developmental process of the dentate gyrus (DG), directing the migration and organization of dentate precursor cells and granule neurons. This leads to the aggregation of neural progenitors at the hippocampal fissure, where they form the tertiary matrix and ultimately give rise to granule cells within the granule cell layer (GCL) [93].

In the early postnatal stages after birth, the tertiary matrix transitions to become the primary source of dentate progenitor cells and granule cells. As the second postnatal week progresses, proliferation becomes increasingly confined to a specific region called the subgranular zone (SGZ), where neural stem cells (NSCs) persist into adulthood [91].

At approximately E17.5 and 18.5 in mice, an early form of the dentate gyrus becomes evident. During late embryonic and early postnatal stages, a phenomenon known as the "second dentate migration" occurs, where cells migrate towards and reach the future dentate hilus.
Interestingly, these migratory cells preserve their capability for proliferation even within the hilus, and the designated area where these cells reside is denoted as the tertiary dentate matrix [87]. The subplate zone (SPB) structure appears at birth [94], while the infragranular zone (IPB) structure develops during the first postnatal week, coinciding with the peak generation of granule cells [76]. During this stage, granule cell generation becomes restricted to the tertiary matrix exclusively [91]. Subsequently, granule cells develop dendrites and form branches with dendritic spines in the following weeks. The foundation of the granule cell layer (GCL) is completed during the early postnatal period

due to the substantial generation of granule cells. Although neurogenesis reaches its peak during this early postnatal phase, it continues throughout adulthood [76]. However, following the early postnatal period, the origin of granule cells becomes increasingly limited, exclusively confined to the subgranular zone (SGZ), where they endure throughout an individual's lifespan [91].

1.6.2 CA1:

The generation of pyramidal neurons within the hippocampal CA1 region primarily occurs within the Ammonic neuroepithelium, predominantly from embryonic day 12 (E12) to E18. The peak period of pyramidal neuron generation in the CA1 region occurs at embryonic day 15 (E15), while in the CA3 region, it peaks at E14. However, the generation of these neurons continues until E18 [87]. Subsequent to their terminal mitotic division, post-mitotic neurons engage in a migratory phase lasting several days before undergoing differentiation into pyramidal neurons and ultimately positioning themselves in the pyramidal cell layer [95]. The formation of pyramidal neurons in the CA regions adheres to an inside-out gradient, where neurons are initially produced in the deepest layer closest to the striatum oriens and gradually accumulate toward the more superficial layer. In the CA3 region, neurons nearest to CA1 are generated initially, while those closest to the dentate gyrus (DG) are produced last. The maturation of neurons in the hippocampal pyramidal layer is completed by embryonic day 18 (E18) [96].

The majority of pyramidal neurons in this region are derived from the ventricular zone (VZ), but a smaller population also originates from basal progenitors in the subventricular zone (SVZ). The generation of pyramidal neurons in the CA regions follows an inside-out gradient, with neurons initially produced in the deepest zone of the layer, closest to the stratum oriens, and progressively accumulating towards the more superficial zone. In the CA3 region, neurons closest to CA1 are generated first, while those closest to the dentate gyrus (DG) are generated last. The formation of neurons for the hippocampal pyramidal layer is concluded by embryonic day 18 (E18) [87].

2. Hypothesis and project aims:

The DNA repair enzyme NEIL3 plays a crucial role in influencing the maturation and function of hippocampal neurons by shaping the transcriptome during development. Our observations indicate a prolonged maturation in mice lacking Neil3, and we have recognized genes with differential regulation that are essential for hippocampal development. Notably, *Neil3−/−* mice exhibit impaired spatial performance in the Morris Water Maze and a distinct synaptic composition in the hippocampus [41]. These findings suggest a unique role of NEIL3 in the regulation of hippocampal functions Furthermore, data from the Bjørås group proposes that the NEIL family of DNA glycosylases may play a crucial role in cognitive functions, particularly in learning and memory within the brain. Hence *Neil3-/-*have important role for both development and function of hippocampus.

The main goal of this project is to uncover novel insights into the influence of NEIL3 on the development and functioning of the hippocampus. This master's project aims to investigate:

- the impact of NEIL3 on the gene expression in the hippocampal subregions.
- the influence of NEIL3 in the organization of GABAergic inhibitory neurons.
- the role of NEIL3 in the postnatal maturation of hippocampal subregions.

3. Methodology

3.1 Mouse model:

Male NEIL3 knockout mice with C57BL/6N background and male wild type control mice were selectively bred at the Comparative Medicine Core Facility in the Norwegian University of Science and Technology (NTNU). The mice were given free access to both water and food and were kept under controlled environmental conditions, adhering to a 12:12-hour light-dark cycle. The room temperature in which the mice were housed was maintained at 25°C, aligning with the specific requirements of the research protocols. In this study, adult animals, which were examined in relation to spatial learning, were collected at three months of age. Meanwhile, for the postnatal developmental study, animals were obtained at different postnatal timepoints, including, postnatal day 2 (P2) and postnatal day 8 (P8). The collection of these animals was carefully planned and performed to ensure the integrity and quality of the samples and minimize the effect of external variables.

3.2 Ethical statement:

The experimental procedures involving animals in this study were carried out in strict adherence to the ethical guidelines for animal welfare as mandated by the Norwegian Animal Welfare Act. The Institutional Animal Care and Use Committee (IACUC) at the Norwegian University of Science and Technology (NTNU) approved all animal-related protocols. The animals were carefully monitored throughout the study for any indications of distress or discomfort, and all measures were taken to mitigate any such issues, as necessary. Special care was taken to ensure that the animals did not experience any pain or discomfort during the experimental procedures. The study was conducted in accordance with high scientific standards to uphold the integrity and quality of the experimental data. FOTS number 28340.

3.3 Heterozygous breeding

The breeding program was initiated by crossing wild-type (WT) mice with mice homozygous for a knockout of the Neil3 gene *(Neil3-/-),* which yielded heterozygous offspring *(Neil3+/-)* carrying one functional and one non-functional copy of the Neil3 gene. In a subsequent step, the *Neil3+/-* mice were interbred, resulting in the generation of offspring with three genotypes: wild type *(Neil3+/+),* heterozygous *(Neil3+/-),* and homozygous knockout *(Neil3-/-).* The animals were monitored daily to ascertain the time of pregnancy and were collected at various timepoints: postnatal day 2 (P2), postnatal day 8 (P8), and 3 months (3m).

3.4 Brain perfusion

Initially, the mouse was administered isoflurane (1 mL, Baxter, Cat. #1001936060) via a chamber to induce anaesthesia and elicit loss of consciousness. Following this, an intraperitoneal injection of pentobarbital (2 g/kg bodyweight) was administered to further anesthetize the animal. The efficacy of anaesthesia was confirmed by testing for pedal pain reflex.

After confirming successful anaesthesia, a V-shaped incision was made in the skin, each end reaching both armpits and to the lowermost part of the ribcage. The lower part of the ribcage was then horizontally dissected, exposing the abdomen. The abdomen was maneuvered to reveal the diaphragm, which was subsequently dissected. The remaining ribcage was then precisely cut down from the left, right, and superior aspects to allow for clear visualization and access to the heart. An 18-gauge needle, coupled with loaded with 50 ml of 0.9% Saline Solution, was employed to puncture the left ventricle. This system was connected to a BRAUN 3-way Connection Tube (BBRAUN Cat. #BRAU4098218) to facilitate the injection of the solution. To permit the efflux of blood, the right atrium was dissected using small scissors. Approximately 60 ml of 0.9% Saline Solution was gradually injected from syringe to flush the blood from the body.

Following perfusion, the head was severed, and the skin covering the skull was dissected to reveal the skull bones. The cervical vertebrae were taken out with forceps. The occipital, temporal, parietal and frontal bones were carefully removed using forceps to gain access to the brain. Finally, the brain was then scooped in swinging motion and stored in 4% paraformaldehyde. Prior to further analysis, the tissue samples were stored under appropriate conditions to maintain their integrity.

Brains were cut sagittal, the right half of the brain was obtained and preserved by freezing it in sections, utilizing a 4% paraformaldehyde (PFA) solution for storage. Conversely, the left half of the brain underwent microdissection, with specific attention to the DG, CA1, and CA3 regions. The dissected tissue underwent RNA extraction and subsequent reverse transcription quantitative polymerase chain reaction (RT-qPCR) before being promptly stored at -80 °C. Additionally, approximately 1 cm of the animal's tail was collected for genotyping purposes.

3.5 DNA preparation

To prepare DNA for genotyping analysis, 1mm tail samples were obtained and lysed in a lysis buffer (100 µl, consisting of 10mM Tris, 1M KCl, 0.4 % NP-40/Igepal CA630 Sigma,

and 0.1 % Tween 20), supplemented with Protein kinase K (2 µl) and incubated at 60°C overnight. The samples underwent heating at 95°C for 30 minutes, followed by full-speed centrifugation (14,000 rpm) for 20 minutes. The resultant DNA samples were then stored at -20°C until they were utilized in subsequent experiments.

3.6 PCR

The DNA obtained from the tail samples was purified and subsequently diluted to a 1:10 ratio. A PCR-mix was prepared by combining 1 µl of the diluted DNA with 2.75 µl of ddH2O, 5 µl of Taq Master Mix (Cat. #19J0801, containing 10XPCR Buffer, 2.5/10 mM dNTPs, 5U/µl paq5000, and 50 mM MgCl2), 0.5 µl of *Neil3* forward primer, 0.5 µl of *Neil3* reverse primer, and 0.25 µl of Primer KO for *Neil3*. The mixture was vortexed and centrifuged before subjecting it to the following PCR-program: 3 minutes at 95˚C followed by 38 cycles of denaturation at 95˚C for 30 seconds, annealing at 58˚C for 30 seconds, and extension at 72˚C for 60 seconds. This was followed by a final extension step at 72˚C for 5 minutes and holding the sample at 4˚C indefinitely.

Table 1: List of primers for PCR: Neil3, knock-out.

Gene	Sequence
Neil3	Forward: CTTGTTTTCCCACCACAATCTG
Neil3	Reverse: GTGGGCTGAAATTACACAAACAAT
Neil3 KO	Forward: GCCTCTGTTCCACATACACTTCAT
Neil3 KO	Reverse: GTGGGCTGAAATTACACAAACAAT

3.7 Gel electrophoresis

To prepare the gel, 2% agarose (LE Agarose, BioNordica, Cat. #BN50004) was dissolved in TAE-buffer (Tris Base, Glacial Acetic Acid, 0.5M EDTA) with 0.001% SYBR safe stain (ThermoFisher/Invitrogen, Cat. #S33102). The solution was then poured into a plastic gel holder fitted with an appropriate well-comb (BIORAD), and any entrapped air bubbles were removed using a pipette tip. After solidification of the gel, it was carefully transferred to the electrophoresis apparatus, filled with TAE-buffer.

The gel was loaded with 100 bp DNA ladder (New England Biolabs) in the first well, then 8µL of each sample was loaded. The controls used were Wild types and NEIL3 animals which have been previously genotyped. The gel was then subjected to an electric field at 120V for 40 minutes in a BIORAD electric chamber system, allowing the DNA fragments to migrate through the gel based on their size.

After the run, the gel was transferred to a ChemiDoc Imaging System (BIORAD) for visualization. The SYBR safe stain intercalates into the DNA and fluoresces when exposed to UV light, allowing for visualization of the DNA fragments. The resulting gel image was analysed to determine the size and quantity of the DNA fragments present in the samples.

3.8 Frozen sectioning

The brains samples were prepared for sectioning using a state-of-the-art cryotome (CryoStar NX70, Thermo Fisher). The cryotome chamber was maintained at a temperature of -20°C, while the section thickness was set to 30 µm. The right hemisphere was then carefully mounted onto a cryostat metal chip and secured using a suitable amount of Tissue OCT mounting medium (Q Path, Cat. #19G060001). To prevent crystal formation and minimize the freezing time, the brain tissue was rapidly frozen by exposing it to a PRF quick-freezing spray at -55°C.

After the brain sample being mounted onto a metal chip, it was firmly placed onto the cryobar of the cryotome to ensure complete freezing. The cutting blade and glass were adjusted, and the metal chip was accurately positioned for cutting. Subsequently, sagittal brain sections were acquired sequentially, by placing the first sections in well 1 and second in well 2 and so on. Individual sections were then transferred to a 24-well plate containing 2 mL of Phosphate buffered saline (PBS) 1X with 0.03% ProClin 300 in each well. To ensure precision, a specialized bent glass pipet was employed for the transfer of each section, and each section was evenly distributed so that the medial and lateral sections are equal in all wells. This approach allowed for consistent and accurate sample distribution across 6 wells of the 24-well plate. Specifically, the initial section was placed in the first well, the second section was positioned in the second well, and so forth. Once the seventh section was collected, it was placed into the first well, and the arrangement pattern continued.

The plate was stored at 4°C for further analysis. The use of PBS1X in conjunction with the antimicrobial agent ProClin 300 ensured the preservation of the tissue sections and protected them from contamination during storage. The importance of careful handling and preservation of tissue sections cannot be overstated, as it is essential to maintaining the integrity of the samples and preventing the loss of valuable data.

3.9 Immunohistochemistry

Immunohistochemistry (IHC) was performed on different brain samples to analyse various neurobiological markers, including proliferating cells (Ki67), neural progenital cells (Sox2) immature neurons (DCX), NeuroD1, mature neurons (NeuN) in the whole hippocampus and GABAergic interneurons GAD67, Parvalbumin and Somatostatin in regions of DG and CA1. The sagittal sections of a mouse brain were chosen for this experiment, different regions of the section are shown in the figure 6. The study involved the use of three naïve animals from each genotype (WT/*Neil3-/-*) and three trained animals from each genotype.

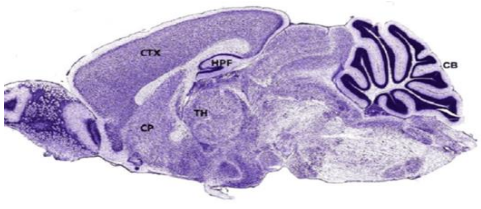

Figure 6: *Sagittal section of a mouse brain, showing different regions of the brain including the hippocampal formation (HPF), thalamus (TH), cerebellum (CB), and cortex (CTX). Sagittal section of the mouse brain, stained with Cresyl violet to highlight the hippocampus. This particular section is considered optimal for selection as it exclusively displays the medial aspect of the hippocampus, clearly delineating all components, including the dentate gyrus and hippocampus proper. Adapted from the Allen Brain Atlas online.*

3.9.1 Sorting of slices

The sorting of brain tissue sections was carried out using a bent glass pipette to delicately transfer 30 µm slices from a 24-well storage-plate to a large petri dish containing PBS1X. Two medial sections, displaying the Dorsal hippocampus from the right hemisphere, were subsequently chosen for each sample and placed in a 12-well plate filled with PBS 1X. The sections were meticulously chosen to maintain uniformity and consistency across all samples. both control and *Neil3-/-* samples were subjected to the same staining protocol for every experiment.

3.9.2 Antigen retrieval

Tissue fixation using formaldehyde can cause modifications to the tissue, which can lead to masking of antigens and hindrance in antibody binding. Therefore, an antigen retrieval step was implemented in this study to unmask antigens and facilitate antibody binding.

Sodium citrate (Trisodium citrate 5,5 hydrate, Merck Millipore 1.06431.100) at a concentration of 100mM and pH 6 was used for this purpose. It is further diluted by adding 600 µl of double distilled water in 400 µl of TriSodium Citrate to get the final concentration of 40mM. Eppendorf tubes were filled with 1 mL of the sodium citrate solution, with one tube designated for each sample. The sections were thoroughly washed once in fresh PBS in a 12-well plate before being transferred into Eppendorf tubes, which had been already preheated to 99°C. The sections were then incubated at this temperature for 4 min. After heating, the sections were left to cool down for 26 minutes. The samples were then washed three times with PBS1X for 5 minutes each to remove any excess solution.

3.9.3 Blocking

To prevent non-specific binding of antibodies or other reagents, blocking was performed on the sections. The slices were transferred directly from PBS1X to a 24-well plate containing 500 µL of blocking buffer composed of 5% normal goat serum (NGS), 5% bovine serum albumin (BSA), and 0.1% Triton X-100 in PBS. The plate was then placed on a shaker with a shaking frequency of 15 turns/min at room temperature for a duration of 2 hours.

3.9.4 Primary antibodies

In order to identify specific proteins of interest, primary antibodies were employed. The primary antibodies used in this study were used at different concentrations as shown in the Table 2 below.

To apply the primary antibodies, the sections were transferred from the blocking buffer into 24-well plates containing 200 µL of primary antibody solution. The primary antibodies were diluted in dilution buffer, which consists of 1% NGS, 1% BSA, and 0.1% Triton X-100 in PBS. The sections were carefully transferred into the wells while ensuring that they were submerged in the liquid and not in contact with the plastic. The plate was then sealed tightly with Parafilm (Bemis) to prevent evaporation and incubated overnight at 4°C with gentle shaking (15 turns/min) to allow for proper binding of the primary antibodies to their respective antigens.

3.9.5 Secondary antibodies

The sections were first washed in a 12 well plaque with PBS-T, which is a solution containing 0.1% Tween 20 in PBS. The washing process consisted of three rounds of gentle shaking on a shaker for 10, 20, and 30 minutes, respectively. To minimize potential photo-bleaching effects, all steps involving secondary antibody-containing solutions were performed under low lighting conditions or protected with aluminium foil when left for a long time. The secondary antibodies used were A555, which is an anti-Mouse IgG1 antibody, and A488, which is an anti-Rabbit polyclonal antibody, (Life Technologies) as shown in the table below. The A555 antibody was used to detect primary antibodies from the Mouse IgG1 isotype, while the A488 antibody was used to detect primary antibodies from rabbit polyclonal sources. The sections were subsequently moved to a 24-well plate containing 200 µL of the secondary antibody solution. This solution was prepared by diluting the secondary antibodies in the Dilution Buffer (1% NGS, 1% BSA, and 0.1% Triton X-100 in PBS). The plaque was closed and covered with tin foil and then incubated at room temperature (approximately 25°C) on a shaker under gentle shaking (15 turns/min) for 2 hours. It is worth noting that tin foil was used to protect the secondary antibody solutions from light, as exposure to light can lead to decreased fluorescence intensity and signal-to-noise ratio of the images obtained.

Table 2: The primary and secondary antibodies employed for immunohistochemistry (IHC) are outlined in the table below.

Primary antibodies	Isotype	Dilution	Manufacturer	Catalog number	RRID
Anti-NeuN	mIgG1	1:500	Merck Millipore	MAB377	AB_2298772
Anti-GAD67	mIgG2a	1:2000	Merck Millipore	MAB5406	AB_2278725
Anti-PV	rIgG	1:1000	Swant	PV25	AB_10000344
Anti-Somatostatin	rIgs	1:1000	Novus	156 003	AB_887694
Anti-Ki67	rIgG2a	1:500	Thermo Fisher	14-5698-82	AB_10854564
Anti-Sox2	rIgG	1:1000	Merck Millipore	AB5603	AB_2286686
Anti-NeuroD1	rIgG	1:2000	Synaptic Systems	226 003	AB_213725
Anti-DCX	rIgGs	1:1000	Abcam	AB18723	AB_732011
Secondary antibodies	**Isotype**	**Dilution**	**Manufacturer**	**Catalog number**	**RRID**
A488	mIgG1	1:1000	Invitrogen	A-21121	AB_2535764

A488	rIgGs	1:1000	Invitrogen	A-11008	AB_143165
A555	rIgGs	1:1000	Invitrogen	A-21431	AB_2535852
A647	Guinea pig	1:1000	Invitrogen	A-21247	AB_141778
A647	ratIgG2a	1:1000	Invitrogen	51-4321-81	AB-2716967

3.9.6 Mounting

In the mounting step, the brain sections were transferred into a 12 well plaque filled with PBS-T. The plaque was sealed and covered with tin foil to prevent exposure to light. The sections were then washed thrice for 10 min, 20 min and 30 min respectively under gentle shaking on a shaker to remove any excess debris. The slices were individually transferred to a large petri dish filled with PBS. Each slice was mounted onto a ThermoFisher Superfrost Plus slide using a soft-bristled thin brush and positioned in the same orientation. Once all slices had been mounted onto the slides, these were left to dry overnight in darkness at room temperature. To ensure efficient staining, DAPI solution (1:1000 in PBS) was slowly added to all three brain slices and incubated for 1 minute at room temperature under a fume hood. The slides were then transferred to a metal slide holder and dipped sequentially into three different beakers, two of them filled with PBS, and third beaker filled with distilled water to remove any residual DAPI solution. In case of detachment, the slices were reattached and allowed to dry for 30 min before continuing the protocol.

The final step involved drying the slides for 1 hour before adding a drop of Prolong Gold Antifade Mountant with DAPI (ThermoFisher/Invitrogen, Cat. #P36935) to the centre of the hippocampus and covering them with a cover slip. Before scanning, the slides were left to dry for at least 24 hours to ensure complete drying before scanning for optimal image quality.

3.10 Immunohistochemistry, paraffin section staining

The dissected brains were found to be highly delicate, making frozen sectioning unsuitable. To preserve their structural integrity, the brains were embedded in paraffin wax, facilitating subsequent sectioning, and mounting on glass slides. The paraffin-embedding procedure was conducted by the Histology Core, NTNU.

3.10.1 Deparaffinization and Rehydration Procedure for Tissue Samples

The deparaffinization and rehydration process involved the following steps: Initially, the samples were subjected to incubation at 58°C for 15 minutes. Subsequently, they were directly placed in glass jars containing various solutions and underwent sequential incubation as follows: two cycles of Xylene (Sigma-Aldrich, 247642) for 5 minutes each, two cycles of 100% Ethanol (VWR, 20821.296) for 3 minutes each, 96% Ethanol (VWR, 20824.296) for 1 minute, 70% Ethanol (VWR) for 1 minute, and finally, PBS 1X.

3.10.2 Antigen Retrieval and Pre-treatment

For antigen retrieval, an antigen retrieval buffer consisting of 40 mM Trisodium citrate 5,5 hydrate (Merck Millipore 1.06431.100) at pH 6 was prepared and boiled on a hot plate within a pressure cooker. Subsequently, tissue sections were immersed in the boiling buffer and allowed to incubate for 3 minutes. To cool down the sections, the pressure cooker was placed under cold running water for 10 minutes. After this stage, the specimens were moved to a glass container containing PBS-T (1X PBS + 0.1% Tween20). The slides were delicately dried with a dust-free paper cloth, and a hydrophobic circle was drawn around the tissue using a Dako Pen. Inside this designated circle, PBS-T enriched with 0.25% Triton was administered using a pipette, and the slides were allowed to incubate at 4°C for a duration of 15 minutes.

3.10.3 Staining Procedure and Antibody Incubation

Following the deparaffinization and rehydration procedures, the slides underwent thorough drying using a dust-free paper cloth, ensuring no contact with the tissue. The Dako Pen was then utilized to redraw a hydrophobic circle. For the blocking step, 200µl of blocking buffer (PBS + 5% NGS + 5% BSA + 0.1% Triton X-100) was pipetted into the designated hydrophobic circle and allowed to incubate for 1 hour at room temperature. Subsequent to this, the slides underwent three washes, each lasting 10 minutes, in PBS-T. The hydrophobic circle was redrawn, and primary antibodies, diluted in a dilution buffer (PBS + 0.5% NGS + 0.5% BSA + 0.1% Triton X-100), were applied within the circle. The slides were then incubated overnight at 4°C with the primary antibodies.

The next day, brain sections were washed three times with PBS-T at room temperature (5, 10, and 20 minutes each). The hydrophobic circle was redefined, and secondary antibodies, diluted in buffer, were added within the circle for a 1-hour incubation. After another three washes with PBS-T, sections were briefly immersed in DAPI solution, washed again, air-dried, and cover-slipped with mounting oil, securing the cover glass with nail polish.

3.11 Confocal Microscopy:

The sections underwent imaging using a confocal microscope (Zeiss LSM 880 Z1, Jena, Germany) equipped with a Plan-Apochromat 40x/1.4 Oil DIC M27 objective (Carl Zeiss, Jena, Germany) and ZEN black edition software (Carl Zeiss). The specific anatomical location of interest was visually identified using the ocular in fluorescence mode, with a 365 nm laser to visualize the DAPI stain. Subsequently, adjustments to the confocal

microscope settings, including pinhole, intensity, and gain, were made to optimize visualization.

A tile scan of the NeuN channel was performed to obtain an overview, and the number of tiles was adjusted to encompass the entire area of interest. In the maturation study, the entire hippocampus was imaged, while for the GABAergic inhibitory interneurons study DG and CA1 regions were captured separately.

The z-stack interval, determined through the NeuN channel, was chosen to encompass all cellular layers within the tissue. Additionally, the z-stack interval was fine-tuned for each batch utilizing the "optimize stacks" function. The "tile scan" function with the NeuN channel was employed to adjust the number of tiles, ensuring coverage of the specific region in the image. Subsequently, all channels were activated, and the image was captured. Consistency in settings was maintained for each batch.

3.12 Imaris Image Analysis

In this study, the mouse samples imaged by confocal fluorescence microscopy were subjected to 3D analysis using Imaris 9.4 software (Oxford Instruments). This software was used for image processing, visualization, and quantification of complex 3D datasets.

3.12.1 Ki67, NeuN, NeuroD1

Firstly, a 3D surface of the hippocampus was generated from the stack images. Subsequently, the surface was masked for the specific channel, facilitating the identification of positive cells. The number of these cells within the hippocampus was counted after selecting the appropriate threshold and eliminating artifacts detected by the software. Finally, the density of positive cells was quantified as the number of cells per cubic millimetre for meaningful comparisons between samples, by using the formula.

$$\frac{\text{Positive stained cells}}{\text{mm}^3} = \frac{\text{Number of positive cells}}{\text{volume } [\text{mm}^3]}$$

3.12.2 Sox2, Dcx:

The analysis of Sox2 and DCX involved setting a threshold to distinguish positive signals from background noise. The thresholding approach was utilized, enabling the software to exclusively detect the number of voxels in the hippocampus. The expression level was then presented as a voxel ratio, calculated using the provided formula.

$$\text{Sox2/DCX expression } = \frac{\text{Number of voxels}}{\text{volume } [\text{mm}^3]}$$

3.12.3 GAD67, PV, Somatostatin:

Inhibitory neurons within the DG and CA1 were meticulously quantified manually using the slice-view to avoid any potential counting artifacts. To determine the number of positive cells per mm³ in each specific region, a customized formula was employed for individual calculations. This approach ensured accurate and reliable quantification of inhibitory neurons in each distinct hippocampal region of interest.

$$\frac{\text{Positive stained cells}}{\text{mm}^3} = \frac{\text{Number of positive cells}}{\text{volume } [\text{mm}^3]}$$

3.13 ImageJ

ImageJ software (Fiji v1.53, NHI, and LOCI Wisconsin) was utilized to generate representative images from the immunohistochemical (IHC) stainings. A maximum intensity z-stack projection, with an equal number of stacks for each channel, was created. Following this, the individual channel images were combined to produce a composite image representing both channels.

3.14 Graph-pad prism

Statistical analysis was performed using Prism 9 software (GraphPad Software, Version 9.3.1) to evaluate differences in neuronal populations between wild-type and mutant mice. The averaging of two samples per animal was performed, resulting in a single value per animal. To ensure data reliability, a rigorous approach was adopted. Initially, a mathematical model was utilized to identify potential outliers within the dataset. For the postnatal timepoints P2 and P8 data analysis a two-way ANOVA was employed, followed by a Tukey multiple comparison test, to assess and compare data among the different groups. A normality test was conducted to ascertain the distribution of the data, subsequently, two-tailed unpaired t-test was employed to assess the statistical significance of differences in the number of neurons per volume between 3 months old wild-type and mutant mice in subregions of hippocampus.

3.15 RNA Extraction

A needle-scratch technique, performed by Marion Silvana was devised to accurately isolate hippocampal subregions, minimizing the risk of contamination from neighbouring anatomical areas. This study involved the use of 3-month-old mice, comprising five wildtype (WT) and five *Neil3-/-* mice as the experimental cohort. To isolate RNA from these samples, we utilized the widely recognized QIAGEN RNeasy RNA isolation kit, known for its established reliability in the field.

To initiate the RNA extraction procedure, aseptic techniques were employed, including cleaning the work surface with 70% ethanol followed by treatment with either RNase Away or RNase Zap to eliminate any RNase contamination. Tissue obtained from hippocampus region were transferred to a Bead Rupter collection tube containing beads and 350 µl of RLT buffer supplemented with beta mercaptoethanol (1:100) was added. The tubes were homogenized for 10 seconds in a rotor-stator homogenizer, and then centrifuged at maximum speed (~12000 rpm) for three minutes to pellet any debris.

After obtaining the flow-through from the previous step (approximately 350 µl), 350 µl of 70% ethanol were added and was thoroughly mixed by pipetting. The resulting mixture (700 µl) was then gently added to a QIAGEN RNeasy spin column (Cat. 74104), which was carefully positioned in a 2 ml collection tube. After securing the tube, the column was subjected to a brief centrifugation step, first at 2000 rpm for 15 seconds, and then at 10000 rpm for another 15 seconds.

Next, 700 ml of RW1 buffer were introduced into the RNeasy spin column, and the tube was subsequently sealed before centrifugation at 2000 rpm for 15 seconds, followed by 10000 rpm for 15 sec. The resulting flow-through was discarded, and then 500 microliters of RPE buffer, which had been activated with 44 ml of ethanol per 11 ml of buffer, were

added to the same spin column. After sealing, the tube was centrifuged again at 2000 rpm for 15 seconds and then at 10000 rpm for another 15 seconds, with the flow-through being dispose of once again. The process was then repeated with another 500 ml of RPE buffer. Again, the flow-through was discarded, and the column was then positioned in a new 2 ml collection tube. Every drop of liquid near the ring of the membrane was collected and placed at the centre of the membrane, and then the tube was sealed and centrifuged for 1 minute at 10000 rpm. Subsequently, the RNeasy spin column was placed into a 1.5 ml Eppendorf tube, and 30 ul of RNase-free water were introduced directly onto the column membrane. The tube was then sealed and allowed to sit for 1 minute. Afterward, it was centrifuged for 1 minute at 2000 rpm, followed by another 1 minute at 10000 rpm to effectively elute the RNA and the process was repeated using 20 ul of RNase-free water to further elute any remaining RNA left. Finally, 1 microliter of each tube was quantified using the Nanodrop device.

3.15.1 DNase treatment

To initiate the DNase treatment, the RNA sample was combined with 5 µl of 10X TURBO DNase I buffer and 1 µl of TURBO DNase enzyme, and thorough mixing was achieved by pipetting. Following this, the mixture underwent a 30-minute incubation in a thermo-mixer at 37°C to facilitate the DNase activity. For deactivation of the DNase enzyme, 5 µl of DNase inactivation reagent was added to the sample and mixed thoroughly using pipetting. Subsequently, the sample was left to incubate at room temperature for 5 minutes, and the tube was flicked three times during this duration. The sample was subsequently centrifuged at 14000 rpm for 90 seconds, allowing for separation of the supernatant and pellet. Finally, the RNA supernatant was carefully transferred to a new tube for further downstream analysis.

3.15.2 cDNA synthesis

To initiate cDNA synthesis, an appropriate amount of RNA is required to ensure uniform cDNA production among all samples. The amount of RNA required was calculated using Excel software. Once the necessary RNA amount is determined, a master mix was prepared by combining essential reagents, including 10X RT buffer, 25X dNTP mix, 10X RT random primers, and MultiScribe Reverse Transcriptase 50units/µl from High-Capacity cDNA Reverse Transcription Kit (Cat. 4368814).

Subsequently, 5.8 µL of the master mix was added to each PCR stripe tube, followed by an appropriate volume of RNA. If the RNA volume is less than 14.2 µL, nuclease-free water can add to achieve a total volume of 14.2 µL. After centrifugation, the tubes were subjected to the cDNA program using a thermocycler. The cDNA program entails incubation at 25°C for 10 minutes, followed by incubation at 37°C for 2 hours, and a final incubation at 85°C for 5 minutes. Finally, the tubes were cooled to 4°C.

3.16 Primer Testing

In this research method, the first crucial step is to identify a specific region within the gene of interest that is unique and not found in other genes, ensuring primer specificity. Subsequently, the selected primers undergo rigorous laboratory testing using PCR with cDNA from the target organism. This testing evaluates primer performance in terms of specificity, efficiency, and reliability for amplifying the desired gene fragment.

3.16.1 Primer selection

The primers are designed based on the sequence of interest and are critical components for PCR amplification. The process involves utilizing bioinformatics tool such as NCBI's Primer-BLAST tool to predict and optimize the binding of the primers to the target sequence to achieve high specificity and efficiency.

Primer design started by accessing the NCBI webpage and selecting the nucleotide database. The target gene Neil3 was searched to obtain its accession number. This accession number was then used in the Primer BLAST webpage for customizing primer design parameters.

The temperature range for PCR annealing was selected, typically between 55 and 65 degrees Celsius, to optimize primer binding. The desired product length was specified within a range of 75 to 200 base pairs, as shorter amplicons tend to amplify more efficiently than longer ones. Additionally, the "one primer must be specific" option was selected to ensure that the primers will not bind to non-target regions of the genome. After these parameters have been set, Primer-BLAST generates a list of potential primers and evaluates their quality using various criteria, such as specificity, melting temperature, and secondary structure formation. The tool also provides the option to select variants and search for the most suitable primer pair.

The primers were ordered from Custom DNA Oligos from Merck.

3.16.2 Formation of aliquots:

Upon receipt of the selected and ordered primers, the primers are received in the concentration of 1µM. To prepare the primers for testing, a dilution step is required to achieve a final concentration of 10µM. To accomplish this, 10µL of the primer solution is combined with 90µL of nuclease-free water to yield a final volume of 100µL.

This process is carried out for both the forward and reverse primers separately. Aliquots were prepared from the primer stocks to ensure stable, long-term storage and repeated use in subsequent experiments. These aliquots were stored at -20°C until needed for further experiments. The use of appropriate and optimized primer concentrations in PCR reactions is essential for efficient amplification of target DNA sequences and to minimize non-specific amplification.

3.16.3 Primer testing

To verify the efficiency and specificity of the primers designed for a specific gene, a master mix recipe composed of 5µL of Taq polymerase, 3µL of water, 0.5µL of the forward primer, and 0.5µL of the reverse primer was followed. To generate enough volume for 8 PCR tubes, the recipe was multiplied by 8. Next, 8µL of the cDNA sample was added to the master mix, and the resulting solution was mixed thoroughly by vertexing. The resulting mix was then distributed evenly into eight PCR tubes, each containing 9µL of the mix. By replicating the PCR reaction in multiple tubes, any variation in the amplification efficiency of the primers due to thermal variations within the thermocycler can be detected. In addition, master mix was prepared, using water instead of cDNA as a control.

To determine the optimal annealing temperature for the primers, different temperature range was selected. The PCR was performed, and the results were analysed using gel electrophoresis. 1µL of DNA loading dye was added in each sample before running the gel to ensure proper functioning. The band patterns were then compared to the expected

amplicon size, and the annealing temperature that gave the most specific and efficient amplification was selected for further experiments.

3.17 qPCR

To investigate the levels of differentially expressed genes in *Neil3-/-* as compared to wildtypes was investigated by using Reverse Transcription-quantitative Polymerase Chain Reaction (RT-qPCR). RNA extracted from DG and CA1 was utilized to construct the cDNA. A 1 ng/µL cDNA dilution was prepared for each sample, and a Master Mix, comprised of Power SYBR Green, forward primer, reverse primer, and nuclease-free H2O, was meticulously assembled per primer. To ensure consistency, the constructed cDNA and Master Mix were dispensed into 96-well plates at a 3:10 ratio. Subsequently, gene expression analysis was carried out using the StepOnePlus RT-PCR system, provided by Applied Biosystems, Thermo Fisher Scientific, along with the corresponding software for data acquisition and analysis. Notably, nine different primers were applied to evaluate the expression of the target genes in each region. To comprehensively assess the alterations in gene expression, both wild-type and mutant cDNA samples were examined, enabling a comparative analysis to discern whether the target gene was upregulated or downregulated. Beta-actin was employed as a reference gene for normalization, ensuring the accuracy of the gene expression results. The gene expression levels were determined using the comparative CT method, with beta-actin primer serving as the internal control.

3.17.1 qPCR Analysis

In qPCR analysis, a systematic process is followed to evaluate gene expression. This involves the selection of an endogenous control gene, designation of a calibrator as the reference sample, and calculation of the Cycle Threshold (Ct) value. The Delta Ct (ΔCt) is computed by subtracting the Ct of the test gene from the Ct of the endogenous control. The Delta Delta Ct (ΔΔCt) quantifies the fold change in gene expression concerning the calibrator. To assess the reliability of the results, the standard deviation (SD) is determined based on technical replicates, with results being considered unreliable if SD exceeds 0.25. The Relative Quantification (RQ) indicates the fold change in gene expression relative to the calibrator.

Additionally, the mentioned variables like ΔΔCq, 2-ΔΔCq, media2-ΔΔCq KOClone3, DS2-ΔΔCq KOClone3, and pruebaT are used to further refine and interpret the qPCR data. These parameters aid in comparing and analyzing gene expression levels, assessing variability, and determining the significance of changes in gene expression under various experimental conditions.

4. Results:

The primary objective of this project includes: The investigation into the impact of NEIL3 on the gene expression in the hippocampal subregions. Various primers were employed, and the differentially expressed genes were analysed using quantitative polymerase chain reaction (QPCR) techniques. Another significant aspect of the study focused on understanding how NEIL3 influences the organization of GABAergic inhibitory neurons. Comparative analyses were conducted between naïve WT and *Neil3-/-* mice, as well as between trained WT and *Neil3-/-* mice. The primary regions of interest were the dentate gyrus (DG) and cornu ammonis 1 (CA1) in 3-month-old mice. The third segment of the investigation delved into the role of NEIL3 in the postnatal maturation of hippocampal subregions. The study specifically examined the maturation and organization of distinct neuronal populations during postnatal days 2 (p2) and 8 (p8). This analysis provided valuable insights into how NEIL3 may contribute to the developmental processes in these crucial early stages.

4.1 NEIL3 impacts specific gene expression in the hippocampal subregions.

4.1.1 Genotyping:

Samples from mice aged 3 months were efficiently collected simultaneously. The brains were extracted, fixed in 4% paraformaldehyde (PFA), and tail samples were obtained for genotyping. The purpose of genotyping is to identify and confirm the genetic makeup of mice, specifically with regards to the presence or absence of the NEIL3 gene. This process involves using a specific set of primers to amplify DNA, and the resulting patterns of DNA bands indicate whether the mice are wild-type (WT), heterozygous (*Neil3+/-),* or knockout (*Neil3-/-)* for the NEIL3 gene. Figure below, show different sizes of DNA amplification in *Neil3-/-* mice (160bp DNA band), WT mice (260bp DNA band), and *Neil3+/-* heterozygous mice (both bands). These findings clearly demonstrate the successful generation of WT and *Neil3-/-* mice. The homozygous *Neil3-/-* and wildtype samples were used in this study.

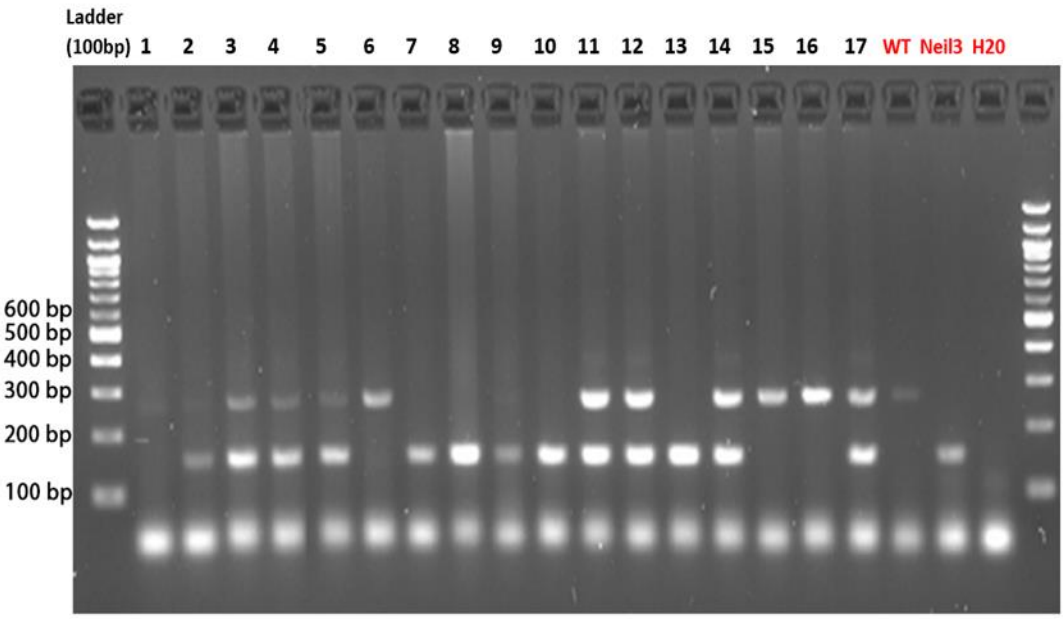

Figure 7: *illustration of an agarose gel containing PCR samples derived from various 3 months old mouse DNA samples. Utilizing the specified primer pair (refer to sectionx, table x), amplification results in a distinct 160bp band for Neil3-/- samples and a distinct 260bp band for WT samples. Heterozygous samples (Neil3-/+), exhibiting bands at both 160bp and 260bp, can be identified. The gel lanes, from left to right, include DNA ladder, PCR samples from different DNA samples labeled 1 to 17, Neil3-/- standard (Neil3-/-), WT standard (WT), and a negative control (NC) represented by water with primers.*

4.1.2 RNA extraction and cDNA synthesis:

This method involved the use of 3-month-old mice, comprising five wildtype (WT) and five *Neil3-/-.* The experimental objective was to acquire cDNA for the purpose of testing primers and conducting quantitative polymerase chain reaction (QPCR) to identify genes exhibiting differential expression. Subsequently, cDNA was synthesized, with a concentration of 25 nanograms per microliter, as indicated in the table below.

Table 3: Concentration of RNA and constructed cDNA: The measurements were acquired using a Nanodrop spectrophotometer. The concentration of each RNA and constructed cDNA is expressed in ng/µL.

DG Samples (3m)	RNA Concentration (ng/µL)	Constructed cDNA (ng/µL)
WT	61.8	25
WT	68.04	25
WT	63.51	25
WT	192.99	25
WT	65.53	25

Neil3	80.32	25
Neil3	83.91	25
Neil3	48.08	25
Neil3	78.25	25
Neil3	40.74	25

CA1 Samples (3m)	**RNA Concentration (ng\µL)**	**Constructed cDNA (ng/µL)**
WT	113.7	25
WT	54.44	25
WT	75.94	25
WT	52.94	25
WT	112.38	25
Neil3	61.38	25
Neil3	81.02	25
Neil3	93.36	25
Neil3	91.81	25
Neil3	141,14	25

4.1.3 Modulation of Gene Expression in Hippocampal Regions following Depletion of NEIL3

Transcriptomic studies from Ye's group identified differentially expressed genes (DEGs) in NEIL3-depleted hippocampal subregions (Fig. 8A). Distinct DEGs involved in the G-protein signalling were identified in the hippocampal CA1 and DG regions. These NEIL3-targeted genes were further analysed by RT-qPCR.

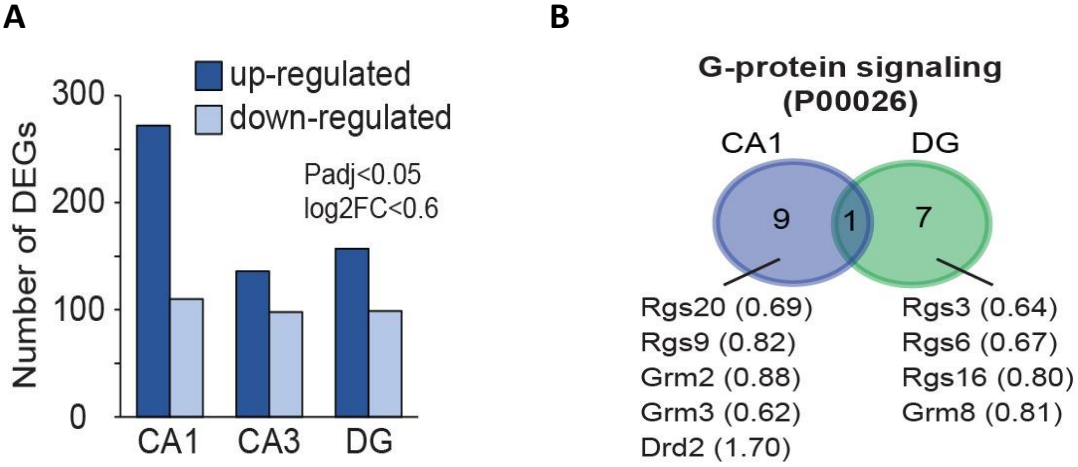

Figure 8: A) *The number of up-regulated and down-regulated gene in each region of hippocampus,* ***B)*** *overlapping DEGs between the CA1 and DG region involved in the G-protein signalling. This data is obtained by Ye's group.*

Hence, the inquiry arose as to whether the absence of this NEIL3 in the knockout mutant could induce alterations in the hippocampal transcriptome. To investigate this, a gradient PCR was employed utilizing prepped cDNA, and the optimal annealing temperature for each primer, yielding a singular specific band on the agarose gel, was determined. Subsequently, the qPCR was performed, *providing a quantification of the complementary DNA (cDNA) level of the target gene. This measurement reflects the messenger RNA (mRNA) level of the tested gene.* To examine the expression levels of genes that differ between *Neil3-/-* and wildtype mice in DG and CA1, a comprehensive analysis using two-way ANOVA was conducted followed, by a Tukey multiple comparison test, to assess and compare data among the different groups.

Quantitative analysis of Drd2 gene expression

Dopamine exerts its influence by slowly modulating the rapid transmission of neurotransmitters through its G-protein-coupled receptors [97]. Dopamine D2-like receptors (D2R) play a crucial role in modulating the excitability of hippocampal neurons, actively contributing to the regulation of synaptic plasticity. Additionally, they play a key role in encoding memories dependent on the hippocampus and contribute to the regulation of affective states [98].

A gradient PCR, utilizing prepared cDNA, determined the optimal annealing temperature (56.9°C) for drd2, resulting in a singular specific band on an agarose gel. Subsequent

qPCR, with beta-actin as a housekeeping gene, was conducted, revealing potential distinctions among the samples, as illustrated in Figure 9 (a,b). The results suggest a downregulation of Drd2 levels in *Neil3-/-* mice compared to wild types, although this difference did not reach statistical significance. The findings indicate that the absence of Neil3 had a relatively modest impact on Drd2 gene expression, with its expression slightly higher in CA1 compared to the DG.

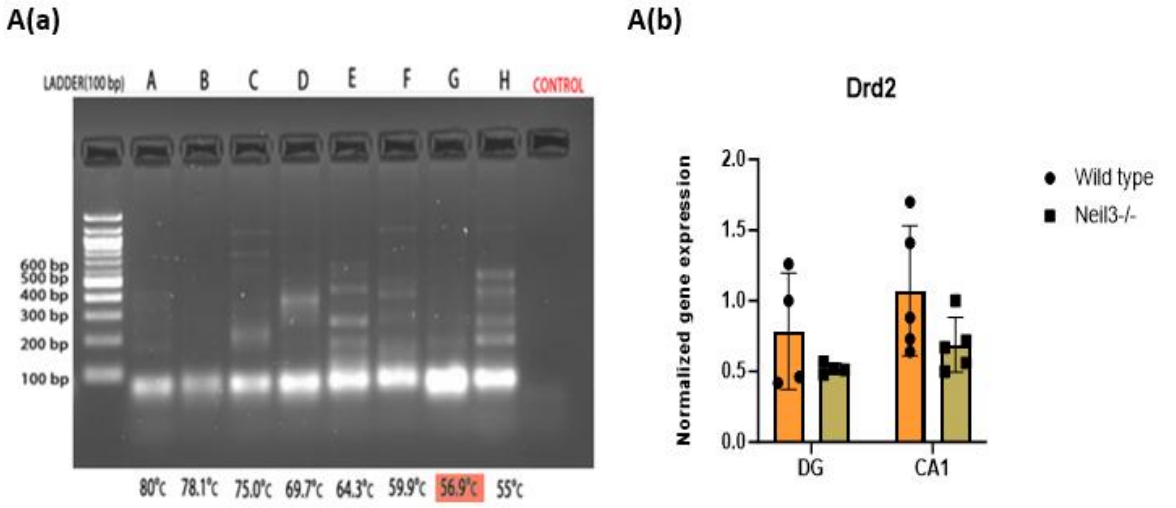

Figure 9: A(a). *Illustration of gradient PCR results demonstrating the optimal annealing temperature for Drd2 primer, identifying 56.9°C as the most effective working temperature.* ***A(b)****. Graphical representation depicting the regulation of Drd2 in the DG and CA1 hippocampal regions, with the Y-axis indicating the normalized drd2 expression. The error bars illustrate the standard error of the mean (SEM), and significance was deemed for a p-value below 0.05.*

Quantitative analysis of Grm gene family

Glutamate, the principal excitatory neurotransmitter in the brain, carries out its functions through both ionotropic and metabotropic receptors. These receptors are pivotal in sustaining synaptic plasticity and are integral to the mechanisms underlying memory and learning Glutamate (Glu) is the primary excitatory neurotransmitter in the mammalian brain [99]. Consequently, Glu acts not only as a rapid transmitter in neuron-to-neuron communication but also as a signalling molecule with enduring effects on neuronal structure and function. Glutamate neurotransmission plays a crucial role in modifying synaptic activity associated with learning, memory formation, and the normal development of the nervous system [100].

I investigated the impact of *Neil3-/-* on the expression of the Grm gene family using targeted gradient PCR with prepared cDNA. Specific bands corresponding to optimal annealing temperatures were visualized on the agarose gel as highlighted by red. Subsequent qPCR, employing beta-actin as a reference gene, revealed noticeable differences among the samples, as depicted in Figure 10A. The findings indicate no change in the gene expression of Grm2, whereas an upregulation of Grm3 in CA1 wildtype compared to the *Neil3-/-* counterpart was observed, demonstrating a statistically significant increase; $p = 0.0095^{**}$, two-way ANOVA, n = 5 mice per time point. In contrast, Grm8 exhibited upregulation only in the CA1 region of *Neil3-/-*; $p = 0.0264^{*}$, while its expression remained unchanged in the DG, suggesting no discernible effect of NEIL3 on Grm8 gene expression in the DG. My results suggest that NEIL3 indeed has an important role for gene regulation in the DG and CA1 of the hippocampus.

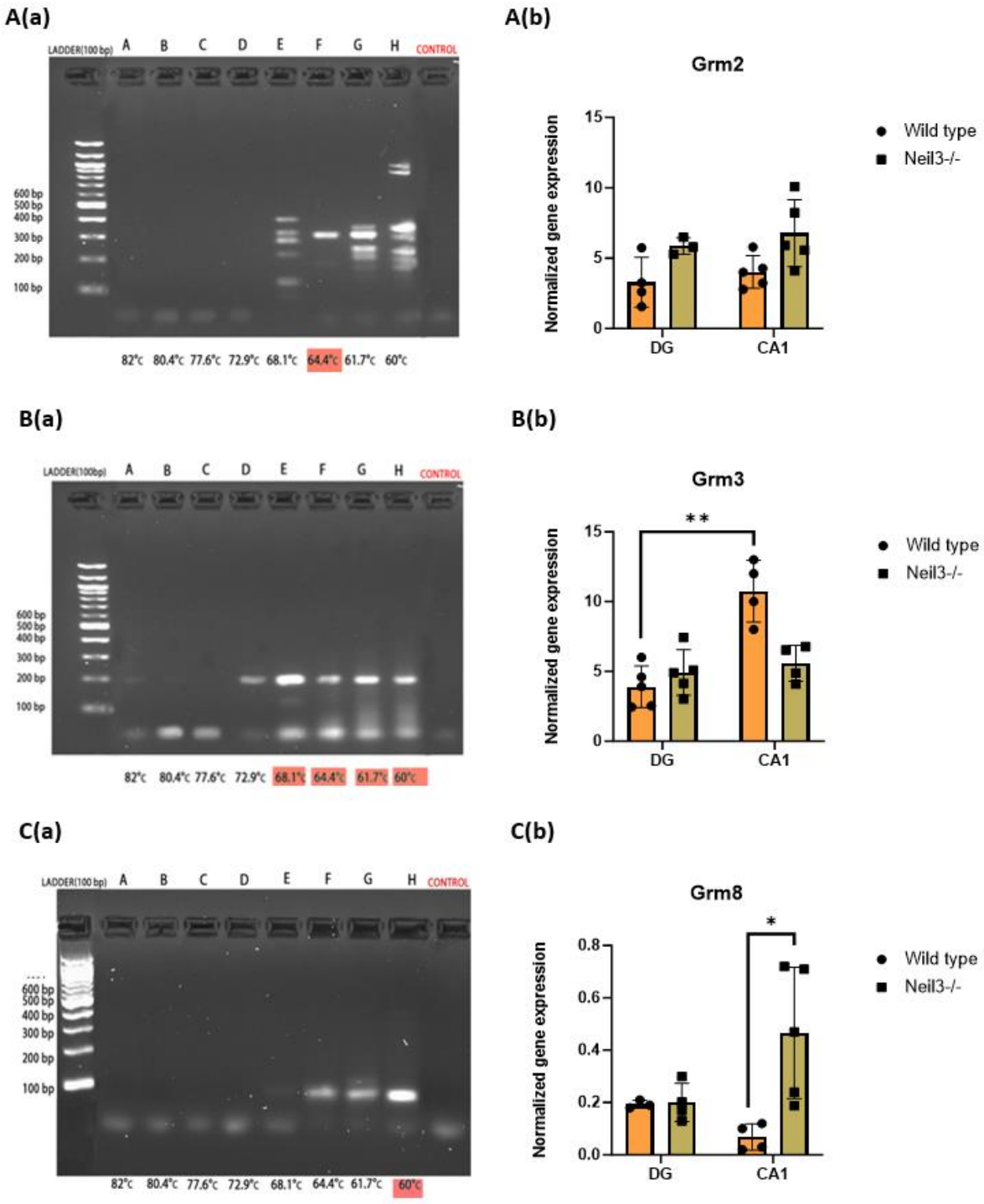

Figure 10: A(a), B(a), C(a) *depict gradient PCR results highlighting the optimal annealing temperature for Grm2, Grm3, and Grm8 primers, identifying the most effective working temperature as indicated by red.* ***A(b), B(b), C(b)*** *demonstrate the graphical representation illustrating that the qPCR results provide a quantification of the complementary DNA (cDNA) level of the target gene. This measurement reflects the messenger RNA (mRNA) level of the tested gene. The error bars illustrate the standard error of the mean (SEM), and significance was deemed for a p-value below 0.05.*

Quantitative analysis of RGS gene family

Regulators of G-protein signaling (RGS) proteins exert potent modulation on the functioning of heterotrimeric G-proteins by enhancing the GTPase activity of G-protein α subunits. The intricate regulation provided by RGS genes contributes to the finely tuned signaling processes within the hippocampus, influencing synaptic plasticity, neurotransmission, and ultimately impacting cognitive functions.

I investigated the impact of *Neil3-/-* on the expression of the Rgs gene family using gradient qPCR with prepared cDNA. Distinct bands, indicative of optimal annealing temperatures, were observed on the agarose gel. Subsequent qPCR, with beta-actin as a reference gene, revealed notable differences among the samples, as seen in Figure 11A.

The results indicate an upregulation of Rgs3 in the DG of *Neil3-/-*, coupled with downregulation in CA1 *Neil3-/-* ; p = 0.021*, two-way ANOVA, n = 5 mice per time point. Remarkably, a significant disparity in RGS regulation is observed between DG and CA1. Conversely, RGS6 displays upregulation in CA1 for both genotypes but is statistically reduced in DG for both, with p values of 0.0485* for DG and 0.0191* for CA1. In contrast, RGS9 exhibits downregulation in DG knockout compared to Wild type. RGS16 demonstrates a statistically significant increase in *Neil3-/-* DG, p= 0.0008***. Moreover, RGS20 shows downregulation in *Neil3-/-* CA1 region, displaying a significant difference; p=0.0141*. My results suggest that NEIL3 indeed has an important role for gene regulation in the DG and CA1 of the hippocampus.

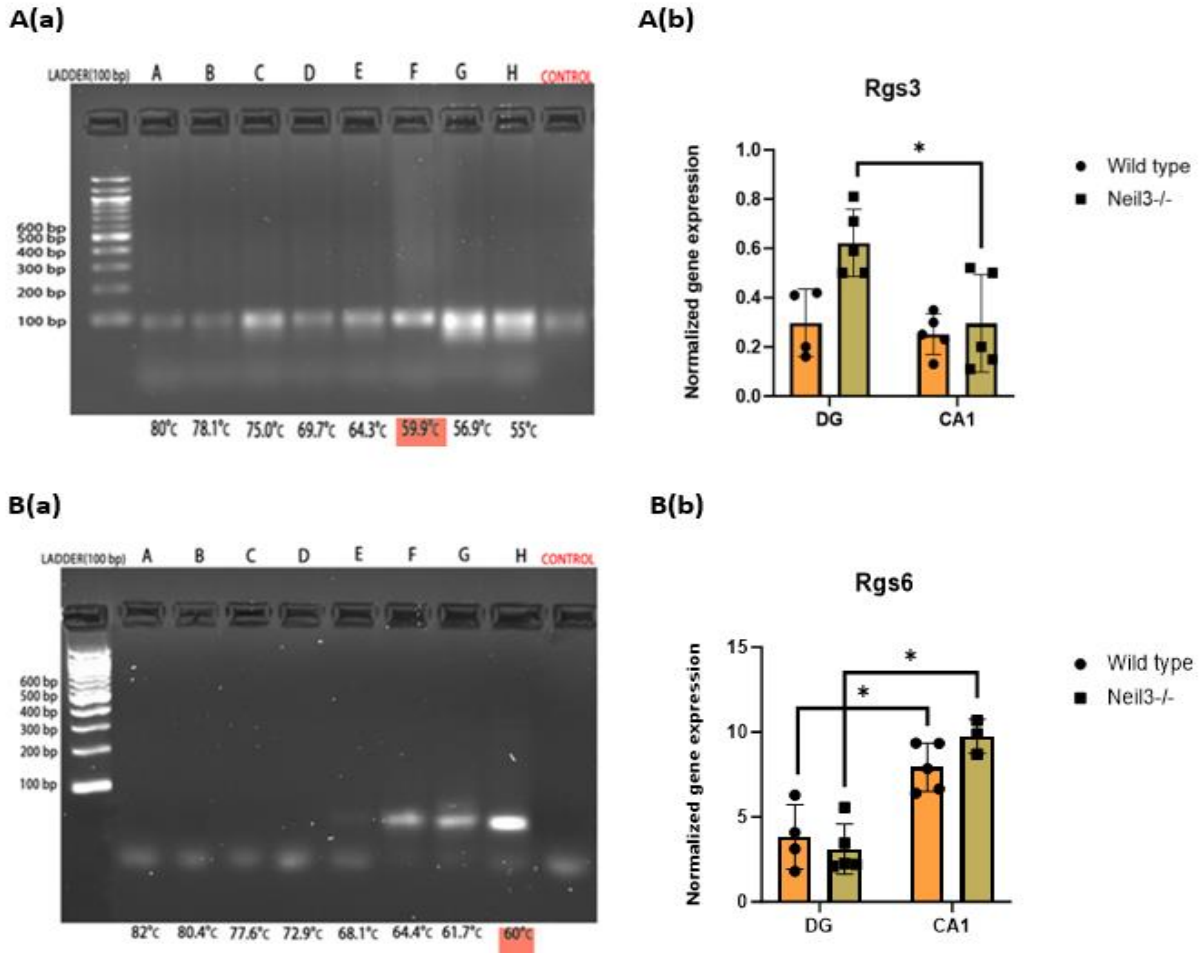

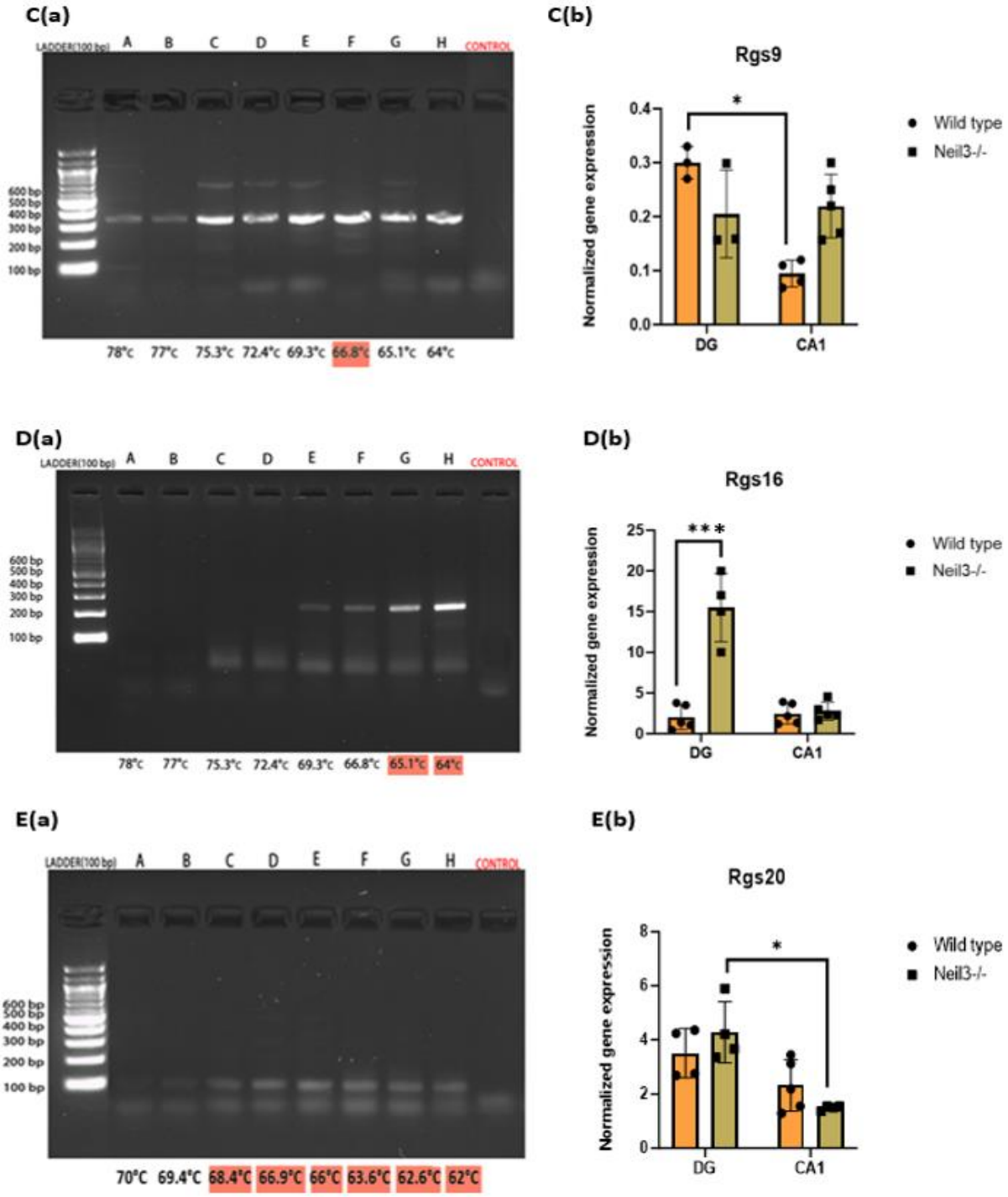

Figure 11: A(a), B(a), C(a) *depict PCR results highlighting the optimal annealing temperature for Rgs3, Rgs6, and Rgs9, Rgs16, Rgs20 primers, identifying the most effective working temperature as indicated by red.* ***A(b), B(b), C(b)*** *demonstrate the graphical representation illustrating the regulation of primers in the DG and CA1 hippocampal regions, with the Y-axis indicating the cycle threshold values. The error bars illustrate the standard error of the mean (SEM), and significance was deemed for a p-value below 0.05.*

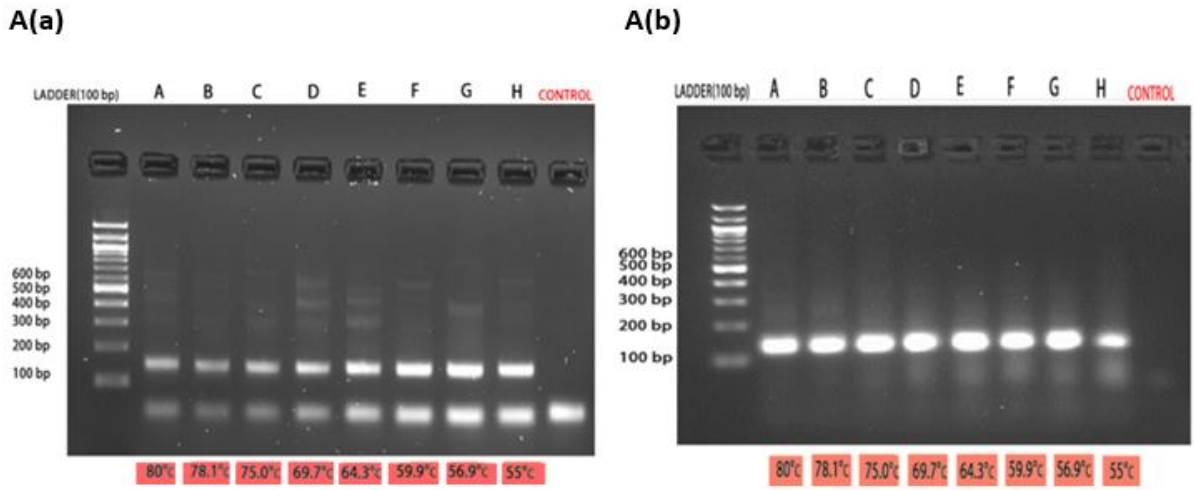

Figure 12: *Illustration of PCR results depicting the housekeeping genes used as controls in the QPCR experiment.* ***A(a)*** *presents the results for GAPDH, and* ***A(b)*** *shows the results for Beta-actin.*

The primers selected for the study were determined based on their optimal annealing temperatures. The optimal annealing temperature is crucial for ensuring the specific binding of primers to the target DNA, facilitating the amplification of the desired product. Therefore, primers lacking specificity, as evidenced by the absence of a distinct band, were excluded from further experimentation. Detailed information, including the specific sequences of all tested primers, can be found in the provided appendix (Table 4), where the chosen primers for subsequent experiments are highlighted in yellow.

4.2 Exploring the influence of NEIL3 in the organization of GABAergic inhibitory neurons.

The hippocampal circuitry is characterized by the intricate interplay between excitatory hippocampal neurons and inhibitory interneurons [101]. Despite the predominance of excitatory neurons within the hippocampus, inhibitory interneurons play a pivotal role in maintaining the delicate balance between excitation and inhibition within the hippocampal circuitry [102]. These interneurons establish connections with various neuron types, thereby modulating the activity of the hippocampal circuitry and regulating overall circuit activity [103]. This regulatory function is achieved through the synaptic release of gamma-aminobutyric acid (GABA), which serves as the principal inhibitory neurotransmitter in the cortex [103].

The maintenance of the excitation-inhibition balance in hippocampal neuronal activity is considered crucial for normal memory and learning processes, often accompanied by an elevation in gamma-aminobutyric acid (GABA) release and inhibitory synaptic plasticity [104]. Furthermore, there is supporting evidence suggesting that the impairment of GABAergic interneuron activity has negative consequences on cognitive functions [104].

GABA, a neurotransmitter in the brain, is synthesized from glutamic acid through the action of the enzyme glutamic acid decarboxylase (GAD). GAD has two gene variants, GAD2 (GAD65) and GAD1 (GAD67). GAD can exist as homo- or heterodimers of GAD65 and GAD67. While GAD65 is predominantly located in nerve terminals, GAD67 is distributed throughout the cell body and nerve terminals. During embryonic brain

development, GAD67 plays a significant role in GABA production, with GAD65's contribution increasing postnatally. In the adult brain, approximately 50–70% of total GABA is produced by GAD65, with the remainder attributed to GAD67. Both isoforms contribute to GABA production in the adult brain. The developmental patterns of GAD65 and inhibitory neuronal transmission appear parallel. GABAA receptor subtypes also change during brain development [105].

Interneurons in the neocortex are classified based on neurochemical properties, revealing the three primary classes: parvalbumin-expressing (PV+), somatostatin-expressing (SOM+) and 5-HT3A receptor-expressing (5HT3A-receptor+). Each class includes various subgroups. Additional classification studies, incorporating morphological, electrophysiological, and neurochemical properties, may identify more cell types. In the hippocampus, at least 10 GABAergic cell types are proposed, and a similar diversity is expected in the neocortex [106]. Utilizing double labeling immunocytochemistry and an extensive array of antibodies, including PV, SOM, CR, VIP, NPY, and CCK, uncovered additional subtypes of interneurons [107].

In the dentate gyrus (DG), interneurons are primarily located in the granular cell layer and the hilus [108, 109] and in CA1 they are situated in the whole region. The present study aimed to assess whether NEIL3 influences the organization of GABAergic interneurons in the hippocampal subregions. To achieve this objective, immunohistochemistry (IHC) was employed with antibodies against GAD67, Parvalbumin (PV), and Somatostatin. This investigation sought to determine whether the quantity of these cells in the DG and CA1 zones is affected in *Neil3-/-* mice. Naïve WT and *Neil3-/-* mice (3 months old) with and without behavioral training were used in this study.

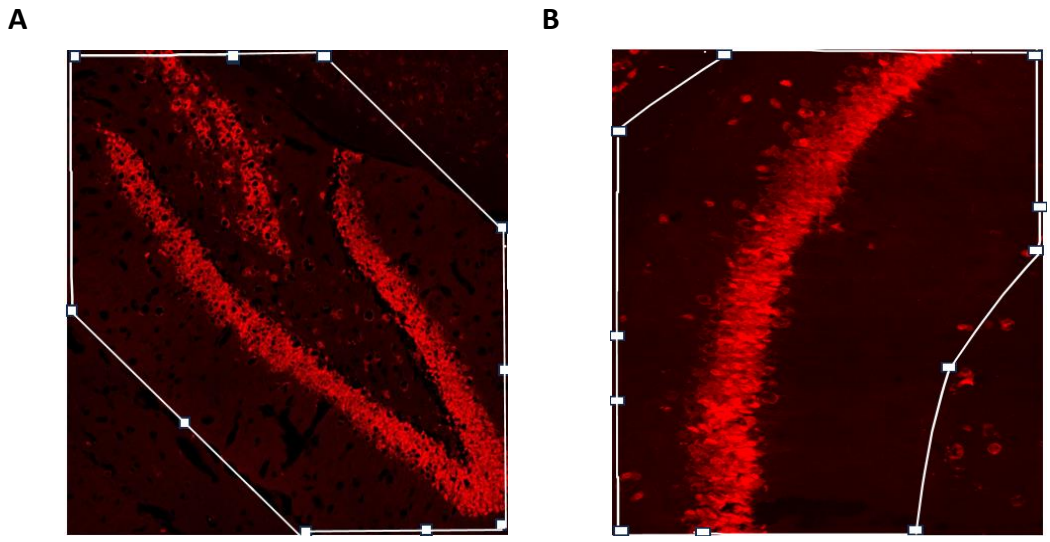

Figure 13: *Demonstration of the selected area in Imaris software for cell counting in specific regions of the hippocampus.* ***A)*** *illustrates the selection of the DG region in the software.* ***B)*** *depicts the CA1 region, showcasing how the region was chosen in the software for subsequent analysis.*

4.2.1 Monitoring Gad67-positive interneurons in DG

GAD67, an enzyme responsible for synthesizing gamma-aminobutyric acid (GABA) upon activation [109], serves as a widely utilized marker for GABAergic interneurons [122]. Consequently, GAD67 can be employed as an indicator for recently active GABAergic inhibitory neurons.

As illustrated in Figure 14A, GAD67-positive cells were detected in the dentate gyrus (DG) granular zone, hilus, and molecular layer. To quantify the number of GAD67-positive cells, the hippocampal DG was imaged using confocal fluorescence microscopy (Zeiss LSM880, Z-stack (25), tile (2x3)), and the GAD67-positive cells in the DG granular zone were assessed using the 3D-image analysis software Imaris 9.4. The number of GAD67-positive cells was determined based on the cell count per tissue volume (mm^3) in the DG. (Figure 14C).
A significant reduced density of GAD67-positive cells was detected in the dentate gyrus (DG) of *Neil3-/-* mice compared to wild-type counterparts (Figure 14C). (n(naïve WT) = 3.20 cells/ mm^3, n(naïve *Neil3-/-*) = 1.34 cells/ mm^3; p = 0.0355*; two-tailed unpaired t-test; n = 3 mice per time point), similarly in the group of animals subjected to behavioural training (n(Trained WT) = 2.05 cells/mm^3, n(Trained *Neil3-/-*) = 1.15 cells/mm^3; p = 0.0152*; n = 3 mice per time point.

In addition, the proportion of GAD67-positive neurons from total DG neurons was assessed (Figure 14D). The quantification provides additional validation for the observed distinctions between the two groups (n(naïve WT) = 1.58%, n(naïve *Neil3-/-*) = 0.975%; p = 0.0059**, (n(trained WT) = 1.84%, n(trained *Neil3-/-*) = 0.948%; p = 0.0059**; two-tailed unpaired t-test; n = 3 mice per time point.

The quantification methods, as outlined earlier, consistently verified significant distinctions between wild type and *Neil3-/-* in both groups. By combining the cell count per cubic millimetre data from three animals in each group, a comprehensive result was derived from six animals in total for two group. This provided conclusive evidence of these distinctions, as shown in Figure 14E.

These findings suggests that the absence of NEIL3 impacts the quantity of GABAergic interneurons in the hippocampal DG, highlighting a noteworthy reduction in the inhibitory network in knockout mice.

A

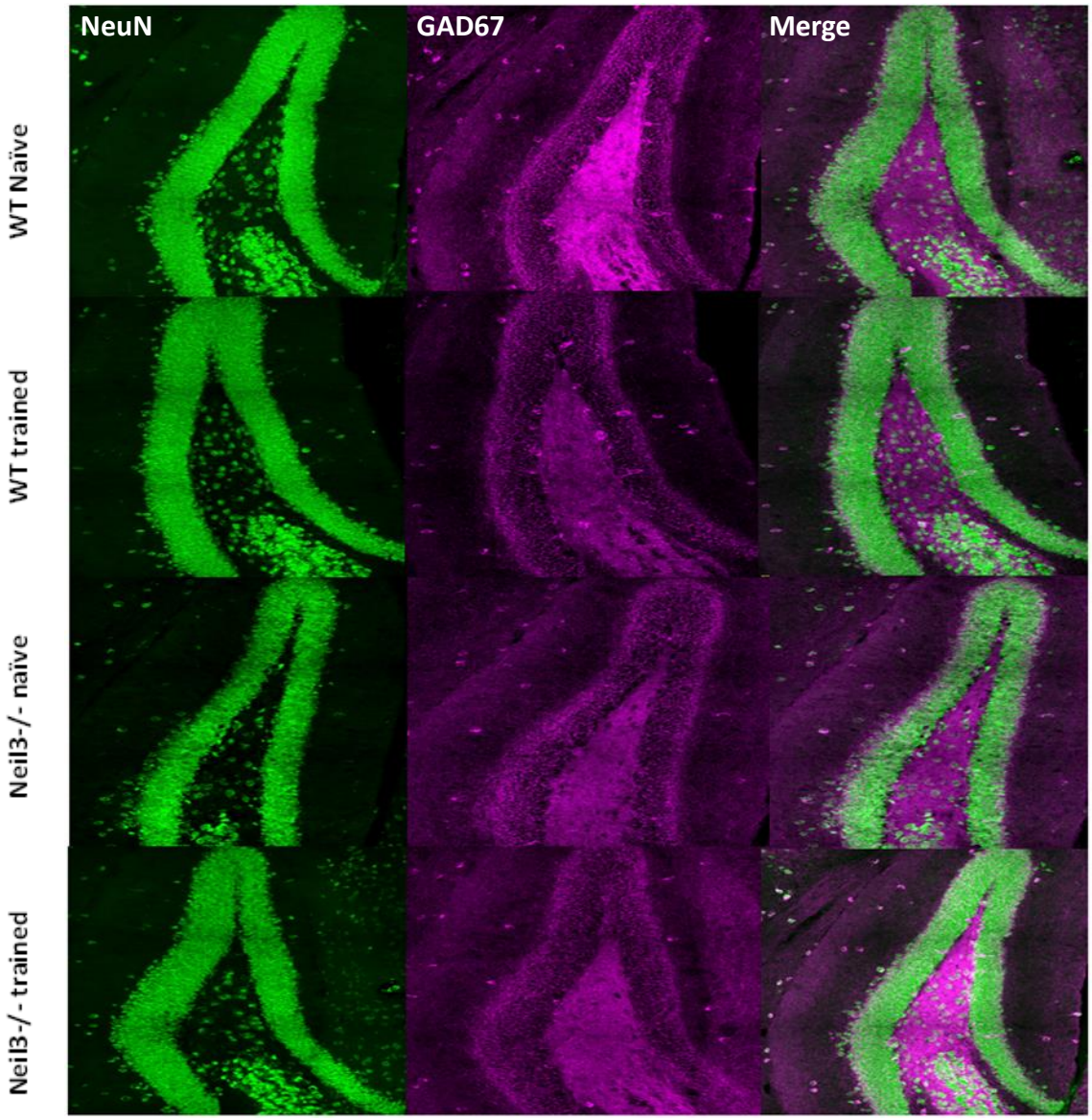
NeuN
GAD67
Merge
WT Naïve
WT trained
Neil3-/- naïve
Neil3-/- trained

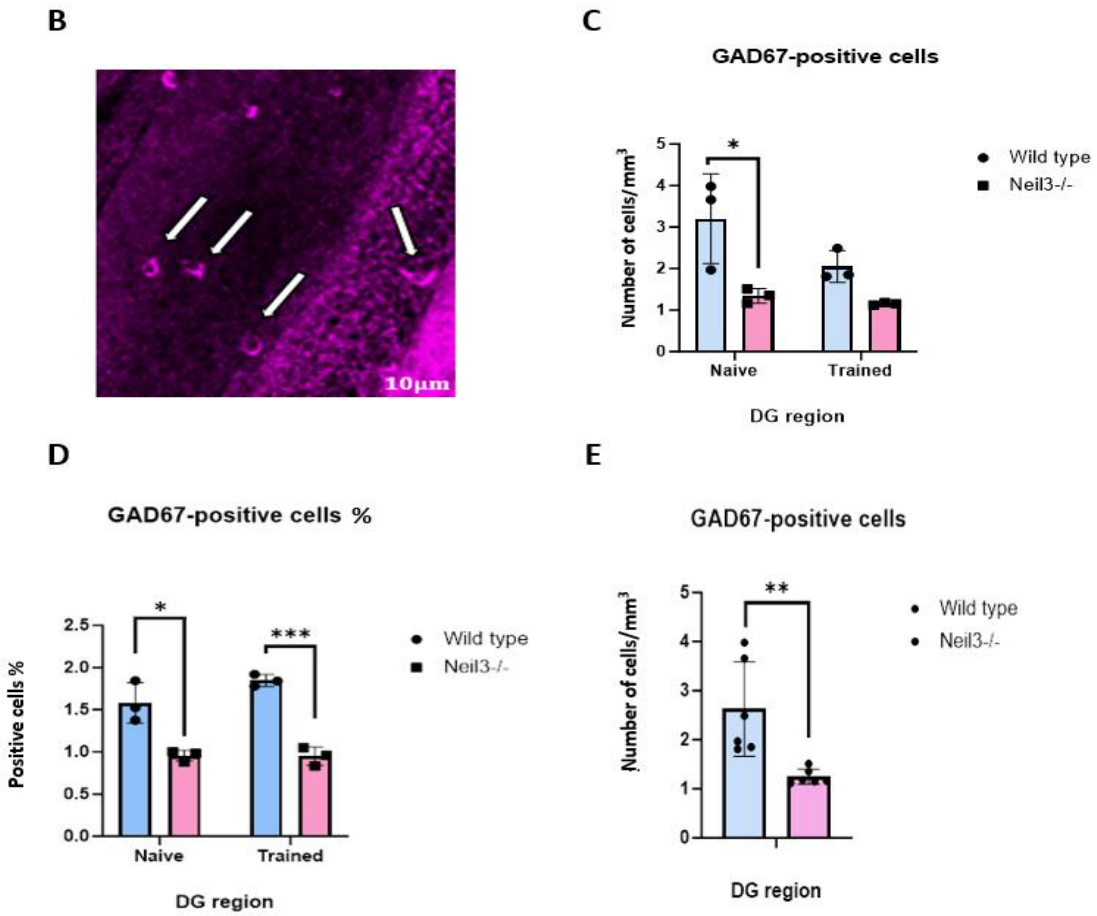

***Figure 14**. **A)** Illustrative confocal images of immunostained samples from the dentate gyrus (DG) are displayed featuring **A)** naïve and trained wild-type and Neil3-/- mice. Each image is sequentially displayed for NeuN (green), GAD67 (magenta), and the merged channels. Scanning was conducted using a Zeiss LSM880, employing a Plan-Achromat 40x/NA 1.4 oil immersion objective (Z stack (25), tile (2x3)). Following this, each image was subjected to additional processing using ImageJ (Fiji v1.53) to produce a maximum intensity z-stack projection (n(z stacks) = 20) **B)** A representative image of GAD67+ cells counted using Imaris 9.4. The image is acquired following the above description. The scale bar is 10 µm. **C**. A representative graph illustrating GAD67+ cells per volume, counted using Imaris 9.4, is displayed. Statistical analysis was performed using GraphPad Prism 10.1.2 with a two-tailed unpaired t-test; n = 3 mice per time point. The error bars illustrate the standard error of the mean (SEM), and significance was deemed for a p-value below 0.05 **D.** The proportion of GAD67-positive neurons from total DG neurons is assessed **E)** A representative graph illustrating GAD67+ cells per volume, n = 6 mice per time point.*

4.2.2 Monitoring Gad67-positive interneurons in CA1

Similarly, a reduced density of GAD67-positive cells was also detected in the CA1 region of *Neil3-/-* mice compared to wild-type counterparts (n(naïve WT) = 3.27 cells/mm³, n(naïve *Neil3-/-*) = 1.76 cells/mm³; p = 0.0196*; two-tailed unpaired t-test; n = 3 mice per time point), as well as the group of animals subjected to behavioural training (n(Trained WT) = 2.58 cells/mm³, n(Trained *Neil3-/-*) = 1.59 cells/mm³; p = 0.0085**; n = 3 mice per time point).

In addition, the proportion of GAD67-positive neurons from total CA1 neurons was assessed (Figure 14D). The quantification provides additional validation for the observed

distinctions between the two groups. (n(naïve WT) = 4.46%, n(naïve *Neil3-/-*) = 2.51%; p = 0.0035**, (n(trained WT) = 4.20%, n(trained *Neil3-/-*) = 2.38%; p = 0.0035**; two-tailed unpaired t-test. The results yielded statistically significant findings, consistent with previous results.

Confirmation methods for quantification consistently validated the significant distinction between wild type and *Neil3-/-* in both groups. Combining data obtained by quantification of cell count per cubic millimetre from three animals in each group, presented definitive evidence of these distinctions, as depicted in graph 15D.

This finding indicates that NEIL3 depletion influences the number of GABAergic interneurons in the hippocampal CA1, demonstrating a significantly diminished inhibitory network in knockout mice.

A

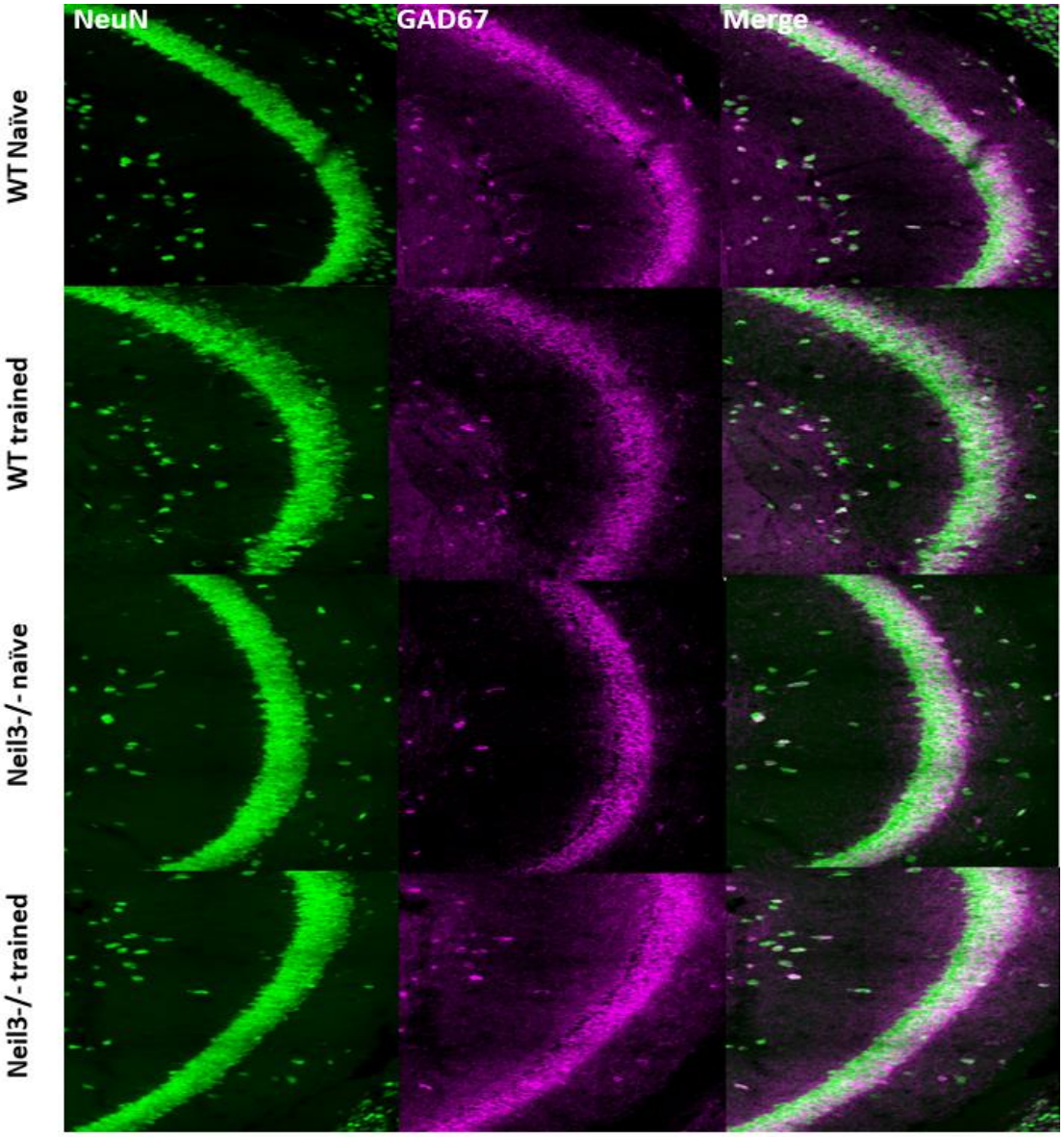

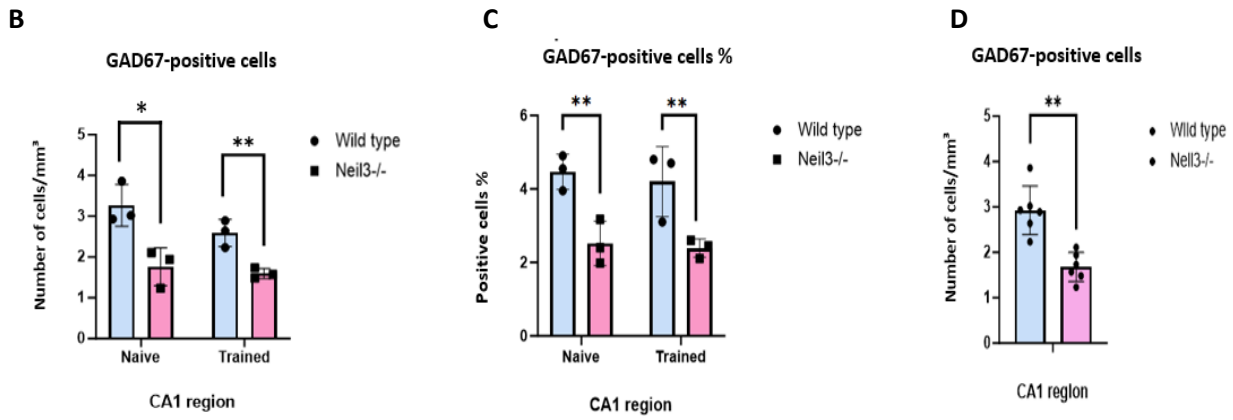

Figure 15: A) *Illustrative confocal images of immunostained samples from the CA1 are displayed, featuring a) naïve and trained wild-type and Neil3-/- mice. Each image is sequentially displayed for NeuN (green), GAD67 (magenta), and the merged channels. Scanning was conducted using a Zeiss LSM880, employing a Plan-Achromat 40x/NA 1.4 oil immersion objective (Z stack (20), tile (2x3)). Following this, each image was subjected to additional processing using ImageJ (Fiji v1.53) to produce a maximum intensity z-stack projection (n(z stacks) = 15).* ***B****). A representative graph illustrating GAD67+ cells per volume, counted using Imaris 9.4, is displayed. Statistical analysis was performed using GraphPad Prism 10.1.2 with a two-tailed unpaired t-test; n = 3 mice per time point. The error bars illustrate the standard error of the mean (SEM), and significance was deemed for a p-value below 0.05* ***C)*** *The proportion of GAD67-positive neurons from total CA1 neurons is assessed* ***D)*** *A representative graph illustrating GAD67+ cells per volume, n = 6 mice per time point.*

4.2.3 Monitoring PV-positive interneurons in DG

Parvalbumin (PV) serves as a calcium-binding protein expressed in a specific subtype of interneurons, functioning as a marker for PV-interneurons. Notably, PV-inhibitory interneurons are predominantly GABAergic [108]. Parvalbumin (PV) cells constitute the predominant category among inhibitory cells, accounting for 30–50% of all inhibitory interneurons. While PV cells exhibit some heterogeneity, they appear to share common features. The aim is to determine whether this subtype of interneurons specifically reduced in *Neil3-/-* knockout mice or not.

As shown in Figure 16A, PV-positive neurons were visualized in DG by IHC. A significant decreased density of PV-positive cells was detected in the dentate gyrus (DG) of *Neil3-/-* mice compared to their wild-type counterparts (n(Naïve WT) = 1.03 cells/mm³, n(Naïve *Neil3-/-*) = 0.492 cells/mm³; p = 0.0269*; two-tailed unpaired t-test; n = 3 mice per time point. In the group of animals that underwent behavioural training, a decline in the density of PV-positive cells was noted in *Neil3-/-*; however, this difference did not achieve statistical significance.

In addition, the proportion of PV-positive neurons from total DG neurons was assessed (Figure 16D). The quantification provides additional validation for the observed distinctions between the two naïve groups (n(naïve WT) = 0.52%, n(naïve *Neil3-/-*) = 0.26%; p = 0.0021*; two-tailed unpaired t-test; n = 3 mice per time point.

The outlined quantification methods consistently confirmed substantial differences between the wild type and *Neil3-/-* in both groups. The combination of cell counts per cubic millimetre data from three animals in each group resulted in a comprehensive

analysis from six animals in total for both groups. This collective approach offered conclusive evidence of the observed distinctions, illustrated in graph 16E.

These findings suggests that the absence of NEIL3 impacts the quantity of PV interneurons in the hippocampal DG, highlighting a noteworthy reduction in the inhibitory network in knockout mice. Moreover, changes in the balance between excitatory and inhibitory neurotransmission can impact the survival and function of inhibitory neurons. Disruptions in this balance may lead to a reduction in PV-positive neurons.

A

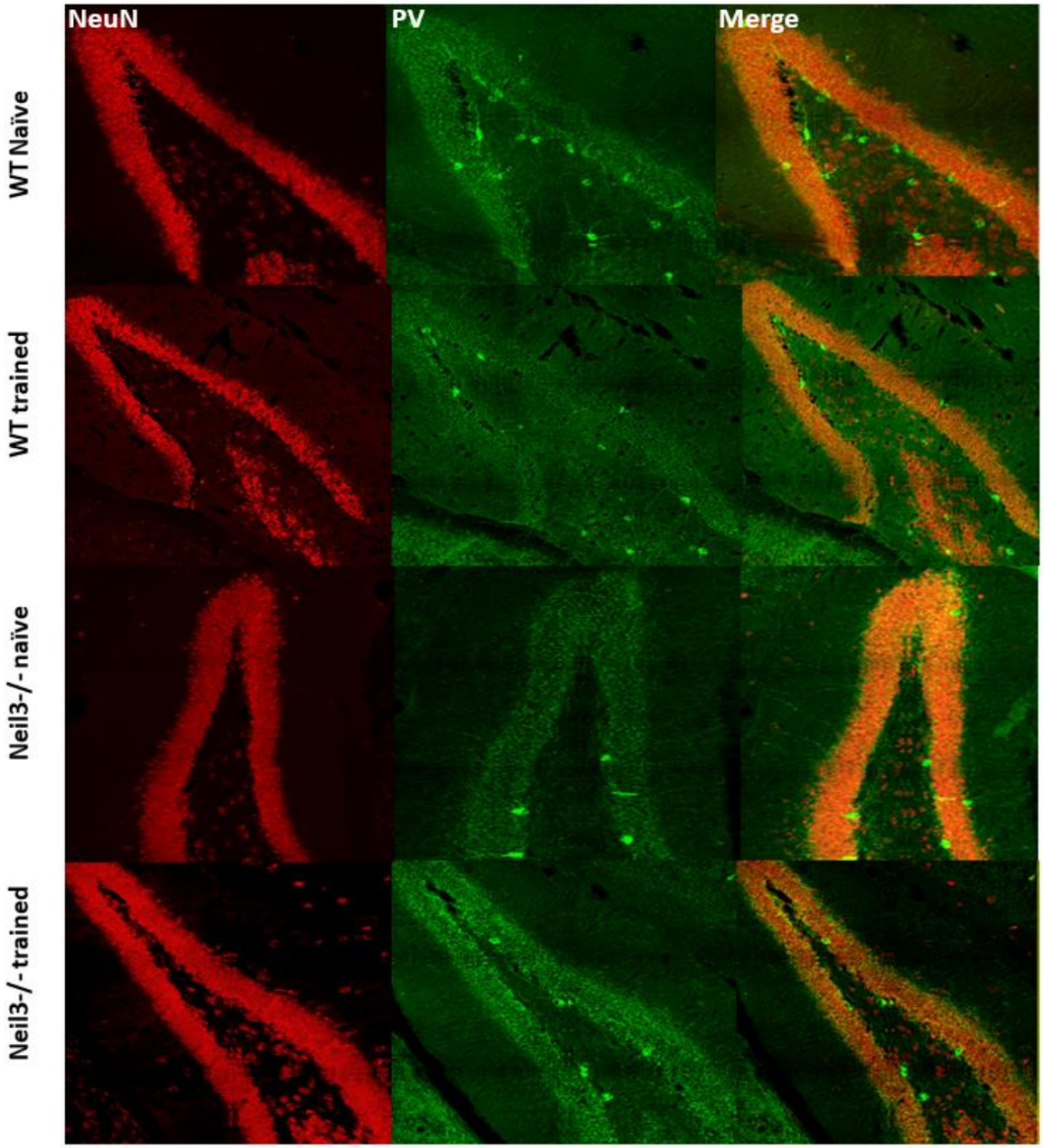

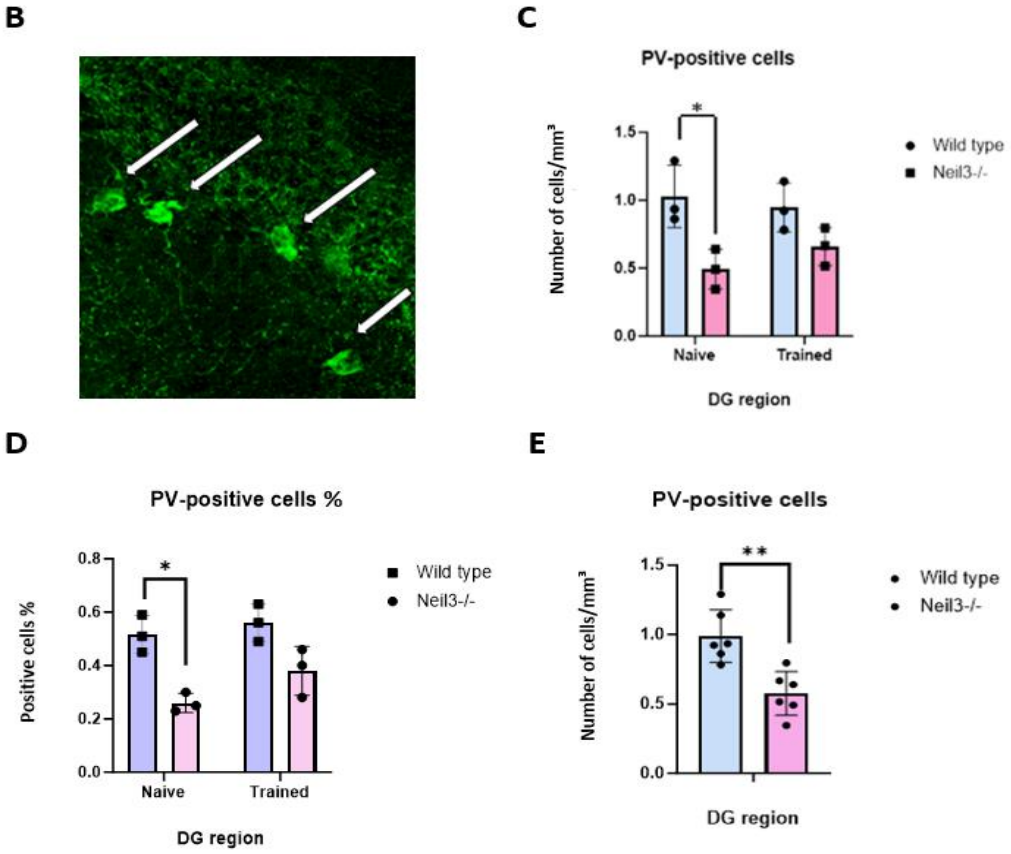

Figure 16: A *Illustrative confocal images of immunostained samples from the dentate gyrus (DG) are displayed, featuring a) naïve and trained wild-type and Neil3-/- mice. Each image is sequentially displayed for NeuN (red), PV (green), and the merged channels. Scanning was conducted using a Zeiss LSM880, employing a Plan-Achromat 40x/NA 1.4 oil immersion objective (Z stack (25), tile (2x3)). Following this, each image was subjected to additional processing using ImageJ (Fiji v1.53) to produce a maximum intensity z-stack projection (n(z stacks) = 20)* ***B)*** *A representative image of PV+ cells counted using Imaris 9.4. The image is acquired following the above description. The scale bar is 10 µm* ***C)****. A representative graph illustrating PV+ cells per volume, counted using Imaris 9.4, is displayed. Statistical analysis was performed using GraphPad Prism 10.1.2 with a two-tailed unpaired t-test; n = 3 mice per time point. The error bars illustrate the standard error of the mean (SEM), and significance was deemed for a p-value below 0.05* ***D).*** *The proportion of PV-positive neurons from total DG neurons is assessed* ***E)*** *A representative graph illustrating PV-positive cells per volume, n = 6 mice per time point.*

4.2.4 Monitoring PV-positive interneurons in CA1

PV-positive cells were identified both in the CA1 pyramidal layer and the stratum orien (Figure 17A). A significant reduced density of PV-positive cells was detected in the CA1 of *Neil3-/-* mice compared to wild-type counterparts (Figure 17C). (n(naïve WT) = 1.52 cells/mm³, n(naïve *Neil3-/-*) = 0.957 cells/mm³; p = 0.0158*; two-tailed unpaired t-test; n = 3 mice per time point. Among the animals exposed to behavioural training, there was an observed decrease in the density of PV-positive cells in *Neil3-/-*; nevertheless, this variation did not attain statistical significance.

In addition, the proportion of PV-positive neurons from total CA1 neurons was assessed. The quantification includes three naïve wild-type and three naïve *Neil3-/-* samples (Figure 17C), providing additional validation for the observed distinctions between the two groups

(n(naïve WT) = 1.44%, n(naïve *Neil3-/-*) = 0.88%; p = 0.0179*; two-tailed unpaired t-test; n = 3 mice per time point.

Confirmation methods for quantification consistently validated the significant distinction between wild type and *Neil3-/-* in both groups. Combining data obtained by quantification of cell count per cubic millimetre from three animals in each group, presented definitive evidence of these distinctions, as depicted in Graph 17D. These findings suggests that the absence of NEIL3 impacts the quantity of PV interneurons in the hippocampal CA1, highlighting a noteworthy reduction in the inhibitory network in knockout mice.

A

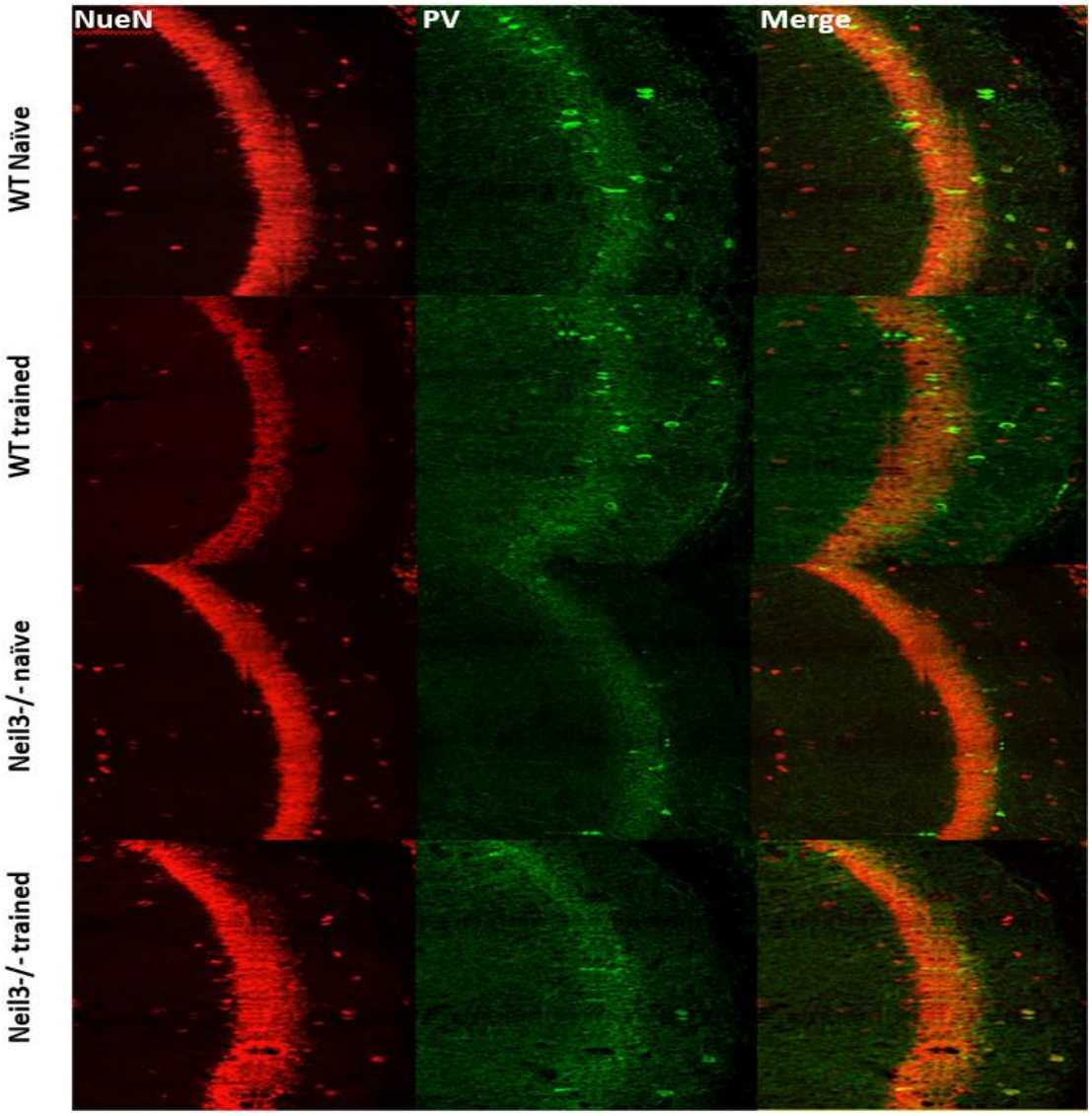

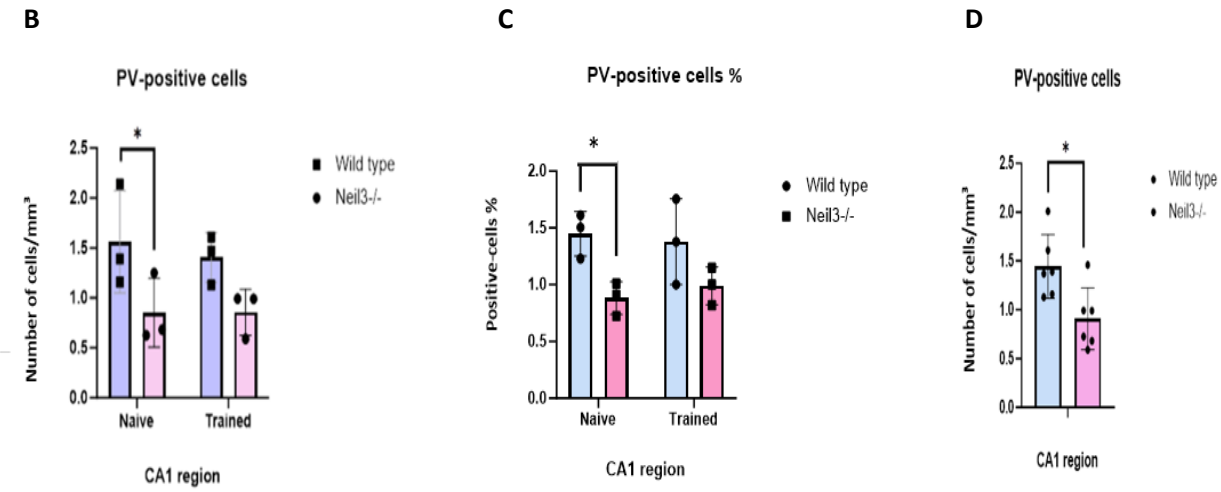

Figure 17: A) *Illustrative confocal images of immunostained samples from the CA1 are displayed, featuring a) naïve and trained wild-type and Neil3-/- mice. Each image is sequentially displayed for NeuN (red), PV (green), and the merged channels. Scanning was conducted using a Zeiss LSM880, employing a Plan-Achromat 40x/NA 1.4 oil immersion objective (Z stack (20), tile (2x3)). Following this, each image was subjected to additional processing using ImageJ (Fiji v1.53) to produce a maximum intensity z-stack projection (n(z stacks) = 15).* ***B)*** *A representative graph illustrating PV+ cells per volume, counted using Imaris 9.4, is displayed. Statistical analysis was performed using GraphPad Prism 10.1.2 with a two-tailed unpaired t-test; n = 3 mice per time point. The error bars illustrate the standard error of the mean (SEM), and significance was deemed for a p-value below 0.05* ***C)*** *The proportion of PV-positive neurons from total CA1 neurons is assessed* ***D)*** *A representative graph illustrating PV+ cells per volume, n = 6 mice per time point.*

4.2.5 Monitoring Somatostatin-positive interneurons in DG

Somatostatin (SST) is an intrinsic peptide synthesized in diverse bodily tissues. In the central nervous system, a subset of GABAergic interneurons releases SST, playing a pivotal role in inhibiting neuronal excitability and regulating network activity. SST further modulates synaptic transmission by decreasing presynaptic glutamate release and exhibits antiepileptic effects by reducing epileptiform bursting and seizure activity [110].

As shown in Figure 18A, Somatostatin-positive neurons were visualized in DG granular zone, hilus and molecular layer by IHC. No decrease in the density of Somatostatin-positive cells was detected in the dentate gyrus (DG) of *Neil3-/-* mice compared to their wild-type counterparts (n(WT) =1.05 cells/mm³, n(*Neil3-/-*) = 1.00 cells/mm³. Similar pattern was observed in the group of animals subjected to behavioural training (n(Trained WT) = 0.962 cells/mm³, n(trained *Neil3-/-*) = 1.18 cells/mm³; n=3 mice per timepoints.

In addition, the proportion of Somatostatin-positive neurons from total DG neurons was assessed. The quantification includes three naïve wild-type and three naïve *Neil3-/-* samples (Figure 18C), providing additional validation for the observed distinctions between the two groups (two-tailed unpaired t-test; n = 3 mice per time point).

Confirmation methods for quantification consistently validated the notable distinction between wild type and *Neil3-/-* in both groups. Combining data illustrating the cell count per cubic millimetre from three animals in each group and six in total presented definitive

evidence of these distinctions, as depicted in graph 18E. This finding indicates that NEIL3 depletion does not influences the number of Somatostatin-positive interneurons in the hippocampal DG. Somatostatin-positive inhibitory neurons might be less susceptible to the specific effects of NEIL3 knockout compared to other neuronal subtypes.

A

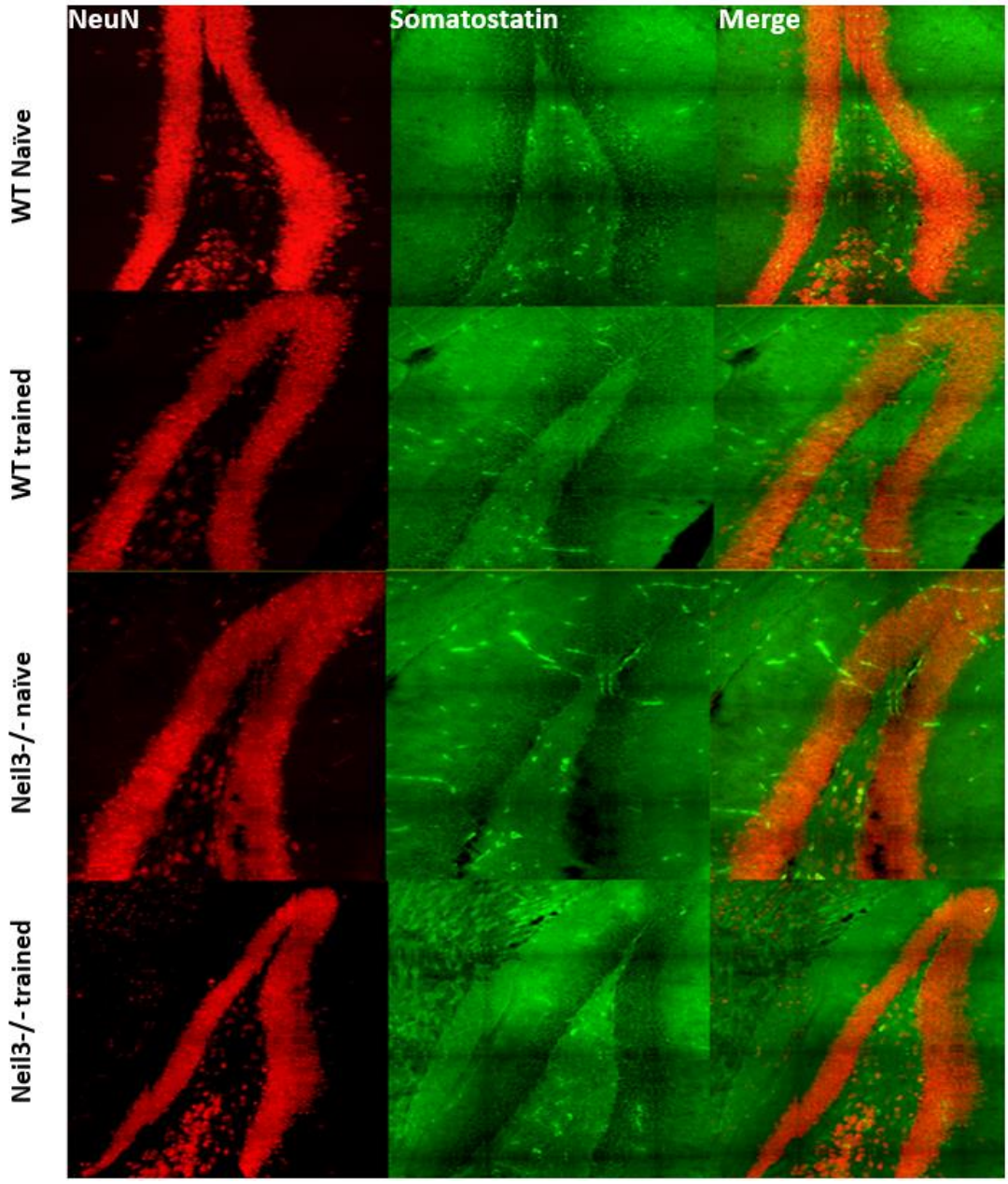

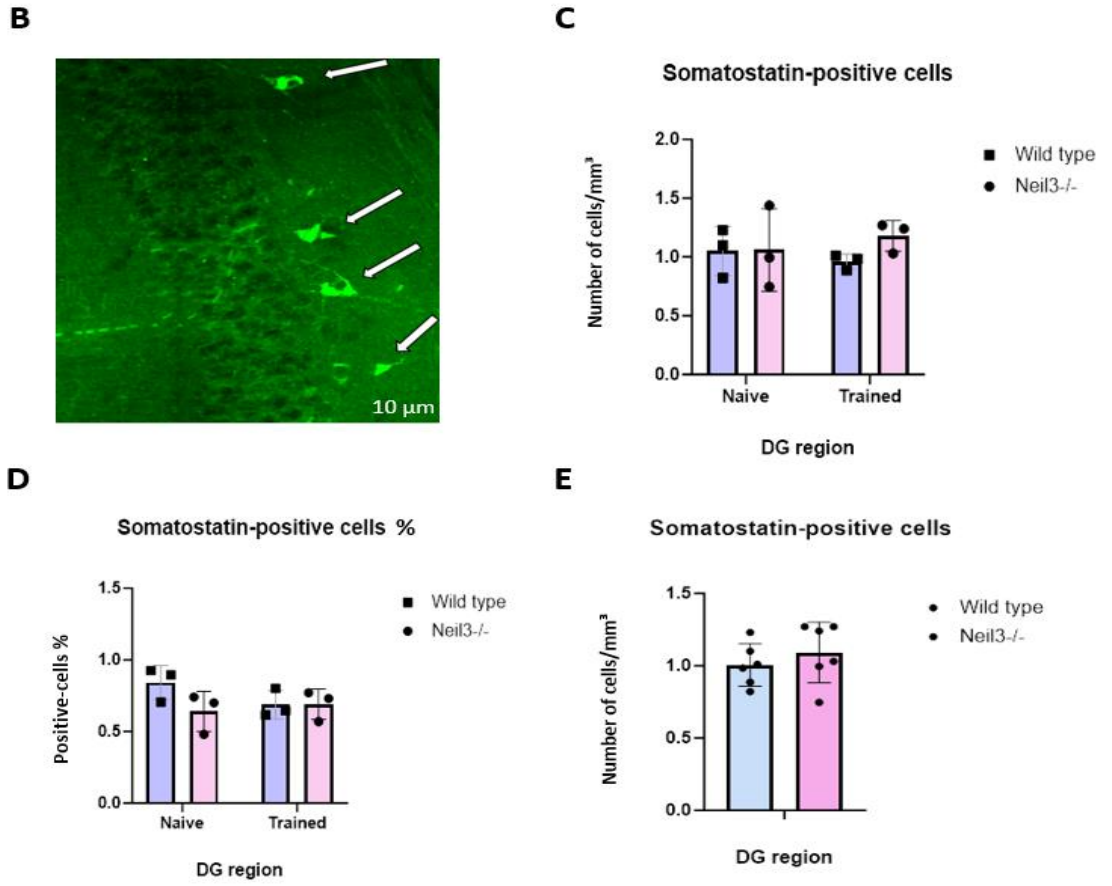

Figure 18: A) *Illustrative confocal images of immunostained samples from the dentate gyrus (DG) are displayed, featuring a) naïve and trained wild-type and Neil3-/- mice. Each image is sequentially displayed for NeuN (red), Somatostatin (green), and the merged channels. Scanning was conducted using a Zeiss LSM880, employing a Plan-Achromat 40x/NA 1.4 oil immersion objective (Z stack (25), tile (2x3)). Following this, each image was subjected to additional processing using ImageJ (Fiji v1.53) to produce a maximum intensity z-stack projection (n(z stacks) = 20)* ***B)*** *A representative image of Somatostatin cells counted using Imaris 9.4. The image is acquired following the above description. The scale bar is 10 µm* ***C)*** *A representative graph illustrating Somatostatin-positive cells per volume, counted using Imaris 9.4, is displayed. Statistical analysis was performed using GraphPad Prism 10.1.2 with a two-tailed unpaired t-test; n = 3 mice per time point. The error bars illustrate the standard error of the mean (SEM), and significance was deemed for a p-value below 0.05* ***D)*** *The proportion of Somatostatin-positive neurons from total DG neurons is assessed* ***E)*** *A representative graph illustrating Somatostatin+ cells per volume, n = 6 mice per time point.*

4.2.6 Monitoring Somatostatin-positive interneurons in CA1

In the hippocampus, where a notable level of Somatostatin binding is observed, oriens-lacunosum moleculare and oriens-bistratified interneurons release Somatostatin. This peptide interacts with Somatostatin receptors situated on the soma and dendrites of CA1 pyramidal neurons, inducing hyperpolarization and diminishing action potential firing in rodent hippocampal pyramidal neurons [110]. As shown in Figure 19A, Somatostatin-positive neurons were visualized in whole CA1 region by IHC. No decrease in the density of Somatostatin-positive cells was detected in the CA1 of *Neil3-/-* mice compared to their wild-type counterparts (n(naïve WT) =2.08 cells/mm³, n(naïve *Neil3-/-* = 1.71 cells/mm³). Similar pattern was observed in the group of animals subjected to behavioural

training (n(Trained WT) = 1.63 cells/mm³, n(trained *Neil3-/-*) = 2.09 cells/mm³, two-tailed unpaired t-test; n = 3 mice per time point.

In addition, the proportion of Somatostatin-positive neurons from total CA1 neurons was assessed. The quantification includes three naïve wild-type and three naïve *Neil3-/-* samples (Figure 19C), providing additional validation for the observed distinctions between the two groups (two-tailed unpaired t-test; n = 3 mice per time point).

Confirmation methods for quantification consistently validated the significant distinction between wild type and *Neil3-/-* in both groups. Combining data obtained by quantification of cell count per cubic millimetre from three animals in each group, presented definitive evidence of these distinctions, as depicted in graph 19D.

This finding indicates that NEIL3 depletion does not influences the number of Somatostatin-positive cells in the hippocampal CA1, demonstrating no influence on the inhibitory network in knockout mice.

A

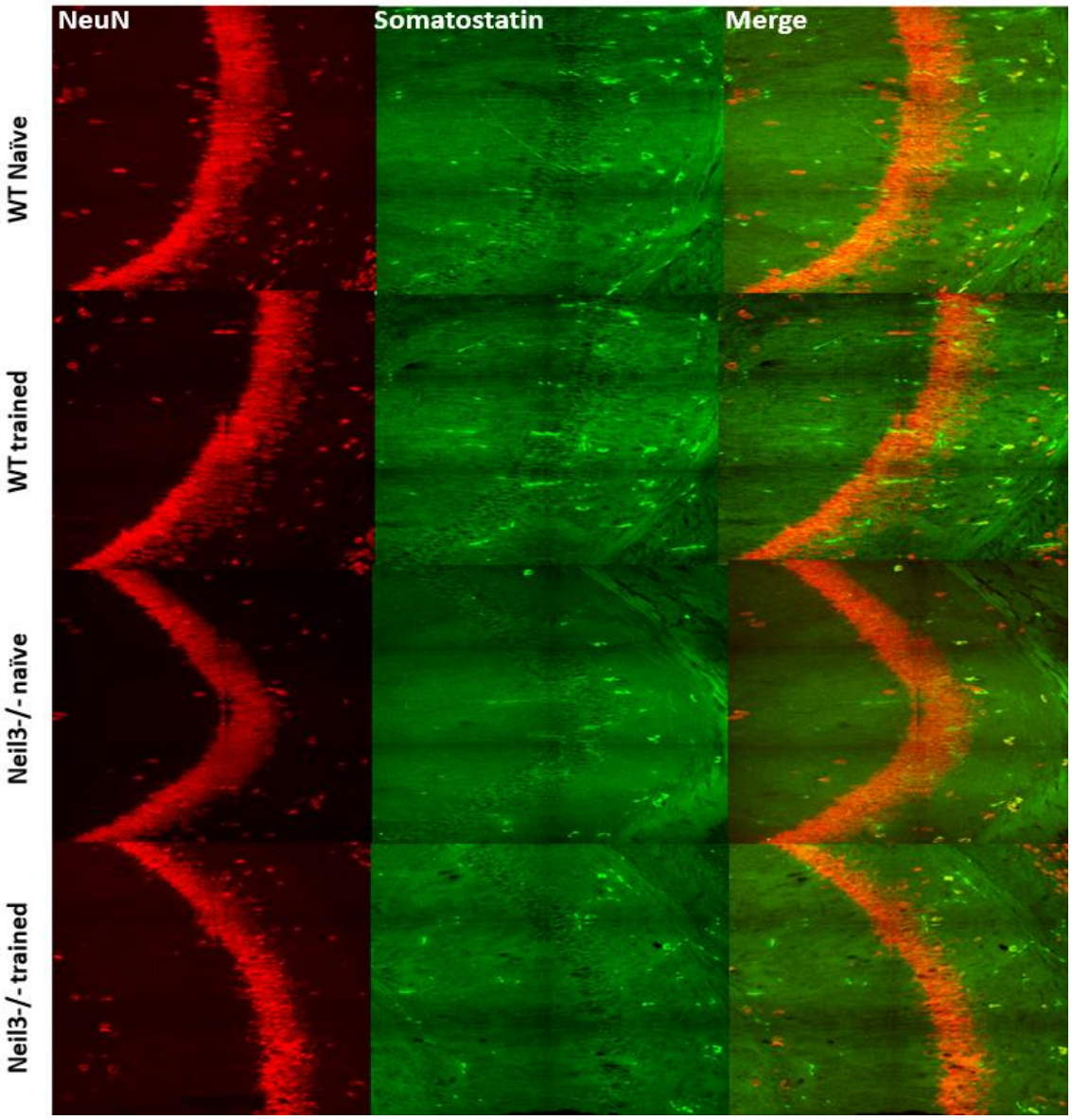

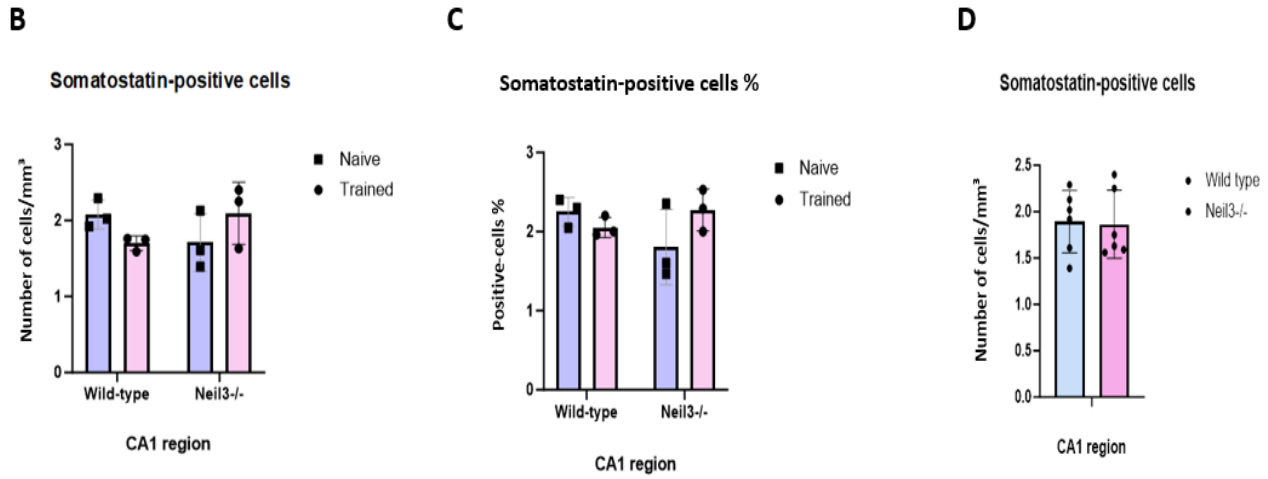

Figure 19 A) *Illustrative confocal images of immunostained samples from the CA1 are displayed, featuring a) naïve and trained wild-type and Neil3-/- mice. Each image is sequentially displayed for NeuN (red), Somatostatin (green), and the merged channels. Scanning was conducted using a Zeiss LSM880, employing a Plan-Achromat 40x/NA 1.4 oil immersion objective (Z stack (20), tile (2x3)). Following this, each image was subjected to additional processing using ImageJ (Fiji v1.53) to produce a maximum intensity z-stack projection (n(z stacks) = 15)* ***B)*** *A representative graph illustrating Somatostatin-positive cells per volume, counted using Imaris 9.4, is displayed. Statistical analysis was performed using GraphPad Prism 10.1.2 with a two-tailed unpaired t-test; n = 3 mice per time point. The error bars illustrate the standard error of the mean (SEM), and significance was deemed for a p-value below 0.05* ***C).*** *The proportion of Somatostatin-positive neurons from total CA1 neurons is assessed* ***D)*** *A representative graph illustrating Somatostatin+ cells per volume, n = 6 mice per time point****.***

4.3. Exploring the role of NEIL3 in the postnatal maturation of hippocampal subregions

The various facets of postnatal development include key processes such as neuronal proliferation, differentiation, and maturation. In this study, our focus is on assessing whether there are any alterations in the proliferation, differentiation, and maturation of neurons within the hippocampus when NEIL3 is depleted during the initial postnatal timepoints.

A breeding strategy was implemented using *Neil3+/-* mice, producing both wild-type (WT) and Neil3 knockout (*Neil3-/-*) mice from the same set of parent mice. This strategy results in the successful generation of WT and *Neil3-/-* mice, all born on the same date, affirming the precision and reliability of the breeding program.

To visualize proliferating cells, neuronal progenitors, mature and immature neurons in the hippocampal subregions DG, CA1 and CA3, I utilized immunohistochemistry. Specifically, antibodies targeting proteins such as Ki67, Sox2, DCX, NeuroD1 and NeuN were applied for this purpose.

To analyse the frozen brain sections of WT and *Neil3-/-* mice, immunohistochemistry (IHC) was conducted using specific antibodies. Confocal fluorescence microscopy (Zeiss LSM880, Z-stack (18), tile (3x4)) captured the entire hippocampus, and 3D-image analysis software Imaris 9.4 quantified the positive cells in the subregions of hippocampus. I quantified the number positive cells in WT and *Neil3-/-* mice at postnatal ages P2 and P8. Statistical analysis employing Two-way ANOVA Tukey's test facilitated pairwise comparisons at each timepoint.

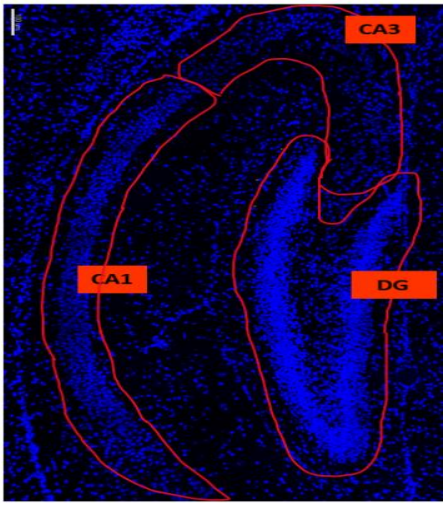

Figure 20: *labelling of distinct regions of the p8 hippocampus, highlighting the selection of specific surface such as DG, CA3, and CA1 for cell counting in Imaris software*.

4.3.1 Quantifying Ki67-Positive Proliferating Cells during postnatal timepoints

Ki67 serves as an effective marker for proliferating cells, being a protein exclusively expressed during cell proliferation [111]. Its expression spans all active phases of tissue-specific cycles, with intensity and cellular location varying across phases [112]. Ki67 expression is minimal in G1 and S phases, peaks during S phase to mitosis, rapidly decreases in anaphase and telophase, making it a valuable marker for proliferating cells [112]. Throughout the cell cycle, Ki67 is found in the nucleus during interphase and on the chromosome surface during mitosis [113]. Previous data in rodents show a decrease of proliferating cell number with age in rodents [50].

The ki67-positive cells are assessed by the number of cells per tissue volume (mm^3) in hippocampal regions. A significant reduced of Ki67-positive neurons was observed in the DG of WT mice from P2 to P8, (n(P2 WT) = 120 cells/mm^3, n(P8 WT) = 85.3 cells/mm^3; p = 0.0005***. Likewise, in *NEIL3-/-* mice Ki67-positive cell number from p2 to p8 showed a similar pattern as WT with a significant decrease in the average density of proliferating cells, n(P2 *Neil3-/-*) = 135 cells/mm^3, n(P8 Neil3-/-) = 86.1 cells/mm^3; p = <0.0001****; two-way ANOVA, Tukey; n = 6 mice per time point. Furthermore, no notable distinctions were observed between genotypes in P2 and P8 mice as shown in figure 21C.

As shown in figure 21 D no decrease in the average density of Ki67-positive neurons was seen in the CA3 region of WT mice from P2 to P8. Likewise, In *NEIL3-/-* mice Ki67-positive cell number from p2 to p8 showed a similar pattern as WT with no difference in the average density of proliferating cells. Furthermore, a statistical significance was observed between genotypes in P2 mice p = 0.024**, as well as in P8 mice p= 0.0006***.

A significant decrease in the average density of Ki67-positive neurons was seen in the CA1 region of WT mice from P2 to P8, n(P2 WT) = 15.55 cells/mm3, n(P8 WT) = 7.44 cells/mm3; p = 0.095**. Whereas, in *Neil3-/-* mice, the average density of Ki67-posiitve cell from p2 to p8 showed no difference . Furthermore, notable distinctions were observed between genotypes, in P8 mice p = 0.0025**, whereas in P2 mice this difference was not significant.

In conclusion, the decrease of the average density of Ki67-positive cells between p2 and p8 was the most pronounced. Between the two groups there were more Ki67-positive cells detected in *Neil3-/-* mice as compared to wild types, the two-way ANOVA, Tukey show statistically significant differences in both time points, which indicate that the NEIL3 have impact on the number of proliferating cells. Our observations are consistent with published results showing that the number of proliferating cells decreases with age in rodents [114].

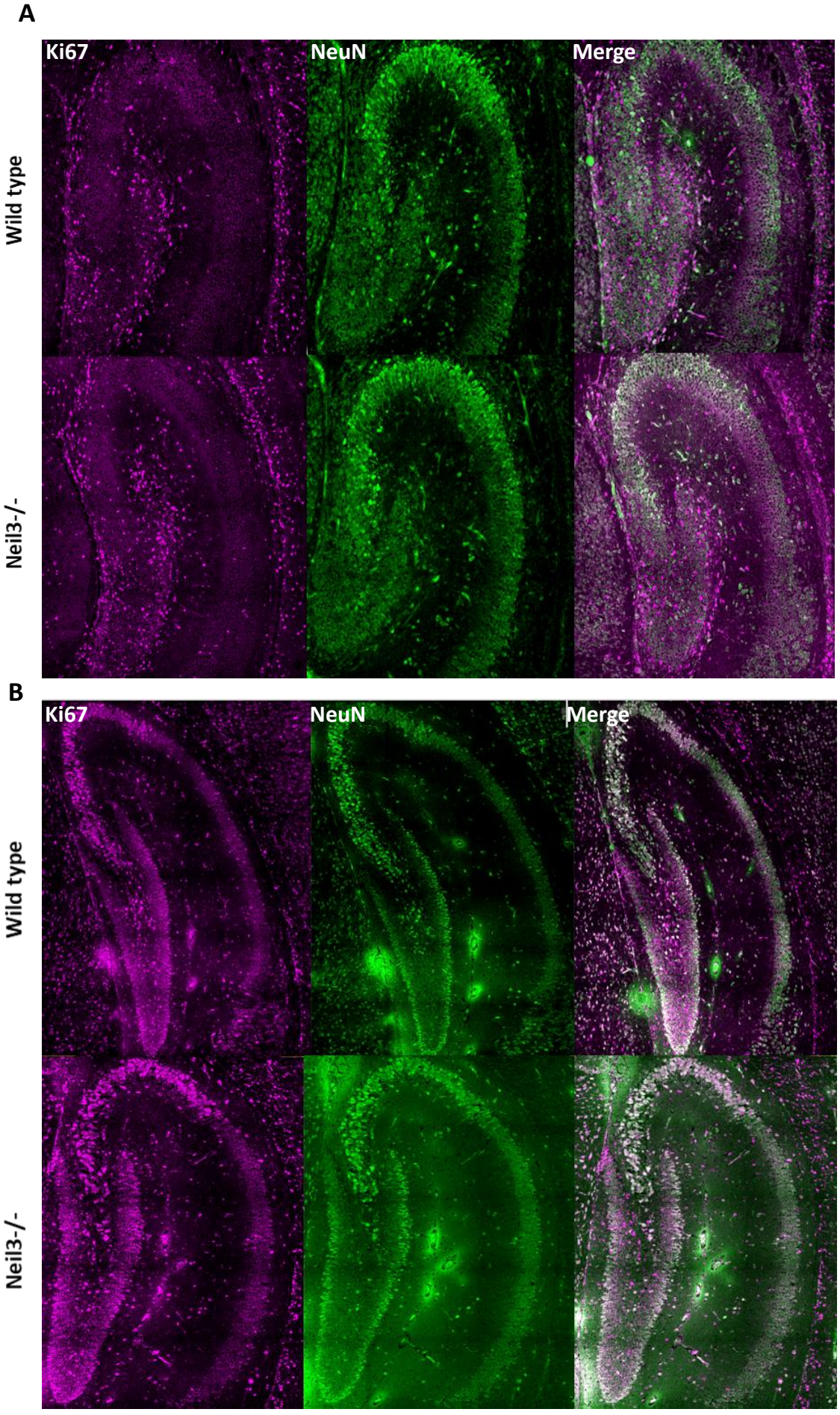
A
Ki67
NeuN
Merge
Wild type
Neil3-/-
B
Ki67
NeuN
Merge
Wild type
Neil3-/-

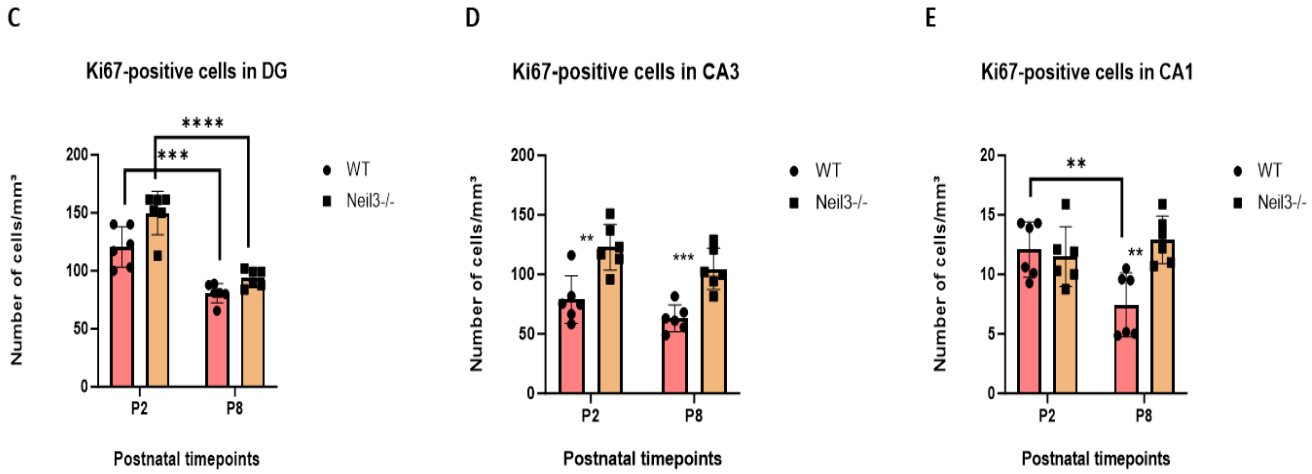

Figure 21: A,B) *Representative confocal images of immunostained hippocampus samples are presented, featuring Wild Type and Neil3-/- on postnatal day 2 and 8. Each image is sequentially displayed for Ki67 (magenta), NeuN (green), and the merged channels. Scanning was conducted using a Zeiss LSM880, employing a Plan-Achromat 40x/NA 1.4 oil immersion objective (Z stack (18), tile (3x5)). Following this, each image was subjected to additional processing using ImageJ (Fiji v1.53) to produce a maximum intensity z-stack projection (n(z stacks) = 15). The scale bar represents 100 µm.* ***C), D), E)*** *Comparative analysis of the number of Ki67-positive cells/mm³in the DG, CA3 and CA1 region was conducted separately for both WT and Neil3-/- on postnatal day 2 and 8. Statistical analysis was performed using GraphPad Prism 10.1.2 with a two-way ANOVA (Tukey). The error bars illustrate the standard error of the mean (SEM), and significance was deemed for a p-value below 0.05.*

3.3.2 Quantifying expression levels of Sox2 neurons during the postnatal timepoints.

Sox2, a protein expressed in neural stem and progenitor cells in the mouse neocortex, served as the marker for monitoring neural progenitor cells [115, 116]. Sox2 is known to be expressed in adult neuronal stem cells during development [117, 118], which is why we chose this marker for visualization of neuronal progenitor cells.

Sox2 was massively expressed in hippocampus during the early postnatal days, therefore a new method of measuring the Voxel numbers per cubic millimetre was established, which shows the level of Sox2 expression in hippocampus. The decrease in the Sox2 expression level between p2 and p8 was most obvious in DG wildtype, n(P2 WT) = 3082 voxels/mm³, n(P8 WT) = 1999 voxels/mm³; p = 0.007**. While in NEIL3-deficient mice, expression level did not elicit a significant change from age p2 to p8, two-way ANOVA (Tukey); n = 6 mice per time point. However, no significant difference was observed in the expression level between the genotypes of age p2 and P8 as shown in Figure 22C.

The expression level of Sox2 neural progenitor was quantified in CA3 region. The decrease of the Sox2 expression level between p2 and p8 was most obvious, with the Sox2 expression in wildtype n(P2 WT) = 2171 voxels/mm³, n(P8 WT) = 1186.6 voxels/mm³; p = 0.0004***. Likewise, in NEIL3-deficient mice, the expression levels elicit a significant distinction from p2 to p8, n(P2 *Neil3-/-*) = 2289 voxels/mm³, n(P8 *Neil3-/-*) = 1107 voxels/mm³; p = 0.0010**. However, no significant difference was observed in the expression level of Sox2 between the two genotypes of age p2 and P8.

The expression level of Sox2-positive neural progenitor was quantified in CA1 region. The decrease of the Sox2 expression level between p2 and p8 was most obvious, with the expression level of Sox2-positive cells in wildtype n(P2 WT) = 2600 voxels/mm³, n(P8 WT) = 1255 voxels/mm³; p = 0.0006***. Likewise, in NEIL3-deficient mice, Sox2 expression level elicit a significant distinction from p2 to p8, n(P2 *Neil3-/-*) = 3353 voxels/mm³, n(P8 *Neil3-/-*) = 1157 voxels/mm³; p = 0.0016**. However, no significant difference was observed in expression level of Sox2-positive cells between the two genotypes of age p2 and P8.

In conclusion, our statistical analysis indicates a similar expression levels of neuronal progenitor cells in WT and *Neil3-/-* mice in the early postnatal timepoints which indicate that the expression level of Sox2 is not influenced by NEIL3. However, a decline in the average density from P2 to P8 suggest reduced expression with age. Similar to the pattern observed for Ki67-positive cells, the expression level of Sox2 was elevated at P2 and significantly declined in later postnatal timepoint p8 in both wildtype and *Neil3-/-* hippocampus.

A

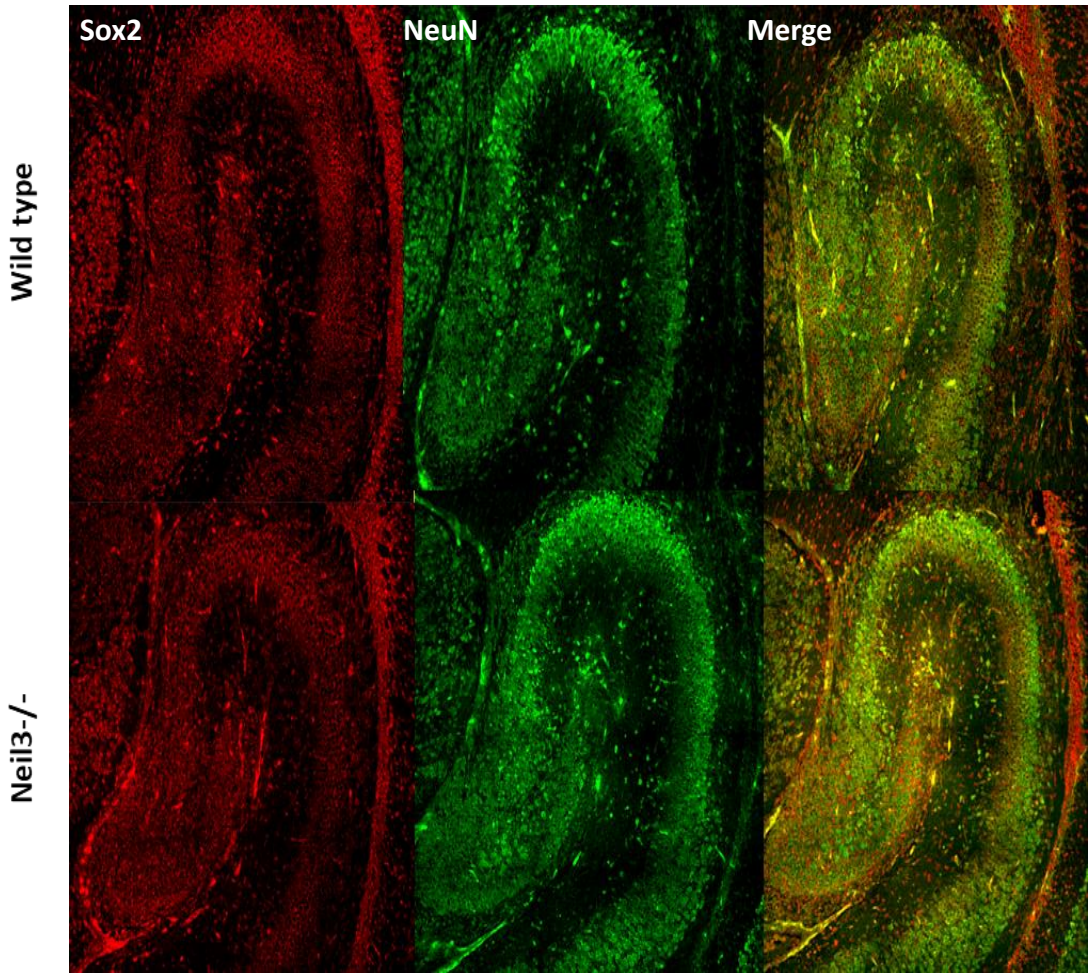

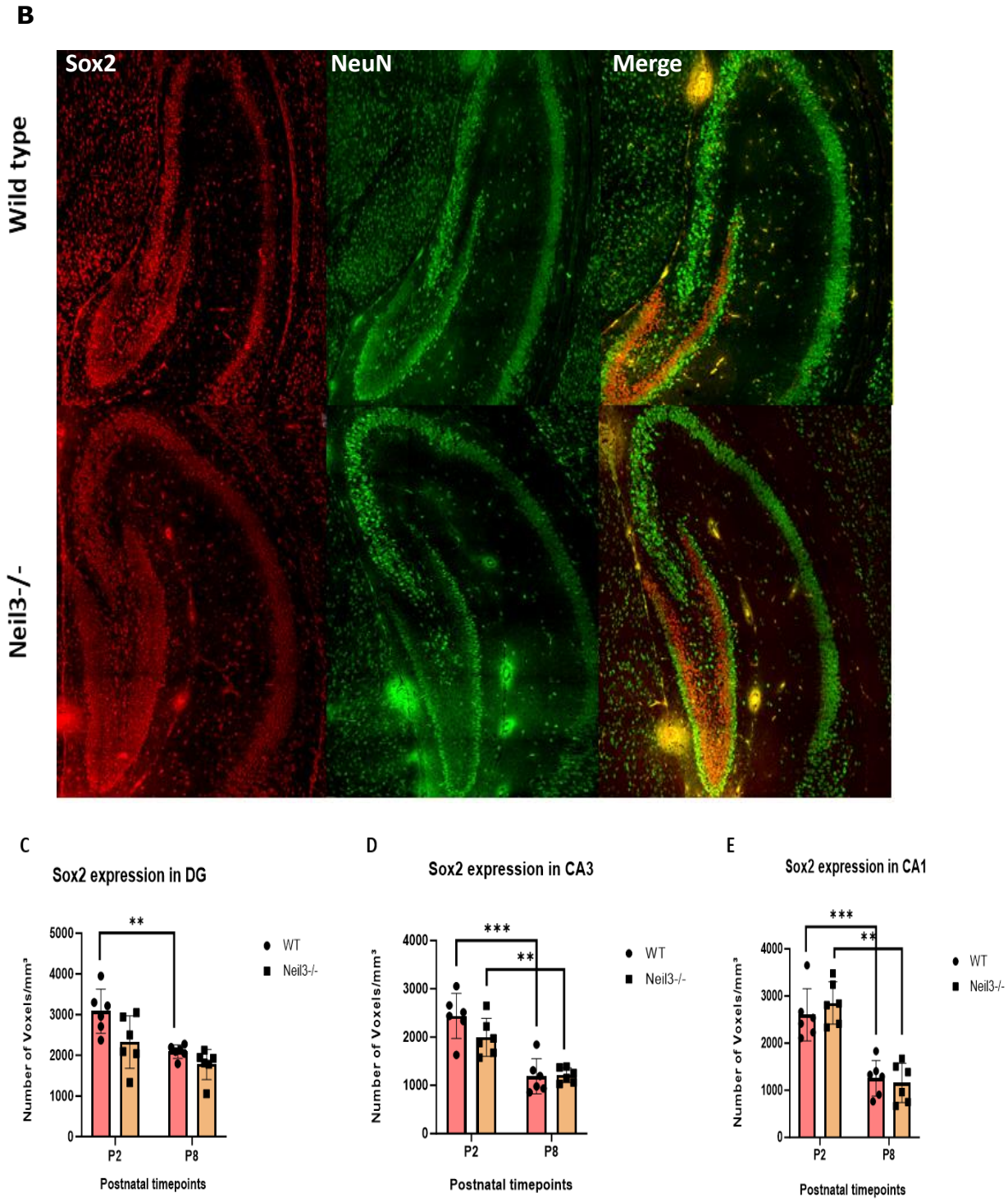

Figure 22: A), B) *Representative confocal images of immunostained hippocampus samples are presented, featuring Wild Type and Neil3-/- on postnatal day 2 and 8. Each image is sequentially displayed for Sox2 (red), NeuN (green), and the merged channels. Scanning was conducted using a Zeiss LSM880, employing a Plan-Achromat 40x/NA 1.4 oil immersion objective (Z stack (18), tile (3x5)). Following this, each image was subjected to additional processing using ImageJ (Fiji v1.53) to produce a maximum intensity z-stack projection (n(z stacks) = 15). The scale bar represents 100 µm.* ***C), D), E)*** *Comparative analysis of the voxel number of Sox2-positive cells/mm³ in the DG, CA3 and CA1 region was conducted separately for both WT and Neil3-/- on postnatal day 2 and 8. Statistical analysis was performed using GraphPad Prism 10.1.2 with a two-way ANOVA (Tukey). The error bars illustrate the standard error of the mean (SEM), and significance was deemed for a p-value below 0.05.*

4.3.3 Quantifying DCX expression level in immature neurons during postnatal timepoints.

We evaluated neuronal maturation in the dentate gyrus (DG) by utilizing doublecortin (DCX) as an indicator of immature neurons. DCX, a protein expressed during the transition from the progenitor stage to the calretinin-positive stage, plays a vital role in dendritic and axonal growth, facilitating the establishment of functional connections [119]. This protein is exclusively present in immature neurons within regions exhibiting neurogenesis in adult animals [120, 121]. The protein's localization changes during neuronal migration and differentiation, being observed in the soma and leading processes during migration and in the axons during differentiation [121].

The expression level of DCX in immature neurons at postnatal ages P2 and P8 were quantified. There was no notable change in the level of gene expression from p2 to p8 in DG as well as in between the two genotypes of age P2 and P8, two-way ANOVA (Tukey), suggesting that the NEIL3 has no effect on the expression level of DCX in DG immature neurons in both postnatal timepoints as shown in Figure 23C.

The expression level of DCX was quantified in CA3 region. The decrease of the DCX expression level in wild type between p2 and p8 was not significant. Whereas, in NEIL3-deficient mice, the expression levels elicit a significant decrease from p2 to p8, n(P2 *Neil3-/-*) = 2558 voxels/mm³, n(P8 Neil3-/-) = 1198 voxels/mm³; 0.0160*. However, no significant difference was observed in the expression level of DCX between the two genotypes of age p2 and P8 as shown in Figure 23D.

The expression level of DCX was quantified in CA1 region. The decrease of the DCX expression level between p2 and p8 was most obvious, with the expression level of DCX in wildtype n(P2 WT) = 2660 voxels/mm3, n(P8 WT) = 1547 voxels/mm³; p = 0.006**. Likewise, in NEIL3-deficient mice, DCX expression level elicit a significant distinction from p2 to p8, n(P2 *Neil3-/-)* = 3670 voxels/mm³, n(P8 *Neil3-/-*) = 630 voxels/mm3; p= 0.0005***. However, no significant difference was observed in expression level of DCX between the two genotypes of age p2 and p8.

In conclusion, our statistical analysis indicates a decrease in expression levels of DCX in WT and *NEIL3-/-* mice in the postnatal age P8. However, no difference was observed between the genotypes of P2 and P8 in any timepoints, indicating that NEIL3 has no impact on the expression level of DCX. A decline in DCX expression by postnatal day 8 was observed more prominent in CA3 and CA1 region as compared to DG. A contributing factor could be the migration of neurons from the dentate gyrus DG to CA3, then to CA1, and finally to other regions like the subiculum and entorhinal cortex, forming the intricate connections of the hippocampal circuit.

A

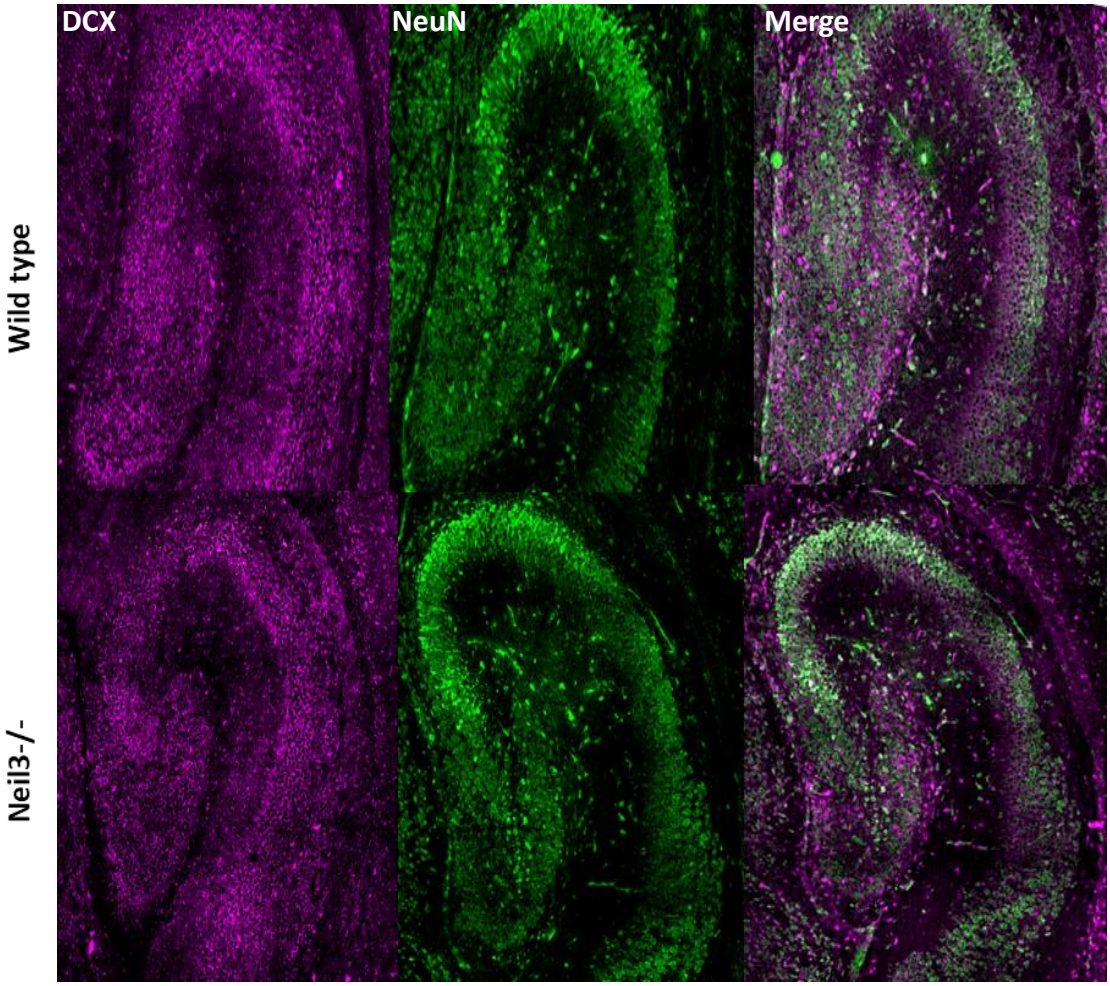

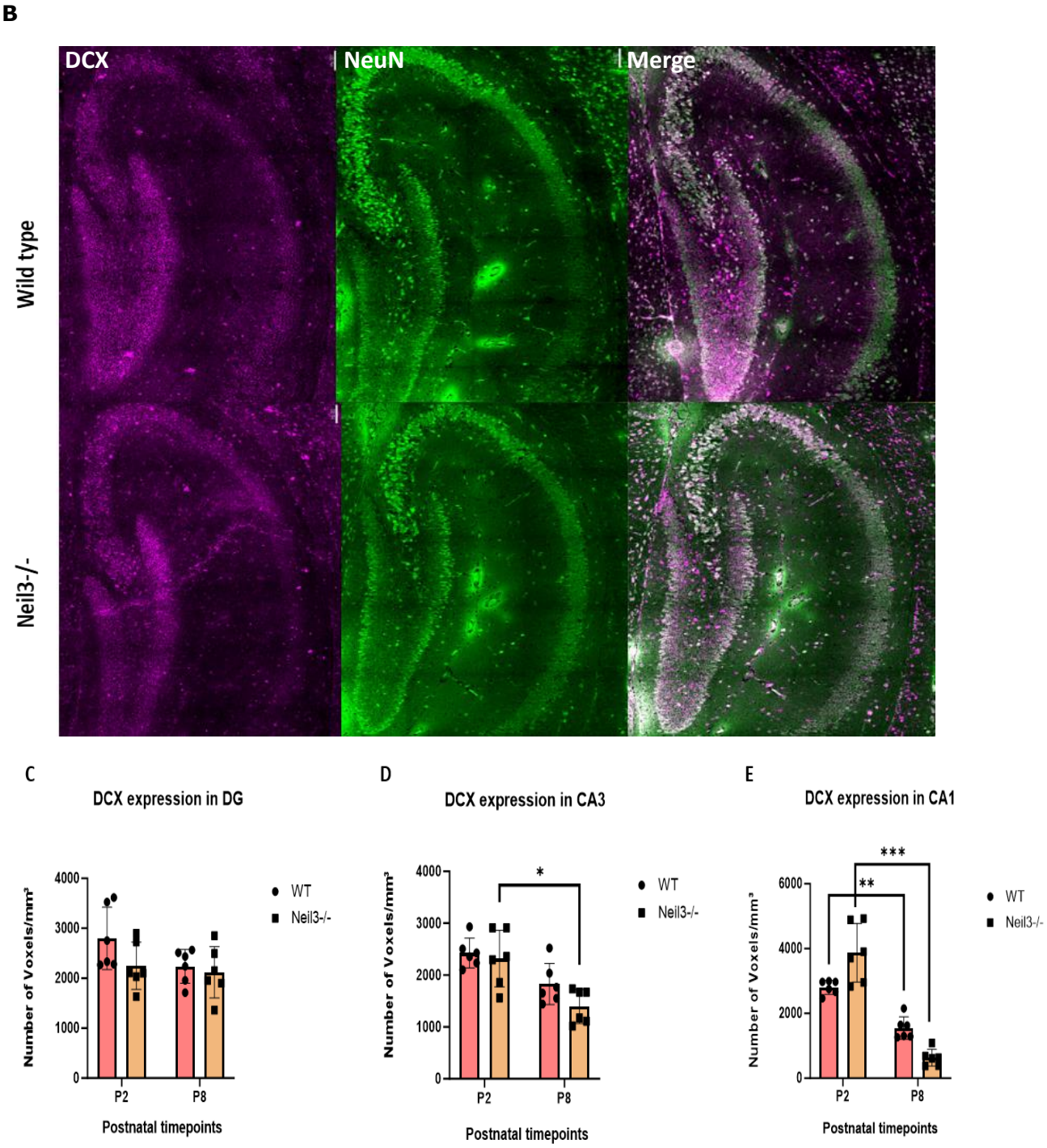

Figure 23: A), B) *Representative confocal images of immunostained hippocampus samples are presented, featuring Wild Type and Neil3-/- on postnatal day 2 and 8. Each image is sequentially displayed for DCX (magenta), NeuN (green), and the merged channels. Scanning was conducted using a Zeiss LSM880, employing a Plan-Achromat 40x/NA 1.4 oil immersion objective (Z stack (18), tile (3x5)). Following this, each image was subjected to additional processing using ImageJ (Fiji v1.53) to produce a maximum intensity z-stack projection n(z stacks) = 15)* ***C), D), E)*** *Comparative analysis of the voxel number of DCX-positive cells/mm³in the DG, CA3 and CA1 region was conducted separately for both WT and Neil3-/- on postnatal day 2 and 8. Statistical analysis was performed using GraphPad Prism 10.1.2 with a two-way ANOVA (Tukey). The error bars illustrate the standard error of the mean (SEM), and significance was deemed for a p-value below 0.05.*

4.3.4 Quantifying NeuroD1-positive neurons during the postnatal timepoints.

A singular transcription factor, NeuroD1, exhibits the ability to directly transform mouse microglia into neurons. The resulting NeuroD1-converted neurons demonstrate the expression of mature neuronal markers and establish synaptic networks with primary cultured cortical neurons. Notably, NeuroD1 is predominantly active in the nervous system during the early stages of development, suggesting its involvement in terminal differentiation, neuronal maturation, and survival [122]. Furthermore, I observed abundant expression of NeuroD1 in neurons within specific brain structures such as the hippocampus. The study sheds light on the multifaceted functions of NeuroD1, emphasizing its significance in the intricate processes of neurogenesis and neuronal maturation within the hippocampus [123].

The decrease of the average density of NeuroD1-positive cells between p2 and p8 was most obvious, with the number of NeuroD1-positive cells wildtype n(P2 WT) = 182.1 cells/mm³, n(P8 WT) = 148.5 cells/mm³; p = 0.0028**. These cells were high at P2 and decreased dramatically during the postnatal day 8. Likewise, in NEIL3-deficient mice, number of NeuroD1-positive cells also shows significant decrease from p2 to p8, n(P2 *Neil3-/-*) = 193 cells/mm³, n(P8 *Neil3-/-*) = 96.3 cells/mm³; p = 0.0098***; two-way ANOVA, Tukey; n(P2 *Neil3-/-*) = 6, n(P8 *Neil3-/-*) = 6. However, no significant difference was observed in the number of NeuroD1-positive cells between the two genotypes of age p2 and p8, indicating that *Neil3-/-* have no influence on NeuroD1-positive cells in hippocampus.

As neurons mature, the necessity for NeuroD1 may diminish or become more finely regulated, resulting in a potential decrease in NeuroD1 expression by P8. Neurons differentiate into mature, functional cells over time. The time elapsed between P2 and P8 may be critical for the maturation and differentiation of neurons into a state where they express NeuroD1 more prominently. The NeuroD1 was observed to be expressed in DG but not in other regions of hippocampus. Its expression is closely linked to the neurogenic processes, and the dentate gyrus is a major site of neurogenesis in the hippocampus.

A

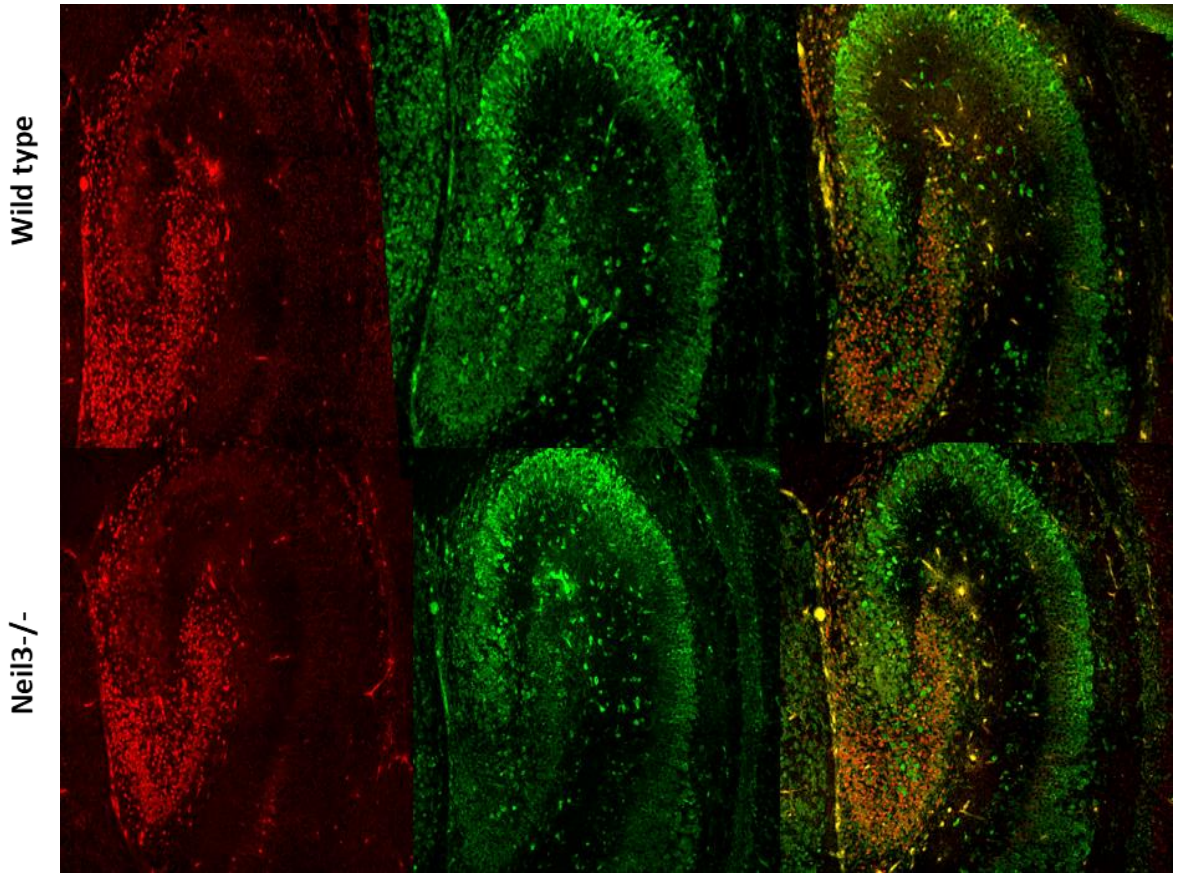

B

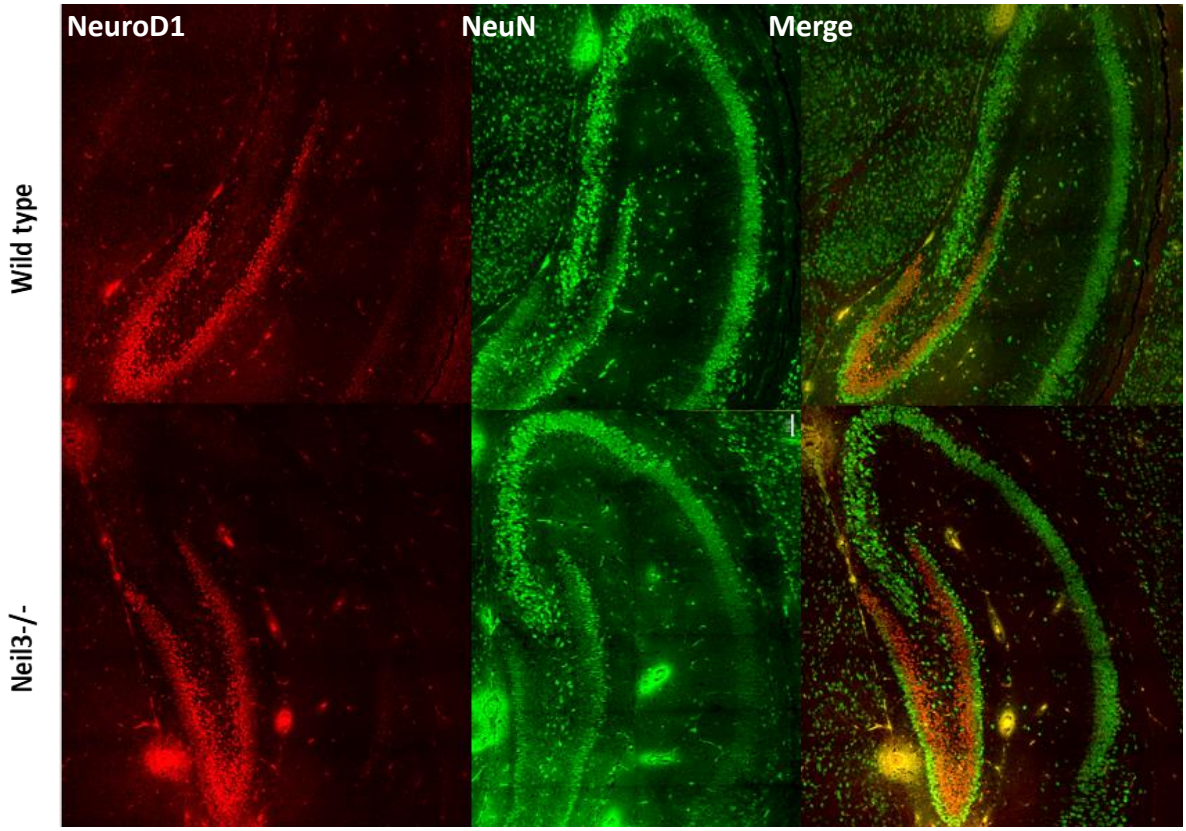

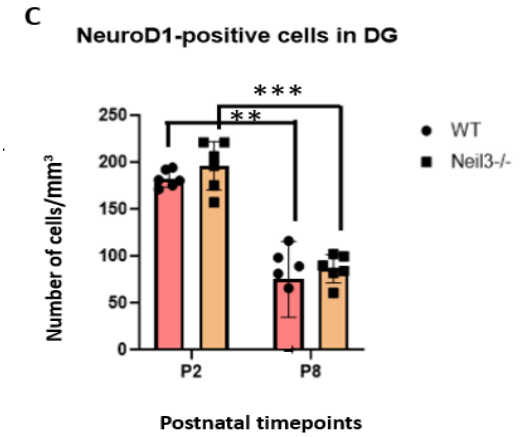

Figure 24: A), B) *Representative confocal images of immunostained hippocampus samples are presented, featuring Wild Type and Neil3-/- on postnatal day 2 and 8. Each image is sequentially displayed for NeuroD1 (red), NeuN (green), and the merged channels. Scanning was conducted using a Zeiss LSM880, employing a Plan-Achromat 40x/NA 1.4 oil immersion objective (Z stack (18), tile (3x5)). Following this, each image was subjected to additional processing using ImageJ (Fiji v1.53) to produce a maximum intensity z-stack projection (n(z stacks) = 15). The scale bar represents 100 µm.* ***C)*** *Comparative analysis of the number of NeuroD1-positive cells/mm³ in the DG region was conducted separately for both WT and Neil3-/- on postnatal day 2 and 8. Statistical analysis was performed using GraphPad Prism 10.1.2 with a two-way ANOVA (Tukey). The error bars illustrate the standard error of the mean (SEM), and significance was deemed for a p-value below 0.05.*

4.3.5 Quantifying Neun-positive mature neurons during the postnatal timepoints.

NeuN is a protein expressed in most mature neurons in the central nervous system, specifically post-mitotic neurons in the hippocampus [124-126]. It is absent in non-neuronal cells in the central neural system, making it a specific neuronal marker [124]. As DCX expression decreases during postnatal development, NeuN expression increases, making the combination of both markers suitable for assessing neuronal maturation in the dentate gyrus (DG) [124].

I sought to investigate the significance of NEIL3 in the postnatal maturation of hippocampal neurons from day 2 to day 8. I methodically monitored the maturation process of neurons in the hippocampus using immunohistochemistry (IHC) with the neuronal marker NeuN. The immunoreactivity of NeuN functions as an indicator, exhibiting robustness in mature hippocampal neurons and comparatively weaker expression in their immature counterparts. NeuN is predominantly expressed in the nuclei and perinuclear cytoplasm [124]. The staining intensity of NeuN, correlates with neuronal maturation [124, 127]. This allowed us to distinguish between two cell populations: one weakly stained population of immature neurons and one strongly stained population of mature neurons.

As shown in figure 25 A, a significant increase in the average density of NeuN-positive cells was seen in the DG of WT mice from P2 to P8, n(P2 WT) = 125 cells/mm³, n(P8 WT) = 160 cells/mm³; p = 0.0242*. Whereas, In *Neil3-/-* mice NeuN-positive cell number from p2 to p8 showed a distinct pattern with a significant decrease in the average density of mature neurons, n(P2 *Neil3-/-*) = 146 cells/mm³, n(P8 *Neil3-/-*) = 83.5 cells/mm3; p = 0.0387* two-way ANOVA, Tukey; n = 6 mice per time point. Furthermore, no notable distinctions were observed between genotypes, in p2 mice whereas in p8 mice this

difference was most significant P8=0.0006*** suggesting a delayed DG maturation in *Neil3-/-* mice.

A significant increase in the average density of NeuN-positive cells was observed in the CA3 region of WT mice from P2 to P8, n(P2 WT) = 2.08 cells/mm³, n(P8 WT) = 1.63 cells/mm³; p = <0.0001****, similar pattern was observed in *Neil3-/-* mice, n(P2 *Neil3-/-*) = 2.08 cells/mm³, n(P8 *Neil3-/-*) = 1.63 cells/mm³; p = 0.00387** two-way ANOVA, Tukey; n = 6 mice per time point. Furthermore, no statistical difference was observed between genotypes in P2 as well as in P8 mice. The high number of mature neurons in p8 suggest that the time elapsed between P2 and P8 may be critical for the maturation and differentiation of neurons.

A significant increase in the average density of NeuN-positive cells was observes in the CA1 region of WT mice from P2 to P8, n(P2 WT) = 2.08 cells/mm³, n(P8 WT) = 1.63 cells/mm³; p = <0.0001****. Whereas this difference was not observed in *Neil3-/-.* Furthermore, no statistical significance was observed between genotypes in P2 mice whereas in P8 mice a significant distinction was observed between the genotypes p= <0.0001**** suggesting a delayed CA1 maturation in *Neil3-/-* mice.

Upon comparing *Neil3-/-* and wildtype mice at various time points, a consistent finding emerged: the average fraction of strongly expressing NeuN-Positive cells were notably lower in *Neil3-/-* mice. This observed difference in mature neurons aligns with our initial hypothesis that NEIL3 has a discernible impact on the maturation of neurons in mice. In summary, these results collectively suggest that the absence of NEIL3 results in a delayed maturation process in the hippocampal subregions, highlighting the involvement of NEIL3 in neuronal maturation. Another reason is that neurons differentiate into mature, functional cells over time. The time elapsed between P2 and P8 may be critical for the maturation and differentiation of neurons into a state where they express Neun more prominently.

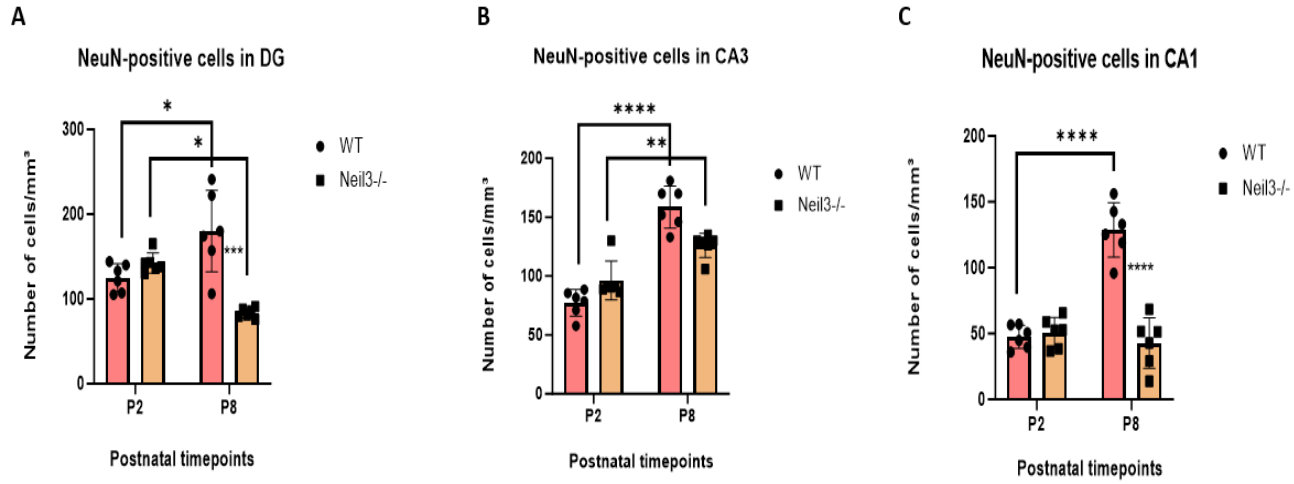

Figure 25: A) B), C), *Comparative analysis of the number of NeuN-positive cells/mm3 in the DG, CA3 and CA1 region was conducted separately for both WT and Neil3-/- on postnatal day 2 and 8. Statistical analysis was performed using GraphPad Prism 10.1.2 with a two-way ANOVA (Tukey). The error bars illustrate the standard error of the mean (SEM), and significance was deemed for a p-value below 0.05.*

5. Discussion

5.1 Main Findings

Emerging evidence suggests novel functions of NEIL3 in the brain. *Neil3-/-* mice, following a stroke, exhibit impaired neurogenesis [128]. The DNA repair enzyme NEIL3 plays a crucial role in influencing the maturation and function of hippocampal neurons by shaping the transcriptome during development. Our observations indicate a delayed maturation in mice lacking Neil3. In vitro studies using cells from aged *Neil3-/-* mice demonstrate diminished neurogenesis in the hippocampus compared to *Neil3+/+* mice [33]. Behavioral assessments reveal spatial learning and memory deficits in *NeilL3-/-* mice during the Morris maze water test, as well as reduced anxiety in the zero-maze test when compared to wildtype mice [33]. These findings imply that NEIL3 play a significant role in neurogenesis and hippocampal-dependent functions, such as memory, and cognitive processing. Hence *Neil3-/-* have important role for both development and function of hippocampus.

The focus of this project is to: (1) investigate the impact of NEIL3 on gene expression in hippocampal subregions, utilizing various primers and analyzing differentially expressed genes through quantitative polymerase chain reaction (QPCR). (2) Explore the NEIL3's influence on the organization of GABAergic inhibitory neurons, comparing naïve and trained WT with *Neil3-/-* mice, focusing on the dentate gyrus (DG) and cornu ammonis 1 (CA1) in 3-month-old mice. (3) Examine the NEIL3's role in the postnatal maturation of hippocampal subregions, analyzing the maturation and organization of distinct neuronal populations during postnatal days 2 (p2) and 8 (p8). Specifically, the investigation centers on distinct neuronal populations within the dentate gyrus (DG) and Cornu Ammonis (CA1 and CA3) regions of the hippocampus (HPC).

The main findings of the project are: (1) the normalized gene expression identified in both the hippocampal CA1 and DG regions via qPCR revealed distinct expression patterns of these genes in WT and *Neil3-/-* (2) The absence of NEIL3 significantly influences the organization of GABAergic inhibitory neurons within the hippocampus, elucidating a marked reduction in the inhibitory network observed in knockout mice, highlighting the functional role of NEIL3 in the hippocampus. (3) A decrease in proliferating neurons and neural progenitor cells, reduced DCX expression, increase in mature neurons like NeuN and NeuroD1 were noted in the hippocampus of P8 mice compared to P2 mice were observed. Furthermore, the alterations in the numbers of these neurons in *Neil3-/-*, emphasize the role of NEIL3 in the postnatal maturation of hippocampus. In conclusion, my findings suggest a significant role of the DNA repair enzyme NEIL3 in both the development and function of the hippocampus.

5.2 Methodological considerations:

Some methodological considerations and limitations were encountered in this study. The cell-counting method in Imaris, particularly for somatostatin samples, presented challenges with a high background signal and difficulty in distinguishing desired cells from artifacts. Moreover, the staining of DCX posed challenges as well, as it was massively expressed in hippocampus during the early postnatal days, therefore a new method of measuring the Voxel numbers per cubic millimetre was established making individual cell counting and the spot tool impractical.

Perfusion qualities and exposure times in fixative agents varied, potentially impacting staining quality and antibody binding. Background staining, resulting from unspecific antibody binding, further impacted manual counting accuracy.

Given the substantial differences in gene expression across HPC subregions, precision in isolation methods is crucial to minimize potential contamination. While traditional microdissection under a microscope has been widely used, it can lead to lower specificity due to imprecise cutting. Laser microdissection is therefore preferred, enabling more precise isolation of different subregions.

5.3 NEIL3 impacts specific gene expression in the hippocampal subregions

Different cell types in the brain maintain their unique chromosomal compositions through the transcriptional regulatory machinery, resulting in varied gene expression profiles [129]. The HPC comprises numerous cells and distinct cell types, each possessing its unique transcriptome, and even within cell type populations, there are variations in the transcriptome [130]. Additionally, stimuli-induced changes in gene expression tend to be subtle, demanding highly sensitive measurement methods. With over 4000 genes expressed in the hippocampal formation, each region has specific and shared genes, with notable differences between DG and CA3 and variations within CA1, particularly between its dorsal and ventral parts due to their distinct projections [129, 131].

The study performed by Ye`s group have identified Differentially Expressed Genes (DEGs) in the *Neil3−/−* hippocampal DG and CA1 region associated with G-protein signaling. These genes are associated with hippocampal functions, a finding that holds significance considering the recognized transcriptional variability across different subregions of the hippocampus [132]. Transcriptomes from carefully dissected dorsal DG and CA1 samples of *Neil3−/−* mice were analyzed at adulthood (3 months). A multifactorial analysis, considering the interaction of age and genotype, was employed to delineate variations in the patterns of gene expression in wild-type and *Neil3−/−* DG and CA1. This approach facilitated the identification of NEIL3-dependent Differentially Expressed Genes (DEGs) in the adult age group. Differentially Expressed Genes (DEGs) dependent on NEIL3, and linked to hippocampal functions, exhibited enrichment in neurobiological processes vital for neurodevelopment, synaptic function, learning, and memory. This implies a fundamental role of NEIL3 in influencing transcriptional processes in both the DG and CA1 during their structural and functional maturation.

qPCR analysis investigates and compare the differential expression of key genes in Wild types and *Neil3−/−*, focusing on the Drd2 gene, Grm subunits, and Rgs subunits—gene families pivotal for hippocampal function.

5.3.1 Dopamine receptor D2 gene

The drd2 gene encodes the dopamine D2 receptor, which is a type of G protein-coupled receptor that binds to dopamine. Dopamine is a neurotransmitter that plays a crucial role in various brain functions, including learning, memory, and mood regulation. D1R activation is suggested to occur during temporary increases in dopamine levels, while D2R is implicated in sustaining dopamine effects, serving as a gating signal for encoding and maintaining new information or updates to existing representations [133].

Moreover, a decline in D2R density across various brain regions, including the hippocampus, has been correlated with cognitive impairments in conditions such as Parkinson's disease, Alzheimer’s disease, and dementia with Lewy bodies. However, the specific role of D2R in hippocampal-dependent memory processes remains relatively unexplored [134].

A recent study explored the involvement of D2R in associative and spatial learning and memory. Genetically modified mice with D2R inactivation (Drd2−/−) and targeted silencing of the receptor in the hippocampus using Drd2-small interfering RNA (Drd2-siRNA) were utilized. Results indicate that the absence of D2R compromized the acquisition and consolidation of hippocampal-dependent processes in associative and spatial learning. Moreover, both the total loss of D2R and its specific silencing in CA1 through siRNAs significantly hinder the acquisition of trace eyeblink conditioned responses. These findings are substantiated by a noticeable decrease in synaptic strength at the CA3-CA1 synapses in the hippocampus [135].

Further study of the drd2 gene in *Neil3-/-* mice is required to addresses its role in dopamine signaling and potential effects on hippocampal function. Understanding temporal dynamics is crucial, and investigating broader consequences due to drd2's role in neurological processes is essential. Findings from 3-month-old mice are insufficient; additional investigations at various postnatal timepoints are needed to fully understand Neil3's impact on drd2 gene.

5.3.2 Grm gene family

GRM2 is expressed not only in embryonic but also in adult-born dentate granule cells (DGCs). Previous studies show that neurotransmitter release from axon terminals of adult-born DGCs can be inhibited by group II metabotropic glutamate receptor (GRM) agonists, indicating GRM2 expression in fully mature and integrated adult-born DGCs. [136]. Given the continuous addition of new neurons to the granule cell population in the dentate gyrus (DG), the presence of GRM2 in newly integrated DGCs is likely crucial for the proper functioning of hippocampal circuits [137].

Another investigation has shown that the deletion of either mGluR2 or mGluR3 genes leads to alterations in the hippocampal expression of numerous genes related to glutamatergic neurotransmission. The consistent nature of the observed changes in both sets of mice aligns with the classification of mGluR2 and mGluR3 as group II mGluRs, indicating a substantial overlap in their functional roles. Simultaneously, the unique alterations in the

profile of glutamate transporter modifications between mGluR2-deficient and mGluR3-deficient mice provide additional support for emerging evidence indicating specific differences in the expression and properties of these two receptors [138]. This study aligns with my findings, which highlight a distinct pattern of gene expression for Grm2 and Grm3. GRM8 exhibits expression in glutamatergic neurons within the enteric nervous system, contributing to enhanced intestinal motility, as indicated by Tong and Kirchgessner in 2003 [139]. This gene exhibits a distinct expression pattern compared to Grm2 and Grm3, suggesting unique properties and differences in the influence of NEIL3 on these genes.

It is crucial to comprehend temporal dynamics, and exploring the broader implications of GRM's involvement in neurological processes is essential. The results from 3-month-old mice are inadequate; further investigations at different postnatal timepoints are required for a comprehensive understanding of Neil3's influence on Grm gene family. Moreover, different cell types in the brain maintain their unique chromosomal compositions through the transcriptional regulatory machinery, resulting in varied gene expression profiles

5.3.3 Rgs gene family

The intricate regulation provided by RGS genes contributes to the finely tuned signaling processes within the hippocampus, influencing synaptic plasticity, neurotransmission, and ultimately impacting cognitive functions. Dysfunction in RGS genes has been implicated in various neurological disorders, underscoring their significance in maintaining proper hippocampal function and cognitive processes. The study unravel the intricate mechanisms through which RGS genes contribute to hippocampal physiology and their potential implications in neurological health and disease [140].

Another studies have suggested that different RGS genes plays a role in regulating central nervous system (CNS) cholinergic and dopaminergic signaling, along with its involvement in endocannabinoid-mediated long-term depression [140]. qPCR analysis of Rgs3, Rgs6, Rgs9, Rgs16, and Rgs20 genes revealed differential expression across various regions of the hippocampus, indicating distinct functions and properties in different hippocampal regions. These gene exhibits a distinct expression pattern, suggesting differences in the influence of NEIL3 on these genes. Additional investigation into the rgs gene in *Neil3-/-* mice is necessary to comprehend its role in hippocampal function. The findings from 3-month-old mice are inconclusive; hence, further exploration at various ages and timepoints is imperative.

5.4 NEIL3 impact the organization of GABAergic interneurons

The mammalian hippocampus harbours a diverse array of interneurons, comprising 21 distinct subtypes of GABAergic interneurons [141]. The 67-kDa isoform of glutamate decarboxylase (GAD67), the principal enzyme for synthesizing gamma-aminobutyric acid (GABA), is expressed in a specific subset of GABAergic neurons. This includes the subtypes such as parvalbumin (PV)-expressing cells and somatostatin (SST)-expressing cells within the cerebral cortex and hippocampus [142].

Ensuring an optimal balance between excitation and inhibition in the neural circuitry of the hippocampus is deemed essential for the proper functioning of memory and learning processes. Disruption of GABAergic interneuron activity has been linked to deficiencies in spatial learning and memory [104, 143]. Increased GABA content at inhibitory synapses and heightened synaptic inhibition in mice have been associated with learning [104]. I aimed to assess whether NEIL3 influences the organization of GABAergic interneurons in the hippocampal subregions. To explore this question, immunohistochemistry (IHC) using antibodies for GAD67, Parvalbumin (PV), and Somatostatin was conducted. The study aimed to assess the impact on cell quantity in the DG and CA1 zones of *Neil3-/-* mice. Both naive 3-month-old WT and *Neil3-/-* mice, with and without behavioural training, were included.

5.4.1 Glutamic acid decarboxylase 65-kilodalton isoform (GAD67)

GAD67 serves as a widely employed marker for GABAergic interneurons in various studies, with its selection for this project based on studying the Neil3`s influence on the organization of GABAergic inhibitory neurons. It is pertinent to note that the GAD enzyme exists in two isotypes, namely GAD67 and GAD65 [144]. Research has demonstrated that GAD65 knockout models exhibit normal GABA levels in the brain, implying that GAD67 is more prevalent and potentially adequate for GABA synthesis in neurotransmission. Despite co-localization of GAD67 and GAD65 observed in rat DG through DISH studies, [144] these investigations revealed that GAD65 exhibits higher expression in the hilus compared to other regions [144]. This finding aligns with observations made by Houser et al. [145]. Further investigation could involve employing GAD65 as a marker for GABAergic interneurons in the mouse granular zone and hilus to identify potential heightened variations in expression patterns.

The augmentation of GAD67 levels supports the replenishment of GABA released post-stimulation [146]. Analysis of GAD67 revealed a greater number of GAD67-positive cells in wild-type (WT) animals, indicating a heightened activation of inhibitory interneurons in WT animals [147]. However, the reduces interneuron activity was observed in NEIL3-depleted mice. Notably, a significant disparity between the two groups was noted before and after the behavioural training, suggesting that NEIL3 influence the organization of GABAergic inhibitory neurons. An interesting direction for further investigation involves examining the equilibrium between glutamatergic and GABAergic activities to identify potential disturbances within the hippocampus in the absence of NEIL3.

GAD67 is recognized for its trophic effects in both neuronal injury and development, as well as its ongoing role in shaping neuronal circuits during neurogenesis in the adult brain. Specifically, functional parvalbumin (PV) neurons, a subtype of GABAergic neurons, are deemed significant in certain hippocampus-dependent memory tasks in rodents [148].

5.4.2 Parvalbumin (PV)

PV-interneurons are predominantly identified as GABAergic in nature [108]. Approximately 20% of inhibitory interneurons within the hippocampal regions are identified as parvalbumin (PV)-expressing interneurons [141]. These interneurons play a crucial role in hippocampus-dependent learning tasks in rodents [148, 149]. This project aimed to explore the specific impact of NEIL3 on PV-interneurons using immunohistochemistry (IHC) with PV as a marker. No discernible difference in the number of neurons expressing PV was observed following behavioral training across different genotypes, suggesting the absence of experience-induced organization of these cells in particular. Nevertheless, a significantly lower count of PV-expressing neurons was evident in the NEIL3-depleted dentate gyrus (DG) compared to the wild-type (WT) DG, in both naive and trained animals. This finding implies that NEIL3 plays a role in regulating the activity of PV-interneurons in the DG and CA1, affecting their proper functioning.

Interestingly, recordings conducted on cells targeted against parvalbumin (PV) neurons with GAD67 deficiency have unveiled that diminished GAD67 expression in PV neurons may play a crucial role in impacting synaptic transmission. GAD67 levels have been identified as direct contributors to the strength of synaptic inhibition [101]. Consequently, the absence of GAD67 is likely to contribute to network dysfunction. This observation aligns well with the impaired performance noted in the Morris Water Maze (MWM) in NEIL3-depleted mice [33].

The outcomes of my study indicate a marked decrease in the expression of GAD67 and PV-expressing cells in the NEIL3-depleted DG and CA1. This implies that NEIL3-deficient mice may experience network dysfunction due to impaired inhibitory activity, resulting from a reduced activation of GABAergic interneurons. Moreover, Changes in the balance between excitatory and inhibitory neurotransmission can impact the survival and function of inhibitory neurons. Disruptions in this balance may lead to a reduction in interneurons.

5.4.3 Somatostatin

A potential approach involves utilizing a marker for another interneuron subtype, such as somatostatin, known for its association with cognitive functions,[110] to investigate the role of NEIL3 in the organization of these cells before and after the behavioural training.

In mice brain slices, neocortical SST neurons exhibit spontaneous activity at a frequency of 3 to 10 times per second, independent of glutamate or GABA signals. They form connections with neighboring neurons, leading to mutual strong inhibition. This continuous activity in SST neurons finely regulates overall inhibition levels in the neocortex and hippocampus. Unlike other neurons with fluctuating electric potentials, SST neurons maintain a steady activity. Recent studies suggest their role in influencing the duration of more active states in the outer brain layer, possibly through the activation of GABA receptors. [150].

These findings are consistent with my results as the number of somatostatin-positive interneurons does not show any distinction between the wild types and Neil3 knockouts in different hippocampal regions. They do not shift between more active state (upstate) and a less active state (downstate), however their number remains consistent even after the behavioural training. The stable numbers of these interneurons suggest that, unlike other

neuron types, somatostatin-positive interneurons may not undergo significant changes in activity levels in response to experimental conditions.

In the hippocampus, a critical region for learning and memory, somatostatin-expressing interneurons play a crucial role as part of the GABAergic inhibitory system. The organized placement of somatostatin-expressing interneurons in the hippocampus allows for precise regulation of neuronal activity. This strategic organization enables them to exert inhibitory influence on nearby pyramidal cells, contributing to the fine-tuning of network dynamics, especially in the context of learning, where precise neural activity regulation is essential for information encoding and retrieval. These interneurons are vital for network stability, preventing hyperexcitability, and their dysregulation [151].

Each GABAergic subtype displays a unique pattern of expression throughout the hippocampus [152]. In conclusion, these results are particularly interesting and indicate that deficiency of NEIL3 impact the organization of GABAergic interneurons in hippocampal subregions. Overall, my results highlighting a noteworthy reduction in the inhibitory network in knockout mice.

A significant finding is the reduced number of PV-positive and GAD67-positive interneurons in the DG and CA1 of NEIL3-depleted mice. Behavioral training did not influence GABAergic interneurons, indicating NEIL3's potential impact on their organization. Employing additional GABAergic interneuron subtypes as markers can enhance the assessment of interneuron organization in the hippocampus. Further exploration should include quantifying the fluorescent intensity of GAD67 in hippocampal cells from both naïve and trained animals to draw conclusions about NEIL3's potential impact on GABAergic interneuron activation.

5.5 NEIL3 have role in the postnatal maturation of hippocampal subregions.

I investigated the potential role of NEIL3 in postnatal maturation and its impact on neurogenesis in mice at postnatal days 2 (P2) and 8 (P8). The hypothesis posited that if NEIL3 plays a role in postnatal development, the results would reveal a lower count of ki67-proliferating neurons and Sox2 neural progenitor cells, reduced DCX expression, reduced neuroD1 and a higher number of mature neurons such as Neun in the hippocampus of P8 mice compared to P2 mice. Additionally, the investigation aimed to discern any distinctions in neuron count between the two genotypes within the same age group, offering valuable insights into the influence of NEIL3 on neurogenesis.

In line with existing literature, the findings revealed a reduction in average proliferating cells, neuronal progenitor cells, and immature neurons in the DG and CA1 regions. The age-related decline in neurogenesis in rodents, as observed in this study, aligns with prior observations reported by other research groups in rats [150]. CA1, a region within the hippocampus, is characterized by the presence of pyramidal cells constituting the pyramidal cell layer [151]. Donato et al. reported that CA1 reaches approximately 80% maturity at postnatal day 23 (p23) during the course of postnatal development in mice [152]. My findings align consistently with prior research.

5.5.1 Ki67-positive proliferating cells

Notably, the count of Ki67-positive cells experienced a significant decline, particularly between postnatal days 2 and 8. This observation correlates with existing literature documenting a decrease in proliferating cells after the first postnatal weeks, with subsequent proliferation primarily confined to the subgranular zone (SGZ) of the dentate gyrus [114, 153, 154]. Our observations are consistent with published results showing that the number of proliferating cells decreases with age in rodents [114].

The potential explanation for the lack of notable differences between genotypes in DG of both naive and trained animals could be the use of Ki67 as a marker for proliferating neurons, possibly concealing genotype variations. Furthermore, Ki67, a protein marker expressed throughout the cell cycle except in G0, [112] labels cells positive for the protein without distinguishing between actively proliferating and cells in cell cycle arrest, leading to potential staining of inactive cells. To address this, an alternative marker like BrdU, which incorporates into newly synthesized DNA and enables the detection of actively replicating cells, could provide more accurate insights [155]. Recent data indicate that NEIL3 deficiency is associated with increased cell proliferation. Notably, the use of BrdU labeling suggests that employing another marker such as BrdU may unveil differences not apparent with Ki67 [156].

In animals at postnatal day 8, comparatively significantly decreased Ki67-positive cells was observed, predominantly localized to the SGZ, the region associated with adult neurogenesis [119, 157]. These findings are consistent with my results that the number of proliferating cells decline significantly with age.

The current study primarily focuses on animals at postnatal day 2 and 8, potentially limiting the generalizability of findings to other developmental stages. Therefore, further experiments must be conducted that span different developmental stages to capture the dynamic changes in proliferating cells throughout development.

5.5.2 Sex determining region Y-box 2 (Sox2)

SOX2, a transcription factor essential for fostering the self-renewal and proliferation of NSCs, displayed a parallel trend in neural progenitor cells. Sox2 is initially expressed by neural progenitors and subsequently downregulated during their differentiation into neurons. The initial insights into the role of SOX2 in the hippocampal formation were gleaned from studying hypomorphic Sox2 mutant mice (hypo Sox2 KO). Mice with a compound heterozygosity, possessing a null Sox2 allele on one chromosome and a deletion of a telencephalic enhancer on the other chromosome, exhibited diminished neural stem cells (NSC) in the adult dentate gyrus. Additionally, their capacity to generate differentiated neurons was compromised [158].

My results showed that the expression level of Sox2 elevates at P2 and significantly declined in later postnatal timepoint p8 in both wildtype and *Neil3-/-* hippocampus. This sudden decrease is obvious in all the hippocampal regions which indicated that Sox2 is expressed by neural progenitors and then turned off when they differentiate into neurons. Moreover, no statistically significant differences were observed in the NEIL3-depleted mice compared to wildtype. As suggested by the acknowledged role of NEIL3 in neurogenesis [33] .However, it is important to note that the lack of a significant difference does not necessarily imply an equivalence between the wildtype and *NEIL3-/-* conditions.

The elimination of Sox2 in the mature hippocampus results in a reduction of neural stem cells (NSC) and granule neurons, underscoring the persistent requirement of SOX2 for NSC maintenance throughout an organism's lifespan [158]. Future prospects may involve leveraging novel genomic techniques, including spatial transcriptomics and single-cell RNA sequencing, to discern the specific cell types where Sox2 loss exerts profound effects and to elucidate the impact on gene expression. Moreover, it is essential to undertake further experiments spanning diverse developmental stages to intricately capture the dynamic changes in neural progenitor cells throughout the developmental process.

5.5.3 Doublecortin (DCX)

To explore the impact of NEIL3 on neuronal maturation within the dentate gyrus (DG), I utilized doublecortin (DCX) as a marker for immature neurons. Previous research has established that the DG is approximately 80% mature by postnatal day 26 (p26) [159]. Guided by this knowledge, i tracked maturation processes in the DG and CA1 throughout the first two postnatal weeks. DCX and NeuN served as neuronal markers for monitoring maturation. DCX is a protein expressed between the progenitor and calretinin-positive stages, representing the period when new neurons extend dendrites and axons, establishing functional connections [119]. As DCX expression diminishes during later developmental stages, the combined use of DCX and NeuN is suitable for assessing neuronal maturation in the hippocampus [124]. Consistent with the literature we observed a decrease in DCX fraction with increasing age [160]. The same was observed in NEIL3 depleted mice.

My results show that a lower expression level of DCX in immature neurons was observed in the hippocampus at postnatal day 8 (p8) for both WT mice and *Neil3-/-.* An alternative study employed TOAD64 as markers, employing a cell-by-cell counting method, potentially offering a more precise approach for assessing immature neurons [161]. The utilization of these markers is recommended for obtaining more accurate results. Consequently, no significant difference between the genotypes was noted at both postnatal day 2 (p2) and p8, suggesting no influence of NEIL3 on these cells.

Elevated hippocampal network activity is linked to accelerated maturation [127]. NEIL3-deficient animals display significantly higher DCX expression, possibly due to impaired network activity, correlating with observed impaired performance in NEIL3-deficient mice [33], consistent with my findings. Challenges in DCX-expression level study include strong signals in the SGZ forming clusters, making individual cell counting impractical. The DCX signal is calculated as a voxel ratio representing expression levels instead of positive cell count. DCX-expressing cells undergo morphological changes during maturation, initially forming large clusters [33]. It is worth noting that mature neurons do not express DCX [162], potentially contributing to a lower count of DCX-expressing neurons in p8 WT, while higher levels persist in p2 mice.

5.5.4 Neurogenic differentiation 1 (NeuroD1)

NeuroD1 is known to play a crucial role in regulating the differentiation of neural stem cells into neurons. The expression of NeuroD1 may be temporally regulated during specific developmental stages. NeuroD1 expression was specifically noted in the dentate gyrus (DG) but not in other hippocampal regions, closely associated with neurogenic processes. The dentate gyrus exhibits dynamic changes in neurogenesis during different phases of development, and NeuroD1 expression may be more prominent during periods of active neurogenesis.

We observed robust NeuroD1 expression in mature neurons within specific adult brain structures, particularly the hippocampus, suggesting a potential secondary role in fully differentiated hippocampal neurons. This study provides insights into the multifaceted functions of NeuroD1, emphasizing its significance in the intricate processes of neurogenesis and neuronal maturation within the hippocampus [123]. Neurons undergo maturation and differentiation over time, with the period between P2 and P8 being crucial for heightened NeuroD1 expression. This temporal expression pattern aligns with NeuroD1's known role in regulating neural stem cell differentiation into neurons. The fluctuations in neurogenesis within the dentate gyrus imply heightened NeuroD1 expression during periods of active neurogenesis, as evidenced by elevated NeuroD1 expression at postnatal day 2 (P2) and a subsequent decline with age. Another finding indicate that Neil3 have no influence on the NeuroD1 positive cells in early developmental stages. the The exclusive expression of NeuroD1 during specific time points is likely attributed to its well-established role in governing neural stem cell differentiation.

5.5.5 Neuronal nuclear protein (Neun)

NeuN is a marker mainly expressed in the nucleus with some expression in the cytoplasm. Considering that NeuN is known to bind with DNA and RNA it is thought that it has a regulatory role in neuronal differentiation [124].

Furthermore, my findings indicate an increase in the number of mature NeuN-positive neurons at p8 postnatal timepoints, aligning with established literature [124, 127]. This surge in mature neurons is associated with heightened hippocampal network activity, emphasizing the connection between maturation rates and network function [127]. The developmental progression is marked by an overall increase in mature neurons during postnatal development [163]. The concurrent decrease in immature neurons and the rise in strongly expressing NeuN-positive mature neurons during maturation may be attributed to cell migration from the hilus to the granule cell layer [163]. Notably, due to the ongoing neurogenesis in the dentate gyrus throughout adulthood, DCX expression persists into adulthood [164, 165]. The significant discovery in *Neil3-/-* mice is the observed delayed maturation in hippocampal regions, as indicated by robust NeuN expression. These results validate our hypothesis, affirming that NEIL3 indeed influences the maturation of neurons in the dentate gyrus.

Donato et al. demonstrated that CA3 reaches 80% maturation at p20, CA1 at p23, while DG attains this stage at p26 [152]. The earlier maturation of CA3, preceding CA1, may elucidate the robust NeuN expression observed throughout the entire CA3 area in animals at p2. In contrast, in CA1, strong expression was confined to the superior part of the pyramidal cell layer, adjacent to the stratum oriens. To address this inquiry with enhanced

precision, a more refined approach involving specific immature markers for CA1, CA3, and DG, along with additional time points, is recommended [159].

My findings revealed discernible differences in loss of NeuN-positive cell density in DG, CA1 and CA3 in *Neil3-/-.* This observation suggests a potential region-specific cell loss, aligning with findings by Mani et al, who reported a slightly higher cell loss in aged individuals in CA1 (19%) compared to CA3 (17%) [166]. Furthermore, our findings are preliminary and necessitate validation with a larger sample size.

6. Conclusion and future perspectives

Transcriptomic studies revealed differentially expressed genes (DEGs) associated with G-protein signaling in NEIL3-depleted hippocampal subregions. Further analysis through qPCR demonstrated distinct expression patterns of these Neil3-targeted genes compared to wild types. To deepen our understanding of the effects stemming from altered expression patterns of these identified genes, further investigation is warranted. Expanding the study to include mice of earlier age groups would provide insights into the developmental timeline of NEIL3's influence on the hippocampus. Additionally, the exploration of DEGs in the CA3 region of the hippocampus could contribute to a more comprehensive understanding of NEIL3's regulatory role.

Another fascinating finding is the reduced number of PV-positive and GAD67-positive interneurons in the DG and CA1 of NEIL3-depleted mice. Additionally, behavioural training did not influence the GABAergic interneurons, suggesting NEIL3's potential impact on GABAergic inhibitory neuronal organization. Future investigations should involve larger sample sizes to elucidate NEIL3's specific role in interneuron organization. I propose increasing the sample size and adjusting the interval between learning and terminating the animals to determine if the patterns observed in this study become more accentuated. Further studies should employ additional GABAergic interneuron subtypes as markers to further assess the interneuron organization in the hippocampal subregions. Further investigation should be done by quantifying the fluorescent intensity of GAD67 (voxel number) in hippocampal cells from both naïve and trained animals, to draw conclusions regarding the potential impact of NEIL3 on the activation of GABAergic interneurons. It's noteworthy that the present analysis exclusively focused on assessing the quantity of GAD67-positive cells, providing a specific aspect of the overall organization of interneurons.

I investigated the potential role of NEIL3 in postnatal maturation and development in mice at postnatal days 2 (P2) and 8 (P8). The results reveal a lower count of ki67-proliferating neurons and Sox2 neural progenitor cells, reduced DCX expression, reduced neuroD1 and a higher number of mature neurons such as Neun in the hippocampus of P8 mice compared to P2 mice. Additionally, the investigation revealed distinctions in neuron count between the two genotypes within the same age group, offering valuable insights into the influence of NEIL3 on postnatal development. Moreover, an intriguing strategy would involve examining the influence of NEIL3 on the maturation of adult-born neurons in the hippocampus, given that my findings suggest a delayed maturation rate in NEIL3-depleted animals.

Overall, my results indicate that the DNA repair enzyme NEIL3 plays an important role in the hippocampal development and function.

References:

1. Chatterjee, N. and G.C. Walker, *Mechanisms of DNA damage, repair, and mutagenesis.* Environ Mol Mutagen, 2017. **58**(5): p. 235-263.
2. Chen, X., C. Guo, and J. Kong, *Oxidative stress in neurodegenerative diseases.* Neural Regen Res, 2012. **7**(5): p. 376-85.
3. Wilson, D.M., 3rd and D.R. McNeill, *Base excision repair and the central nervous system.* Neuroscience, 2007. **145**(4): p. 1187-200.
4. Dizdaroglu, M. and P. Jaruga, *Mechanisms of free radical-induced damage to DNA.* Free Radic Res, 2012. **46**(4): p. 382-419.
5. Fishel, M.L., M.R. Vasko, and M.R. Kelley, *DNA repair in neurons: so if they don't divide what's to repair?* Mutat Res, 2007. **614**(1-2): p. 24-36.
6. Fan, J. and D.M. Wilson, 3rd, *Protein-protein interactions and posttranslational modifications in mammalian base excision repair.* Free Radic Biol Med, 2005. **38**(9): p. 1121-38.
7. Canugovi, C., et al., *The role of DNA repair in brain related disease pathology.* DNA Repair (Amst), 2013. **12**(8): p. 578-87.
8. Rolseth, V., et al., *Widespread distribution of DNA glycosylases removing oxidative DNA lesions in human and rodent brains.* DNA Repair (Amst), 2008. **7**(9): p. 1578-88.
9. Serrano, F. and E. Klann, *Reactive oxygen species and synaptic plasticity in the aging hippocampus.* Ageing Res Rev, 2004. **3**(4): p. 431-43.
10. Bohr, V.A., O.P. Ottersen, and T. Tønjum, *Genome instability and DNA repair in brain, ageing and neurological disease.* Neuroscience, 2007. **145**(4): p. 1183-6.
11. Dallosso, A.R., et al., *Inherited predisposition to colorectal adenomas caused by multiple rare alleles of MUTYH but not OGG1, NUDT1, NTH1 or NEIL 1, 2 or 3.* Gut, 2008. **57**(9): p. 1252-5.
12. Sheng, Z., et al., *8-Oxoguanine causes neurodegeneration during MUTYH-mediated DNA base excision repair.* J Clin Invest, 2012. **122**(12): p. 4344-61.
13. Wallace, S.S., *Base excision repair: a critical player in many games.* DNA Repair (Amst), 2014. **19**: p. 14-26.
14. Friedberg, E.C. and L.B. Meira, *Database of mouse strains carrying targeted mutations in genes affecting biological responses to DNA damage Version 7.* DNA Repair (Amst), 2006. **5**(2): p. 189-209.
15. Zhao, C., W. Deng, and F.H. Gage, *Mechanisms and functional implications of adult neurogenesis.* Cell, 2008. **132**(4): p. 645-60.
16. Fortini, P., et al., *The base excision repair: mechanisms and its relevance for cancer susceptibility.* Biochimie, 2003. **85**(11): p. 1053-71.
17. Dianov, G.L. and U. Hübscher, *Mammalian base excision repair: the forgotten archangel.* Nucleic Acids Res, 2013. **41**(6): p. 3483-90.
18. Akbari, M., et al., *The role of DNA base excision repair in brain homeostasis and disease.* DNA Repair (Amst), 2015. **32**: p. 172-179.
19. Krokan, H.E. and M. Bjørås, *Base excision repair.* Cold Spring Harb Perspect Biol, 2013. **5**(4): p. a012583.
20. *The Hippocampus Book*, ed. P. Andersen, et al. 2006: Oxford University Press.
21. Karahalil, B., et al., *Base excision repair capacity in mitochondria and nuclei: tissue-specific variations.* Faseb j, 2002. **16**(14): p. 1895-902.
22. Pan, L., J. Penney, and L.H. Tsai, *Chromatin regulation of DNA damage repair and genome integrity in the central nervous system.* J Mol Biol, 2014. **426**(20): p. 3376-88.
23. Gavin, D.P., K.A. Chase, and R.P. Sharma, *Active DNA demethylation in post-mitotic neurons: a reason for optimism.* Neuropharmacology, 2013. **75**: p. 233-45.
24. Ma, D.K., et al., *Epigenetic choreographers of neurogenesis in the adult mammalian brain.* Nat Neurosci, 2010. **13**(11): p. 1338-44.

25. Wu, S.C. and Y. Zhang, *Active DNA demethylation: many roads lead to Rome.* Nat Rev Mol Cell Biol, 2010. **11**(9): p. 607-20.
26. Liu, M., S. Doublié, and S.S. Wallace, *Neil3, the final frontier for the DNA glycosylases that recognize oxidative damage.* Mutat Res, 2013. **743-744**: p. 4-11.
27. Neurauter, C.G., L. Luna, and M. Bjørås, *Release from quiescence stimulates the expression of human NEIL3 under the control of the Ras dependent ERK-MAP kinase pathway.* DNA Repair (Amst), 2012. **11**(4): p. 401-9.
28. Zhou, J., et al., *The NEIL glycosylases remove oxidized guanine lesions from telomeric and promoter quadruplex DNA structures.* Nucleic Acids Res, 2015. **43**(14): p. 7171.
29. Krokeide, S.Z., et al., *Human NEIL3 is mainly a monofunctional DNA glycosylase removing spiroimindiohydantoin and guanidinohydantoin.* DNA Repair (Amst), 2013. **12**(12): p. 1159-64.
30. Liu, M., et al., *Structural characterization of a mouse ortholog of human NEIL3 with a marked preference for single-stranded DNA.* Structure, 2013. **21**(2): p. 247-56.
31. Ha, A., Y. Lin, and S. Yan, *A non-canonical role for the DNA glycosylase NEIL3 in suppressing APE1 endonuclease-mediated ssDNA damage.* J Biol Chem, 2020. **295**(41): p. 14222-14235.
32. Liu, M., et al., *The mouse ortholog of NEIL3 is a functional DNA glycosylase in vitro and in vivo.* Proc Natl Acad Sci U S A, 2010. **107**(11): p. 4925-30.
33. Regnell, C.E., et al., *Hippocampal adult neurogenesis is maintained by Neil3-dependent repair of oxidative DNA lesions in neural progenitor cells.* Cell Rep, 2012. **2**(3): p. 503-10.
34. Schomacher, L., et al., *Neil DNA glycosylases promote substrate turnover by Tdg during DNA demethylation.* Nat Struct Mol Biol, 2016. **23**(2): p. 116-124.
35. Kunath, N., et al., *DNA repair enzyme NEIL3 enables a stable neural representation of space by shaping transcription in hippocampal neurons.* iScience, 2021. **24**(12): p. 103470.
36. Hildrestrand, G.A., et al., *Expression patterns of Neil3 during embryonic brain development and neoplasia.* BMC Neurosci, 2009. **10**: p. 45.
37. Wu, X. and Y. Zhang, *TET-mediated active DNA demethylation: mechanism, function and beyond.* Nat Rev Genet, 2017. **18**(9): p. 517-534.
38. Müller, U., et al., *TET-mediated oxidation of methylcytosine causes TDG or NEIL glycosylase dependent gene reactivation.* Nucleic Acids Res, 2014. **42**(13): p. 8592-604.
39. Reis, A. and O. Hermanson, *The DNA glycosylases OGG1 and NEIL3 influence differentiation potential, proliferation, and senescence-associated signs in neural stem cells.* Biochem Biophys Res Commun, 2012. **423**(4): p. 621-6.
40. Zhou, J., et al., *NEIL3 Repairs Telomere Damage during S Phase to Secure Chromosome Segregation at Mitosis.* Cell Rep, 2017. **20**(9): p. 2044-2056.
41. Regnell, Christine E., et al., *Hippocampal Adult Neurogenesis Is Maintained by Neil3-Dependent Repair of Oxidative DNA Lesions in Neural Progenitor Cells.* Cell Reports, 2012. **2**(3): p. 503-510.
42. Imayoshi, I., et al., *Roles of continuous neurogenesis in the structural and functional integrity of the adult forebrain.* Nature neuroscience, 2008. **11**(10): p. 1153-1161.
43. Squire, L.R., C.E. Stark, and R.E. Clark, *The medial temporal lobe.* Annu Rev Neurosci, 2004. **27**: p. 279-306.
44. Buzsáki, G. and E.I. Moser, *Memory, navigation and theta rhythm in the hippocampal-entorhinal system.* Nat Neurosci, 2013. **16**(2): p. 130-8.
45. Broadbent, N.J., L.R. Squire, and R.E. Clark, *Spatial memory, recognition memory, and the hippocampus.* Proc Natl Acad Sci U S A, 2004. **101**(40): p. 14515-20.
46. van Strien, N.M., N.L. Cappaert, and M.P. Witter, *The anatomy of memory: an interactive overview of the parahippocampal-hippocampal network.* Nat Rev Neurosci, 2009. **10**(4): p. 272-82.
47. Andersen, P., et al., *The Hippocampus Book*. 2006: Oxford University Press.
48. Witter, M.P., *The perforant path: projections from the entorhinal cortex to the dentate gyrus.* Prog Brain Res, 2007. **163**: p. 43-61.

49. Bayer, S.A., *Development of the hippocampal region in the rat. I. Neurogenesis examined with 3H-thymidine autoradiography.* J Comp Neurol, 1980. **190**(1): p. 87-114.
50. Driscoll, I., et al., *The aging hippocampus: a multi-level analysis in the rat.* Neuroscience, 2006. **139**(4): p. 1173-85.
51. Medina, L., A. Abellán, and E. Desfilis, *Contribution of Genoarchitecture to Understanding Hippocampal Evolution and Development.* Brain Behav Evol, 2017. **90**(1): p. 25-40.
52. O'Keefe, J. and L. Nadel, *The Hippocampus as a Cognitive Map*. 1978: Oxford: Clarendon Press.
53. Amaral, D.G. and M.P. Witter, *The three-dimensional organization of the hippocampal formation: a review of anatomical data.* Neuroscience, 1989. **31**(3): p. 571-91.
54. Zemla, R. and J. Basu, *Hippocampal function in rodents.* Curr Opin Neurobiol, 2017. **43**: p. 187-197.
55. Hargreaves, E.L., et al., *Major dissociation between medial and lateral entorhinal input to dorsal hippocampus.* Science, 2005. **308**(5729): p. 1792-4.
56. Eichenbaum, H., *Remembering: functional organization of the declarative memory system.* Curr Biol, 2006. **16**(16): p. R643-5.
57. Sargolini, F., et al., *Conjunctive representation of position, direction, and velocity in entorhinal cortex.* Science, 2006. **312**(5774): p. 758-62.
58. Ahmed, O.J. and M.R. Mehta, *The hippocampal rate code: anatomy, physiology and theory.* Trends Neurosci, 2009. **32**(6): p. 329-38.
59. Li, Y., et al., *A distinct entorhinal cortex to hippocampal CA1 direct circuit for olfactory associative learning.* Nat Neurosci, 2017. **20**(4): p. 559-570.
60. Freund, T.F. and G. Buzsáki, *Interneurons of the hippocampus.* Hippocampus, 1996. **6**(4): p. 347-470.
61. Nakazawa, K., et al., *Requirement for hippocampal CA3 NMDA receptors in associative memory recall.* Science, 2002. **297**(5579): p. 211-8.
62. O'Keefe, J., *Place units in the hippocampus of the freely moving rat.* Exp Neurol, 1976. **51**(1): p. 78-109.
63. Kjelstrup, K.B., et al., *Finite scale of spatial representation in the hippocampus.* Science, 2008. **321**(5885): p. 140-3.
64. Sharp, P.E., *Subicular cells generate similar spatial firing patterns in two geometrically and visually distinctive environments: comparison with hippocampal place cells.* Behav Brain Res, 1997. **85**(1): p. 71-92.
65. Sharp, P.E., *Multiple spatial/behavioral correlates for cells in the rat postsubiculum: multiple regression analysis and comparison to other hippocampal areas.* Cereb Cortex, 1996. **6**(2): p. 238-59.
66. Taube, J.S., *Place cells recorded in the parasubiculum of freely moving rats.* Hippocampus, 1995. **5**(6): p. 569-83.
67. Maurer, A.P., et al., *Self-motion and the origin of differential spatial scaling along the septo-temporal axis of the hippocampus.* Hippocampus, 2005. **15**(7): p. 841-52.
68. Fyhn, M., et al., *Spatial representation in the entorhinal cortex.* Science, 2004. **305**(5688): p. 1258-64.
69. Burwell, R.D. and D.G. Amaral, *Cortical afferents of the perirhinal, postrhinal, and entorhinal cortices of the rat.* J Comp Neurol, 1998. **398**(2): p. 179-205.
70. Remondes, M. and E.M. Schuman, *Role for a cortical input to hippocampal area CA1 in the consolidation of a long-term memory.* Nature, 2004. **431**(7009): p. 699-703.
71. Taube, J.S., R.U. Muller, and J.B. Ranck, Jr., *Head-direction cells recorded from the postsubiculum in freely moving rats. II. Effects of environmental manipulations.* J Neurosci, 1990. **10**(2): p. 436-47.
72. Rowland, D.C., et al., *Functional properties of stellate cells in medial entorhinal cortex layer II.* Elife, 2018. **7**.
73. Watson, C., *The Mouse Nervous System*. 2011. 814.

74. Segi-Nishida, E. and K. Suzuki, *Regulation of adult-born and mature neurons in stress response and antidepressant action in the dentate gyrus of the hippocampus.* Neurosci Res, 2022.
75. van Ooyen, A., et al., *Chapter 18 - Adult Neurogenesis and Synaptic Rewiring in the Hippocampal Dentate Gyrus*, in *The Rewiring Brain*, A. van Ooyen and M. Butz-Ostendorf, Editors. 2017, Academic Press: San Diego. p. 389-408.
76. Leuner, B. and E. Gould, *Structural plasticity and hippocampal function.* Annu Rev Psychol, 2010. **61**: p. 111-40, c1-3.
77. Barnard, R.C., et al., *Chapter 6 - Clustered Arrangement of Inhibitory Neurons Can Lead to Oscillatory Dynamics in a Model of Activity-Dependent Structural Plasticity*, in *The Rewiring Brain*, A. van Ooyen and M. Butz-Ostendorf, Editors. 2017, Academic Press: San Diego. p. 123-154.
78. Hainmueller, T. and M. Bartos, *Dentate gyrus circuits for encoding, retrieval and discrimination of episodic memories.* Nat Rev Neurosci, 2020. **21**(3): p. 153-168.
79. Gonçalves, J.T., S.T. Schafer, and F.H. Gage, *Adult Neurogenesis in the Hippocampus: From Stem Cells to Behavior.* Cell, 2016. **167**(4): p. 897-914.
80. Baker, S., et al., *The Human Dentate Gyrus Plays a Necessary Role in Discriminating New Memories.* Curr Biol, 2016. **26**(19): p. 2629-2634.
81. Madroñal, N., et al., *Rapid erasure of hippocampal memory following inhibition of dentate gyrus granule cells.* Nat Commun, 2016. **7**: p. 10923.
82. Leal, S.L. and M.A. Yassa, *Neurocognitive Aging and the Hippocampus across Species.* Trends Neurosci, 2015. **38**(12): p. 800-812.
83. Rodríguez, J.J., et al., *Impaired adult neurogenesis in the dentate gyrus of a triple transgenic mouse model of Alzheimer's disease.* PLoS One, 2008. **3**(8): p. e2935.
84. Toda, T., et al., *The role of adult hippocampal neurogenesis in brain health and disease.* Mol Psychiatry, 2019. **24**(1): p. 67-87.
85. Yassa, M.A., et al., *Age-related memory deficits linked to circuit-specific disruptions in the hippocampus.* Proc Natl Acad Sci U S A, 2011. **108**(21): p. 8873-8.
86. Burke, S.N. and C.A. Barnes, *Neural plasticity in the ageing brain.* Nat Rev Neurosci, 2006. **7**(1): p. 30-40.
87. Hayashi, K., et al., *Cellular dynamics of neuronal migration in the hippocampus.* Front Neurosci, 2015. **9**: p. 135.
88. Bannister, N.J. and A.U. Larkman, *Dendritic morphology of CA1 pyramidal neurones from the rat hippocampus: II. Spine distributions.* J Comp Neurol, 1995. **360**(1): p. 161-71.
89. Pearce, R.A., *Physiological evidence for two distinct GABAA responses in rat hippocampus.* Neuron, 1993. **10**(2): p. 189-200.
90. Andersen, P., T.W. Blackstad, and T. Lömo, *Location and identification of excitatory synapses on hippocampal pyramidal cells.* Exp Brain Res, 1966. **1**(3): p. 236-48.
91. Urbán, N. and F. Guillemot, *Neurogenesis in the embryonic and adult brain: same regulators, different roles.* Front Cell Neurosci, 2014. **8**: p. 396.
92. Reznikov, K.Y., *Cell proliferation and cytogenesis in the mouse hippocampus.* Adv Anat Embryol Cell Biol, 1991. **122**: p. 1-74.
93. Caronia-Brown, G., et al., *The cortical hem regulates the size and patterning of neocortex.* Development, 2014. **141**(14): p. 2855-65.
94. Khalaf-Nazzal, R. and F. Francis, *Hippocampal development - old and new findings.* Neuroscience, 2013. **248**: p. 225-42.
95. Lagali, P.S., C.P. Corcoran, and D.J. Picketts, *Hippocampus development and function: role of epigenetic factors and implications for cognitive disease.* Clin Genet, 2010. **78**(4): p. 321-33.
96. Nakahira, E. and S. Yuasa, *Neuronal generation, migration, and differentiation in the mouse hippocampal primoridium as revealed by enhanced green fluorescent protein gene transfer by means of in utero electroporation.* J Comp Neurol, 2005. **483**(3): p. 329-40.

97. Beaulieu, J.M. and R.R. Gainetdinov, *The physiology, signaling, and pharmacology of dopamine receptors.* Pharmacol Rev, 2011. **63**(1): p. 182-217.
98. Dubovyk, V. and D. Manahan-Vaughan, *Gradient of Expression of Dopamine D2 Receptors Along the Dorso-Ventral Axis of the Hippocampus.* Front Synaptic Neurosci, 2019. **11**: p. 28.
99. Reshetnikov, V.V., et al., *The Long-Term Effects of Early Postnatal Stress on Cognitive Abilities and Expression of Genes of the Glutamatergic System in Mice.* Neurochemical Journal, 2018. **12**(2): p. 142-151.
100. Wang, X., et al., *Transcriptomic responses in mouse brain exposed to chronic excess of the neurotransmitter glutamate.* BMC Genomics, 2010. **11**: p. 360.
101. Lazarus, M.S., K. Krishnan, and Z.J. Huang, *GAD67 deficiency in parvalbumin interneurons produces deficits in inhibitory transmission and network disinhibition in mouse prefrontal cortex.* Cereb Cortex, 2015. **25**(5): p. 1290-6.
102. Nahar, L., B.M. Delacroix, and H.W. Nam, *The Role of Parvalbumin Interneurons in Neurotransmitter Balance and Neurological Disease.* Front Psychiatry, 2021. **12**: p. 679960.
103. Kelsom, C. and W. Lu, *Development and specification of GABAergic cortical interneurons.* Cell Biosci, 2013. **3**(1): p. 19.
104. Andrews-Zwilling, Y., et al., *Hilar GABAergic interneuron activity controls spatial learning and memory retrieval.* PLoS One, 2012. **7**(7): p. e40555.
105. Harada, K., et al., *GABA Signaling and Neuroactive Steroids in Adrenal Medullary Chromaffin Cells.* Front Cell Neurosci, 2016. **10**: p. 100.
106. Riedemann, T., *Diversity and Function of Somatostatin-Expressing Interneurons in the Cerebral Cortex.* Int J Mol Sci, 2019. **20**(12).
107. Gonchar, Y., Q. Wang, and A. Burkhalter, *Multiple distinct subtypes of GABAergic neurons in mouse visual cortex identified by triple immunostaining.* Front Neuroanat, 2007. **1**: p. 3.
108. Kosaka, T., et al., *GABAergic neurons containing the Ca2+-binding protein parvalbumin in the rat hippocampus and dentate gyrus.* Brain Res, 1987. **419**(1-2): p. 119-30.
109. Houser, C.R., *Interneurons of the dentate gyrus: an overview of cell types, terminal fields and neurochemical identity.* Prog Brain Res, 2007. **163**: p. 217-32.
110. Abbas, A.I., et al., *Somatostatin Interneurons Facilitate Hippocampal-Prefrontal Synchrony and Prefrontal Spatial Encoding.* Neuron, 2018. **100**(4): p. 926-939.e3.
111. Gerdes, J., et al., *Cell cycle analysis of a cell proliferation-associated human nuclear antigen defined by the monoclonal antibody Ki-67.* J Immunol, 1984. **133**(4): p. 1710-5.
112. Urruticoechea, A., I.E. Smith, and M. Dowsett, *Proliferation marker Ki-67 in early breast cancer.* J Clin Oncol, 2005. **23**(28): p. 7212-20.
113. Scholzen, T. and J. Gerdes, *The Ki-67 protein: from the known and the unknown.* J Cell Physiol, 2000. **182**(3): p. 311-22.
114. Qiu, L., et al., *Changes of cell proliferation and differentiation in the developing brain of mouse.* Neurosci Bull, 2007. **23**(1): p. 46-52.
115. Vinci, L., et al., *Immunohistochemical markers of neural progenitor cells in the early embryonic human cerebral cortex.* Eur J Histochem, 2016. **60**(1): p. 2563.
116. Pibiri, V., et al., *Stem/progenitor cells in the developing human cerebellum: an immunohistochemical study.* Eur J Histochem, 2016. **60**(3): p. 2686.
117. Kang, W. and J.M. Hébert, *A Sox2 BAC transgenic approach for targeting adult neural stem cells.* PLoS One, 2012. **7**(11): p. e49038.
118. Zhang, J. and J. Jiao, *Molecular Biomarkers for Embryonic and Adult Neural Stem Cell and Neurogenesis.* Biomed Res Int, 2015. **2015**: p. 727542.
119. von Bohlen und Halbach, O., *Immunohistological markers for proliferative events, gliogenesis, and neurogenesis within the adult hippocampus.* Cell Tissue Res, 2011. **345**(1): p. 1-19.
120. Francis, F., et al., *Doublecortin Is a Developmentally Regulated, Microtubule-Associated Protein Expressed in Migrating and Differentiating Neurons.* Neuron, 1999. **23**(2): p. 247-256.

121. Nacher, J., C. Crespo, and B. McEwen, *DCX expression in the adult rat telencephalon.* The European journal of neuroscience, 2001. **14**: p. 629-44.
122. Gao, Z., et al., *Neurod1 is essential for the survival and maturation of adult-born neurons.* Nat Neurosci, 2009. **12**(9): p. 1090-2.
123. Matsuda, T., et al., *Pioneer Factor NeuroD1 Rearranges Transcriptional and Epigenetic Profiles to Execute Microglia-Neuron Conversion.* Neuron, 2019. **101**(3): p. 472-485.e7.
124. Gusel'nikova, V.V. and D.E. Korzhevskiy, *NeuN As a Neuronal Nuclear Antigen and Neuron Differentiation Marker.* Acta Naturae, 2015. **7**(2): p. 42-7.
125. Duan, W., et al., *Novel Insights into NeuN: from Neuronal Marker to Splicing Regulator.* Mol Neurobiol, 2016. **53**(3): p. 1637-1647.
126. Mullen, R.J., C.R. Buck, and A.M. Smith, *NeuN, a neuronal specific nuclear protein in vertebrates.* Development, 1992. **116**(1): p. 201-11.
127. Piatti, V.C., et al., *The timing for neuronal maturation in the adult hippocampus is modulated by local network activity.* J Neurosci, 2011. **31**(21): p. 7715-28.
128. Sejersted, Y., et al., *Endonuclease VIII-like 3 (Neil3) DNA glycosylase promotes neurogenesis induced by hypoxia-ischemia.* Proc Natl Acad Sci U S A, 2011. **108**(46): p. 18802-7.
129. Kang, M.G., et al., *Proteogenomics of the human hippocampus: The road ahead.* Biochim Biophys Acta, 2015. **1854**(7): p. 788-97.
130. Datson, N.A., et al., *MicroSAGE: a modified procedure for serial analysis of gene expression in limited amounts of tissue.* Nucleic Acids Res, 1999. **27**(5): p. 1300-7.
131. Dong, H.W., et al., *Genomic-anatomic evidence for distinct functional domains in hippocampal field CA1.* Proc Natl Acad Sci U S A, 2009. **106**(28): p. 11794-9.
132. Thompson, C.L., et al., *Genomic anatomy of the hippocampus.* Neuron, 2008. **60**(6): p. 1010-21.
133. Wall, V.Z., et al., *A behavioral genetics approach to understanding D1 receptor involvement in phasic dopamine signaling.* Mol Cell Neurosci, 2011. **46**(1): p. 21-31.
134. Christopher, L., et al., *Combined insular and striatal dopamine dysfunction are associated with executive deficits in Parkinson's disease with mild cognitive impairment.* Brain, 2014. **137**(Pt 2): p. 565-75.
135. Espadas, I., et al., *Dopamine D2R is Required for Hippocampal-dependent Memory and Plasticity at the CA3-CA1 Synapse.* Cerebral Cortex, 2020. **31**(4): p. 2187-2204.
136. Gu, Y., et al., *Optical controlling reveals time-dependent roles for adult-born dentate granule cells.* Nat Neurosci, 2012. **15**(12): p. 1700-6.
137. Ma, J., et al., *GRM2 Regulates Functional Integration of Adult-Born DGCs by Paradoxically Modulating MEK/ERK1/2 Pathway.* J Neurosci, 2023. **43**(16): p. 2822-2836.
138. Lyon, L., et al., *Altered hippocampal expression of glutamate receptors and transporters in GRM2 and GRM3 knockout mice.* Synapse, 2008. **62**(11): p. 842-50.
139. Woo, M.S., et al., *Neuronal metabotropic glutamate receptor 8 protects against neurodegeneration in CNS inflammation.* J Exp Med, 2021. **218**(5).
140. Ahlers-Dannen, K.E., M.M. Spicer, and R.A. Fisher, *RGS Proteins as Critical Regulators of Motor Function and Their Implications in Parkinson's Disease.* Mol Pharmacol, 2020. **98**(6): p. 730-738.
141. Molgaard, S., et al., *Immunofluorescent visualization of mouse interneuron subtypes.* F1000Res, 2014. **3**: p. 242.
142. Fujihara, K., et al., *Glutamate Decarboxylase 67 Deficiency in a Subset of GABAergic Neurons Induces Schizophrenia-Related Phenotypes.* Neuropsychopharmacology, 2015. **40**(10): p. 2475-2486.
143. Bannai, H., et al., *Bidirectional Control of Synaptic GABAAR Clustering by Glutamate and Calcium.* Cell Rep, 2015. **13**(12): p. 2768-80.

144. Stone, D.J., J. Walsh, and F.M. Benes, *Localization of cells preferentially expressing GAD(67) with negligible GAD(65) transcripts in the rat hippocampus. A double in situ hybridization study.* Brain Res Mol Brain Res, 1999. **71**(2): p. 201-9.
145. Houser, C.R. and M. Esclapez, *Localization of mRNAs encoding two forms of glutamic acid decarboxylase in the rat hippocampal formation.* Hippocampus, 1994. **4**(5): p. 530-45.
146. Bowers, G., W.E. Cullinan, and J.P. Herman, *Region-specific regulation of glutamic acid decarboxylase (GAD) mRNA expression in central stress circuits.* J Neurosci, 1998. **18**(15): p. 5938-47.
147. Lau, C.G. and V.N. Murthy, *Activity-Dependent Regulation of Inhibition via GAD67.* The Journal of Neuroscience, 2012. **32**(25): p. 8521-8531.
148. Kiljan, S., et al., *Enhanced GABAergic Immunoreactivity in Hippocampal Neurons and Astroglia of Multiple Sclerosis Patients.* J Neuropathol Exp Neurol, 2019. **78**(6): p. 480-491.
149. Fuchs, E.C., et al., *Recruitment of parvalbumin-positive interneurons determines hippocampal function and associated behavior.* Neuron, 2007. **53**(4): p. 591-604.
150. Urban-Ciecko, J. and A.L. Barth, *Somatostatin-expressing neurons in cortical networks.* Nat Rev Neurosci, 2016. **17**(7): p. 401-9.
151. Yavorska, I. and M. Wehr, *Somatostatin-Expressing Inhibitory Interneurons in Cortical Circuits.* Front Neural Circuits, 2016. **10**: p. 76.
152. Kajita, Y. and H. Mushiake, *Heterogeneous GAD65 Expression in Subtypes of GABAergic Neurons Across Layers of the Cerebral Cortex and Hippocampus.* Frontiers in Behavioral Neuroscience, 2021. **15**.
153. Radic, T., et al., *Differential Postnatal Expression of Neuronal Maturation Markers in the Dentate Gyrus of Mice and Rats.* Front Neuroanat, 2017. **11**: p. 104.
154. Nicola, Z., K. Fabel, and G. Kempermann, *Development of the adult neurogenic niche in the hippocampus of mice.* Front Neuroanat, 2015. **9**: p. 53.
155. Gratzner, H.G., *Monoclonal antibody to 5-bromo- and 5-iododeoxyuridine: A new reagent for detection of DNA replication.* Science, 1982. **218**(4571): p. 474-5.
156. Egiazarian, M.A., et al., *Age- and sex-dependent effects of DNA glycosylase Neil3 on amyloid pathology, adult neurogenesis, and memory in a mouse model of Alzheimer's disease.* Free Radic Biol Med, 2022. **193**(Pt 2): p. 685-693.
157. Kee, N., et al., *The utility of Ki-67 and BrdU as proliferative markers of adult neurogenesis.* J Neurosci Methods, 2002. **115**(1): p. 97-105.
158. Mercurio, S., et al., *Deconstructing Sox2 Function in Brain Development and Disease.* Cells, 2022. **11**(10): p. 1604.
159. Donato, F., et al., *Stellate cells drive maturation of the entorhinal-hippocampal circuit.* Science, 2017. **355**(6330).
160. Gilley, J.A., C.P. Yang, and S.G. Kernie, *Developmental profiling of postnatal dentate gyrus progenitors provides evidence for dynamic cell-autonomous regulation.* Hippocampus, 2011. **21**(1): p. 33-47.
161. Gould, E., et al., *Learning enhances adult neurogenesis in the hippocampal formation.* Nat Neurosci, 1999. **2**(3): p. 260-5.
162. Brown, J.P., et al., *Transient expression of doublecortin during adult neurogenesis.* J Comp Neurol, 2003. **467**(1): p. 1-10.
163. Bliss, T., *The hippocampus book*. The hippocampus book., ed. P. Andersen, et al. 2007, New York, NY, US: Oxford University Press. xx, 832-xx, 832.
164. Eriksson, P.S., et al., *Neurogenesis in the adult human hippocampus.* Nat Med, 1998. **4**(11): p. 1313-7.
165. Rao, M.S. and A.K. Shetty, *Efficacy of doublecortin as a marker to analyse the absolute number and dendritic growth of newly generated neurons in the adult dentate gyrus.* Eur J Neurosci, 2004. **19**(2): p. 234-46.

166. Mani, R.B., J.B. Lohr, and D.V. Jeste, *Hippocampal pyramidal cells and aging in the human: a quantitative study of neuronal loss in sectors CA1 to CA4.* Exp Neurol, 1986. **94**(1): p. 29-40.

Appendix

Solutions

1. **Preparation of 1x PBS (1000 ml):**

- Dissolve 10 tablets of ready-made PBS (OXOID PBS Dulbecco A, BR0014G) in 500 ml ddH2O.
- Bring the volume up to 1000 ml with ddH2O.

2. **0.1% PBS-T (1000 ml):**

- Dissolve 1 ml of Tween20 (Sigma P1379-500ML/Lot# SLBZ5658) in 1000 ml of 1x PBS.

3. **4% Paraformaldehyde (PFA) (1000 ml):**

- Heat 500 ml of 1x PBS to around 60°C (do not boil).
- Add 40 g of PFA (Merck, 1.04005.1000) and bring the volume up to 1000 ml with 1x PBS.
- Optionally, filter the solution with a 0.2 µm filter.
- Aliquot into 50 ml tubes and store at -20°C.

4. **10% BSA/10% GS Stock Solution (500 ml):**

- Mix 50 ml of 10x PBS with 300 ml of Millipore water.
- Add 50 g of BSA and 50 ml of GS, stirring until dissolved.
- Bring the volume up to 500 ml with Millipore water.
- Aliquot and freeze at -20°C.

5. **Blocking Buffer (100 ml of 5% BSA/5% GS in 0.1% Triton/PBS):**

- Add 1 ml of PBS/Triton 10% and 50 ml of 10% BSA/10% GS.
- Bring the volume up to 100 ml with 1x PBS.

6. **Dilution Buffer (100 ml of 1% BSA/1% GS in 0.1% Triton/PBS):**

- Add 10 ml of 10% BSA/10% GS and 1 ml of PBS/Triton 10%.
- Bring the volume up to 100 ml with 1x PBS.

7. **100 mM Trisodium-Citrate Buffer Stock for Antigen Retrieval (100 ml):**

- Fill a glass bottle with 50 ml of ddH2O.
- Add 3.57 g of Trisodium-Citrate (Trisodium citrate 5.5 hydrate, Merck-Millipore 1.06431.1000) and stir.
- Adjust the pH to 6 by adding droplets of 1M HCl using a Pasteur-Pipette.
- Bring the volume up to 100 ml with ddH2O.

8. **TAE Buffer (1 L):**

- Dissolve 242 g Tris Base in about 600 ml ddH2O.
- Add 57.1 ml Glacial Acetic Acid and 100 ml 0.5 M EDTA.
- Bring the final volume up to 1 L with ddH2O.

Table 4: Comprehensive information for all tested primers, including Locus, Base pairs, Exon number, and sequences for both Forward and Reverse primers, along with their respective product sizes. The highlighted primer sequences represent the selected primers exhibiting optimal annealing temperatures.

Gene	Locus	Base pairs	Exons	Forward primer	Reverse primer	Product size
Rgs3	NM_001310706.1	2832 bp	7	GAAGCAAGAGAGCCAAGCCT	GCCTCTGTCTCAAACATCCAAG	290bp
				TCCATGTGGGAGGTGGAACC	CCTCTGTCTCAAACATCCAAGTTC	89bp
				AGGTGGAACCTGGTCATTTGG	CTGCCTCTGTCTCAAACATCCAAG	82bp
Rgs6	NM_001282061	5588 bp	16	ACCTGGGAAGCCTTATTGCC	CCTGATTGGCTGGCTTGGTA	515bp
				GCAATACACCTGGGAAGCCT	ACGGTAAAAGGTGCCATCGT	96bp
				TCCACATCCAACGACAGAGC	CAGCACCGTGGACTCTTTCT	137bp
Rgs9	NM_001165934.1	7642 bp	16	AGCGCAGACCCACATTTACA	CTCTCCTACGTGCACGACTC	341bp
				GGCGATCAGTCCAAGGTCAA	CGTAAGCCTCTCCTACGTGC	497bp
				TGCACGTAGGAGAGGCTTAC	TGGGAAGTCCCCTCTGAACT	99bp
Rgs16	NM_011267.3	2351 bp	5	GAACCCCCTCTCCTCCAGAT	ACACAGCCTTTTCTAGGCCC	280bp
				ATTCGAGTGGGCCAGTAAGC	AAAGATGTGGTGAGCCCTGG	229bp
				AGCAGGTGAGCTAAGGGAGA	CGAGACAATCGGCACAACAC	471bp
Rgs20	NM_001290372.1	1708 bp	5	CTTATCGGGCCTGGGAGCTA	TCTGCTTCCTACCCGAACCT	106bp
				GAGAGAGGGTGGGGATTGTC	TGAAGCGGGGATAGGAGTCT	729bp
				AGCGACTGAAGGTTCGGGTA	TGTGGAGTTCATGAAGCGGG	643bp
Grm2	NM_001160353.1	3338 bp	6	AGGCCATGCTTTTTGCACTG	GAAGGCCTCAATGCCTGTCT	485bp
				GCCGTACCCTTTGAACAGGA	AGCCTACCTTCTGGTAGCGA	313bp
				AATGAGCACCGTGGCATACA	TCCTGTTCAAAGGGTACGGC	965bp
Grm3	NM_181850.2	3536 bp	6	GCTCCCTCTTTTGTGTCGGA	TGAATTCCTCGCACGGTCAA	126bp
				GAAGAGGACCAACCATGAGC	TCACTGAATTCCTCGCACGG	109bp
				GCACAAGTTGGCCATTTCAG	CCGTCACTGAATTCCTCGCA	200bp
Grm8	NM_001311072.1	3570 bp	10	TGAAACCAACACTTCTTCTACCA	AGGGCTTCAATCCAGTCAGC	492bp
				ACCATGTACACCACGTGCAT	TGGTAGAAGAAGTGTTGGTTTCA	334bp
				AGTTCATCAGCCCAGCATCC	TGGTAGAAGAAGTGTTGGTTTCA	627bp
Drd2	NM_010077.3	2778 bp	8	AGTGAACAGGCGGAGAATGG	TAGACCGTGGTGGGATGGAT	154bp
				CTGGTGGCCACACTGGTTAT	GTGGGTACAGTTGCCCTTGA	495bp
				CTCAAGGGCAACTGTACCCA	GGCCAAGCCAACAATCAAGG	991bp

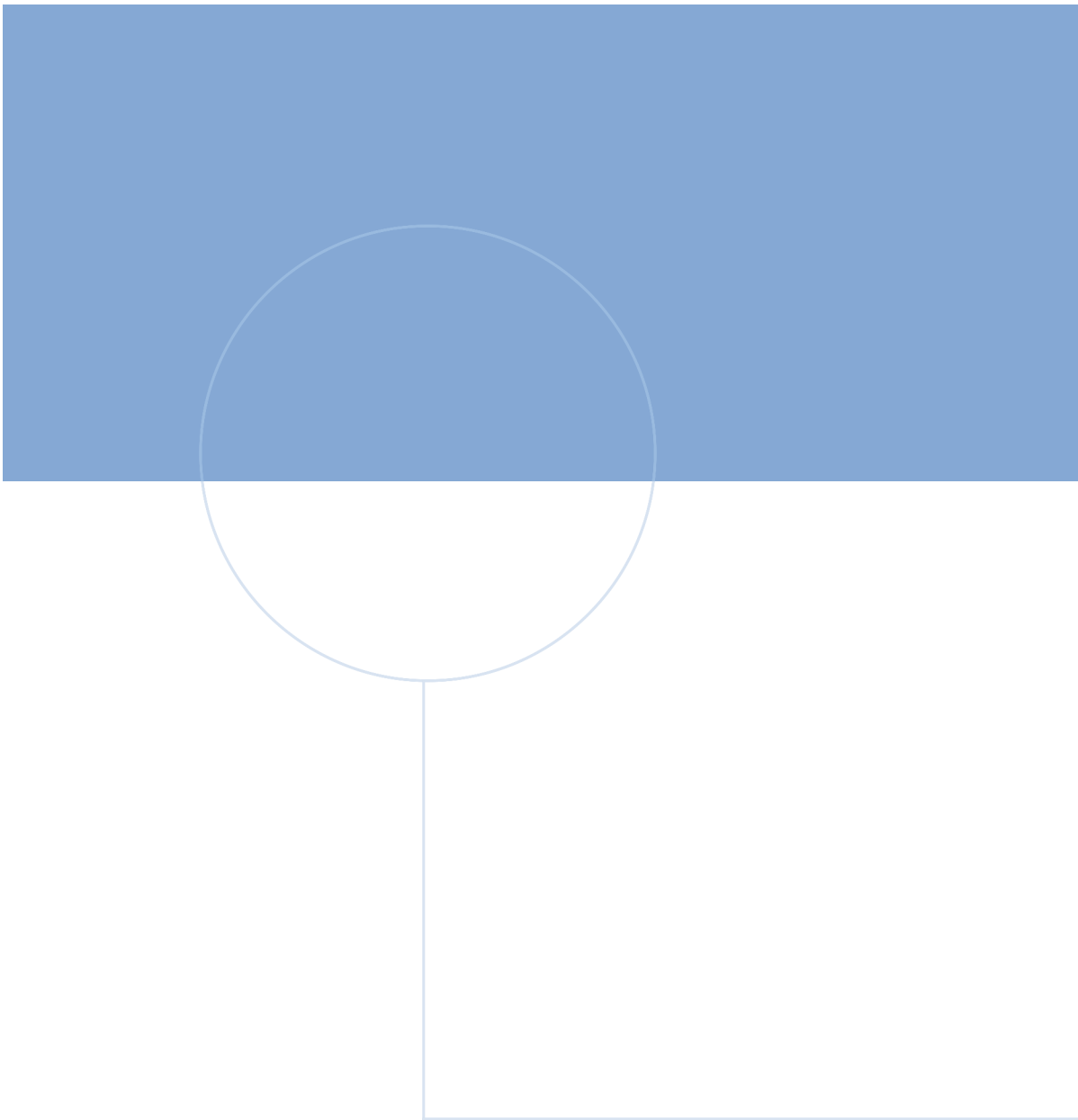

NTNU

Norwegian University of
Science and Technology